Ancient TL

www.ancienttl.org · ISSN: 2693-0935

Issue 33(1) - June 2015
https://doi.org/10.26034/la.atl.v33.i1

ISSN 0735-1348

Ancient TL

A periodical devoted to Luminescence and ESR dating

Department of Physics, East Carolina University, 1000 East 5th Street, Greenville, NC 27858, USA
http://www.ecu.edu/cs-cas/physics/ancient-timeline/

June 2015, Volume 33 No.1

Ancient TL

Started by the late David Zimmerman in 1977

Ancient TL

DosiVox: Implementing Geant 4-based software for dosimetry simulations relevant to luminescence and ESR dating techniques

Loïc Martin,[1*] Sébastien Incerti,[2,3] Norbert Mercier[1]

[1]Institut de Recherche sur les Archéomatériaux, UMR 5060 CNRS Université Bordeaux Montaigne, Centre de Recherche en Physique Appliquée à l'Archéologie (CRP2A), Maison de l'archéologie, 33607 Pessac Cedex, France
[2]CNRS, IN2P3, CENBG, UMR 5797, 33170 Gradignan, France
[3]Université de Bordeaux, CENBG, UMR 5797, 33170 Gradignan, France

[*]Corresponding Author: loic.martin@u-bordeaux-montaigne.fr

Received: June 25, 2014; in final form: December 12, 2014

Abstract

A C++ code, named *DosiVox* and based on the *Geant4* Monte Carlo simulation toolkit, was developed in order to provide a reliable and flexible tool for modeling a large variety of situations of interest in paleodosimetric dating techniques, and for simulating interactions of usual particles (α, β and γ) through complex geometries. *DosiVox* allows the user to define a three dimensional grid, in the simulation space whose voxel dimensions, materials and radioactive contents (U, Th, K) are set by a user-friendly graphical interface. No skills in C++ programming are required. Some of the possibilities offered by *DosiVox* are presented here through a series of examples.

Keywords: Dosimetry, Dating, Luminescence, ESR, Simulation, Sediment

1. Introduction

Almost thirty years ago, Aitken (1985) summarised the basis of the thermoluminescence dating technique, outlining important information relevant to the dosimetry of the samples to be dated, and also the basis for delivering known doses to samples using artificial radioactive sources, and for determining the natural dose rates to which this sample has been exposed. In particular, he collected a series of dosimetric calculations (performed by several authors) which are still of primary importance today in any dating application as, for instance, those related to β- and γ-dose gradients (Aitken et al., 1985) or to attenuation factors of the dose rates (Zimmerman, 1971; Mejdahl, 1979; Bell, 1980).

This author also exposed a technique from Fleming (1970) – the inclusion technique used for pottery dating – which, from a dosimetric point of view, can be seen as an ideal case: the grains which are the sources of the luminescence signal, are considered as embedded in a homogeneous matrix containing a uniform distribution of radioelements. In that case, the density of grains in the material (i.e. the number of grains per unit of volume) is supposed to be low enough to ensure that the presence of these grains does not alter the homogeneity of the matrix and the distribution of the radioelements, and has no influence on the particles fluxes induced by the decay of these radioelements (Guérin et al., 2012). Although defined for pottery dating, this technique is nowadays largely applied to sediment dating and it is questionable whether this model is sufficient to deal with dose rate calculations for the more complex situations which may arise.

Beyond sediment dating, the luminescence or ESR techniques are also used for dating a large diversity of samples (burnt stones, teeth, ...), each one being characterized by its elemental chemical composition, its geometry and its radioactive elements distribution. Moreover, in most cases, the distributions of the radioactive isotopes in the sample itself and its environment - from distances ranging from a few microns up to tenths of centimeters are heterogeneous, making precise dosimetric descriptions difficult, and often leading to adoption of simplifying hypotheses in order to manage the system.

Clearly dosimetry remains at the heart of the dating process, being critical to calibration of artificial sources used for irradiation in the laboratory, and for calculation of any

dose rate. In order to assess the various dosimetric hypotheses usually needed to calculate ages, we have developed a flexible dosimetric tool named *DosiVox*, which is based on the general purpose *Geant4* Monte Carlo toolkit developed at CERN for simulating particle-matter interactions (Agostinelli et al., 2003; Allison et al., 2006). Our objective was to prepare a tool which can be used to model both simple and complex cases (as those described above) and to perform dose-rate calculations. Technically, this software allows the user to create a model of the sample and its environment using a graphical interface which generates a pilot text file. No skills in programming or in the usage of the *Geant4* libraries are then required. In this paper, we outline the program operation and illustrate some of its possibilities for dose rate evaluation in simple and more complex cases.

2. Program description

The *Geant4* toolkit is a set of C++ public libraries which can be compiled with C++ codes to simulate particle-matter interactions by Monte Carlo methods. *Geant4* incorporates a wide range of physics models applied to diverse situations, ranging from high energy physics to medical and space applications (`http://www.Geant4.org`) and can be used to simulate interactions in complex detectors. In dosimetric applications relevant to dating techniques, *Geant4* has already been used for dose calculations (Guérin et al., 2012), but up to now, its potential had been under-exploited. The *DosiVox* program aims to provide a reliable and flexible tool for modeling a large variety of situations of interest in paleodosimetric dating techniques, and simulating interactions of ionizing radiation (α, β and γ) in complex geometries. The code developed has been compiled with *Geant* version 4.10p01, and uses the electromagnetic physics list provided by the G4PenelopePhysicsphysics constructor (Ivanchenko et al., 2011), which is based on the 2008 version of the PENELOPE Monte Carlo code (Baró et al., 1995) and adapted to the transport of low energy particles (Sempau et al., 2003). The secondary particle production cut can be set by the user, in order to match the desired simulations conditions. No step limit was imposed.

DosiVox allows the user to define a "World" volume for simulation in a three dimensional grid (e.g., Fig 1), whose voxel dimensions, material and radioactive contents (U, Th, K) are set through a graphical user interface. This geometrical grid is implemented by successively dividing the volume along the three axes and implementing a nested parametrization of the resulting voxels. This method considerably reduces the time and memory required for geometry optimization and navigation during simulations (Aso et al., 2007; Incerti et al., 2009). Grids with 1 to 300 million voxels, can be loaded in *DosiVox* as 3D images, which decreases the memory requirements for geometry optimization by a factor of about 20 compared to standard parametrization methods.

Different detectors, which are defined in 'parallel worlds', can be superimposed on this grid: a vertical cylindrical probe segmented in different parts, a random packing of spheres (modeling the grains) in a rectangular prism, or a sub-voxelised voxel.

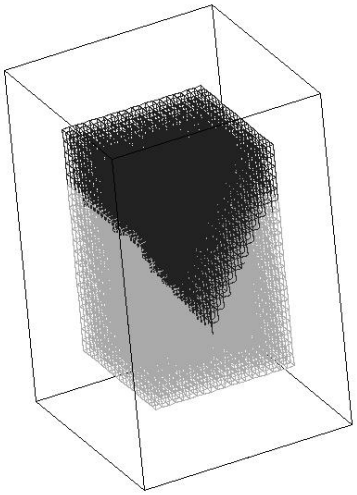

Figure 1. Main voxels grid image. The different tints indicate the different materials in the voxels.

The first of these detectors, the cylindrical probe, is always present in all the simulations but does not interact with the particles or the materials. It only records both the energies of the primary emitted particles and the energy deposited in each of its segments during the whole simulation, and accumulates them. The absorbed dose, as being defined as the deposited energy divided by the density of the material present in the center of this volume, multiplied by the volume of the probe segment itself (defined by the user), is also calculated. Calculation of the absorbed dose relatively to the infinite matrix dose is then performed using these data. The other detector types are sensitive to all particles and record the energy and hence, the dose deposited. At maximum, only one type of these detectors can be defined during a simulation.

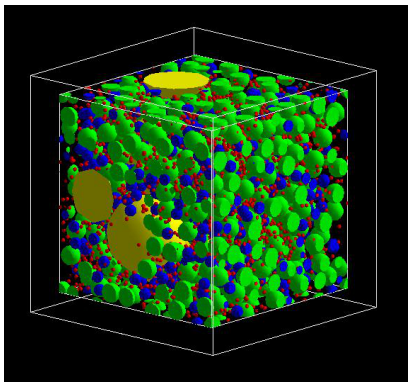

Figure 2. Random packing of grains in a defined box. The edge effects are corrected by a boundary recurrence.

The random packing of spheres was created in order to represent grains in a sedimentary medium; it is defined inside a box whose maximum dimensions are equal to those of one

voxel, and takes into account the material of the grains, their granulometry and their state of compaction (Fig. 2). This detector can also be replicated along the vertical axis of the simulation space - filling up the full height of the geometry with successive boxes containing grains packed to correspond to the material of each intercepted voxel. Moreover, the user can choose to emit particles from the spheres (i.e. the grains) or from the surrounding matrix filling these boxes. The dose deposited in each individual grain is then recorded during the simulation and is available in the results files.

The last detector is a sub-voxelised voxel allowing to define objects with a potentially higher resolution than the main grid, and to register the dose emitted and deposited in all parts of this virtual detector. The voxel chosen by the user is divided into a 3D voxel grid, and as with the main grid, the user can assign the material of choice and its radioactivity content to each of these sub-voxels. The interface allows a $20 \times 20 \times 20$ voxel grid to be defined with its material properties and radioactive contents. Voxelised 3D grey-scale images can also be used to define the detector as well as the use of files resulting from imaging methods (image processing may be necessary to transform images in vertex to image in voxel, which is required for *DosiVox*): in both cases, high resolutions can then be obtained. In the software, the dose deposited in each voxel of this detector, and the dose emitted from it, are recorded. The results are given in two ways: a summary of the dose for each material constituting the detector, and a succession of 3D map slices in ASCII matrix format allowing representation of the deposited dose in 3D, either for all the sub-voxels of the detector, or only for the sub-voxels filled with a particular material. The values in the ASCII files represent 16 bit resolution grey scale levels, and are proportional to the dose deposited.

In many cases of simulation, it is convenient to normalize the dose absorbed in the detectors by the total energy emitted by unit of mass (corresponding to the infinite matrix dose in the case of an infinite medium). The dose rates in the detectors can be then obtained by multiplying this ratio by the infinite matrix dose rate tabulated for the radioelement contents in the corresponding material. As a consequence, the simulation results normalized in this way are equivalent to dose rates.

3. Examples of simulations using *DosiVox*

The following section gives examples illustrating some of the possibilities of the *DosiVox* software. Simulations of γ-, β- and α-particles have been carried out for spectra of the U- and Th-series, ^{40}K and ^{137}Cs. The radioactive decay chains, if applicable, were treated as being in secular equilibrium. However, it is worth noting that, since the emission spectra are accessible to the user (and are defined as text files), modifications of this assumption could easily be implemented.

For visualisation of 2D and 3D images, an open sources image analysis and processing software was used: *ImageJ* (Abràmoff et al., 2004; Rasband, 1997–2012; Schneider et al., 2012), available at the website `http://imagej.nih.gov/ij/index.html`. *ImageJ* was also used to create parts of models presented in this paper, as mentioned in the corresponding paragraphs.

3.1. γ-dose attenuation by a limestone wall

The first example considered here is a sediment deposit placed alongside a limestone block. This is similar to that discussed by Aitken in Appendix H of his 1985 book. Limestones are usually considered less radioactive than clay-rich sediments, and an attenuation of the γ-dose rate (compared to the infinite matrix dose in the sediment) is then expected in the first tens of centimeters from the limestone surface.

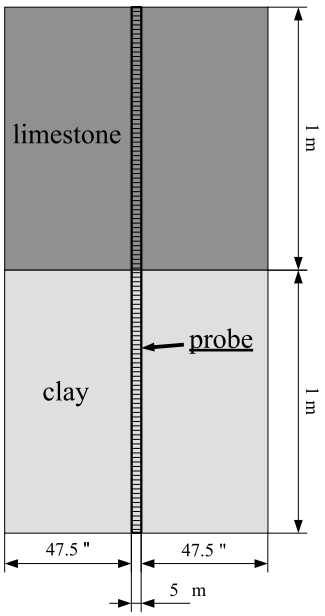

Figure 3. Plan of the geometry of the limestone wall model

To model this configuration, a limestone block has been designed in the graphical interface, by simply filling the first ten levels of voxels in the Z axis with a limestone material (chemical composition: 70 % (in mass) $CaCO_3$, 30 % $MgCO_3$, density 2.7 g/cm^3, water content: 10 % by weight) using an automated function available in the interface. The last ten levels were filled with a clay material representing the sediment (chemical composition: 55 % SiO_2, 35 % Al_2O_3, 10 % Fe_2O_3, density 2.0 g/cm^3, water content: 15 % by weight). The probe detector was positioned vertically in the middle of the simulation space, perpendicular to the boundary between the limestone and the clay (see Fig. 3) γ-photons from ^{40}K were generated, assuming a concentration in limestone ten times lower than in clay. The dose distribution absorbed by the local material in the probe shown in Fig. 4 is normalised by the infinite matrix dose delivered in the clay sediment, which is simply obtained from the sum of the energies of the primary particles emitted in the clay per unit of mass. In this simulation, the average of the energy per mass emitted from the probe segment containing the clay material has been used to calculate the infinite matrix dose.

As expected the decrease of dose at the boundary between

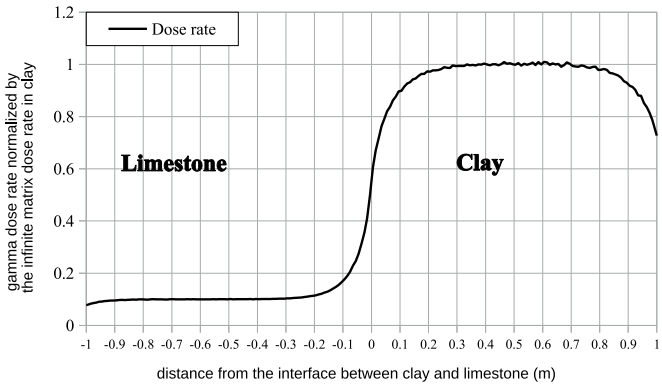

Figure 4. γ-dose rate profile of the simulation of a limestone wall adjoining a clay sediment

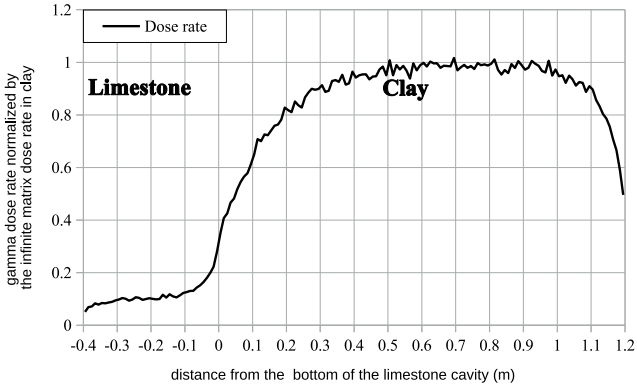

Figure 6. γ-dose rate profile of the simulation of a limestone cavity filled by a clay sediment

the limestone and the clay can be clearly observed. Dose attenuation can also be seen at the extremities of the graphic as a result of edge effects in the simulation, corresponding to the limits on the Z axis of the model grid. The continuity of the model is broken at these points, because of the non-radioactive void surrounding the voxelised grid.

A more complex configuration has been considered in the next example in which the sediment fills a limestone cavity. The cavity geometry, also created with the graphical interface, is represented in Fig. 5, and the probe remaining in the middle of the model as indicated in the figure. The same radioactive contents have been defined for the materials as for the precedent simulation, and the γ-dose profile calculated and normalized to the infinite matrix dose in the clay is shown in Fig. 6. As expected, the dose rate variations clearly differ from that of the previous configuration. As in the preceding model, edge effects can be observed at the graphic edges. The present example can easily be modified to reproduce complex boundaries between two or more media with different properties and radioactive contents.

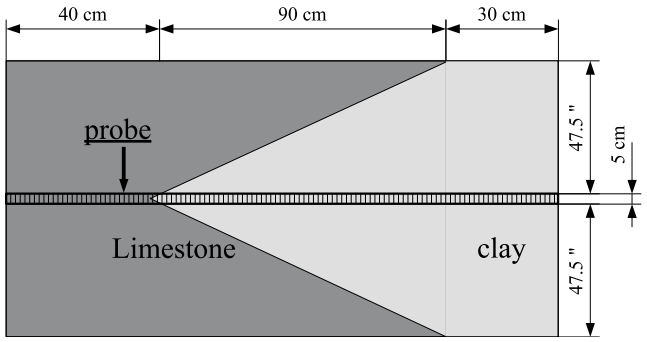

Figure 5. Plan of the geometry of the limestone cavity model

3.2. γ-irradiation of a dosimeter for source calibration

In most dating applications, the dose accumulated by a sample is determined by comparing the natural signal with the one induced by an artificial β-source, hence the importance to get an accurate calibration of this source. One way to calibrate it is to irradiate a phosphor contained in a tube (hereafter called a dosimeter) with a calibrated γ-ray beam, and to compare the induced signals with those generated by the β-source. Here, we consider a dosimeter composed of a duralumin tube filled with a powder of quartz grains, and closed with a nylon screw (Fig. 7).

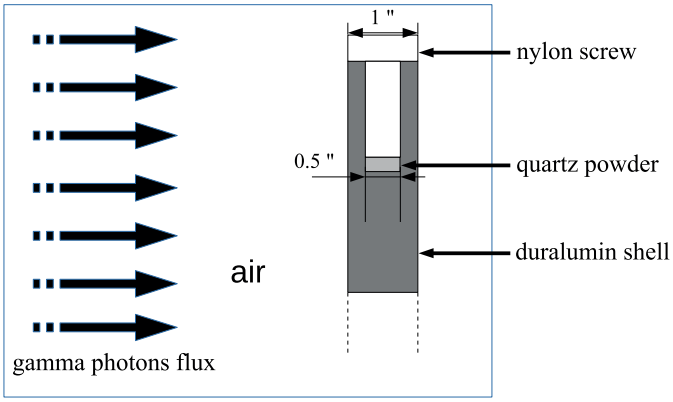

Figure 7. Plan of the geometry of the dosimeter irradiation model

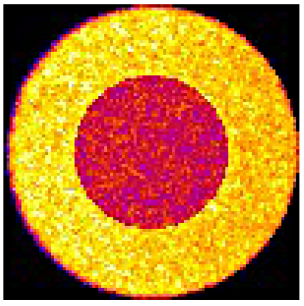

Figure 8. Map of the dose distribution in the quartz powder and its duralumin shell from an artificial irradiation (arbitrary scale)

This configuration was modeled using a 3D image of the dosimeter as input for the voxelised detector. This image has been created with *ImageJ*, and saved as an 8 bits text im-

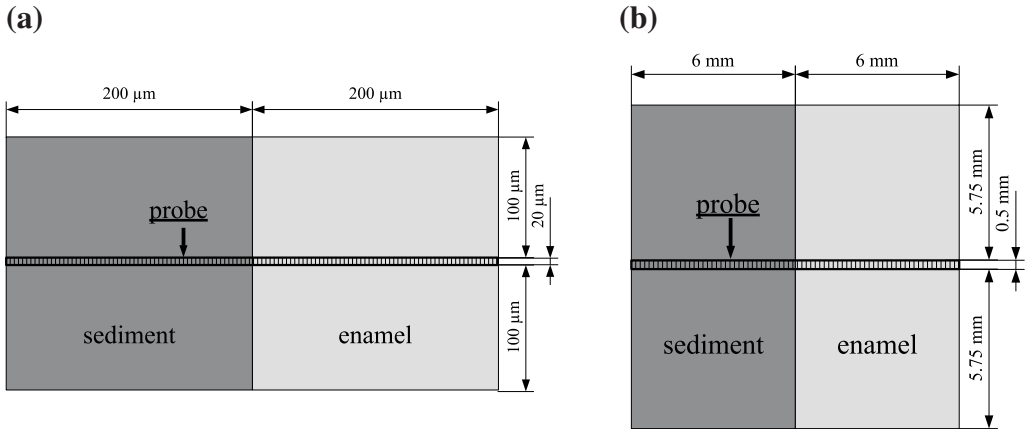

Figure 9. Plan of the geometry of enamel adjoining a sediment: (a) plan for the α-particles simulation, (b) plan for the β-particles simulation

age sequence (in ASCII format), where each grey level represents a material constituting the dosimeter. A radioactive zone has been defined in the main voxel grid with the interface, and an unidirectional emission of γ-particles with energy of 661.7 keV (corresponding to the γ-emission of ^{137}Cs) has been chosen. For this purpose, the text file defining the emission spectrum has been modified. The voxelised detector, carrying the dosimeter geometry and the materials, has been positioned in the γ-flux (Fig. 7). The map of the absorbed dose in a slice of the dosimeter at the level of the phosphor is shown in Fig. 8. This image corresponds to the ASCII result file obtained for this level of the detector, and read by *ImageJ* as an image.

In this figure one can notice a nearly homogeneous dose distribution inside the quartz grains, even though a crescent form area of low dose in the left part of the duralumin tube is observable. At last, this kind of simulations allows calculating the fraction of energy absorbed in the tube and consequently, improves the determination of the dose absorbed by the phosphor used for the β-source calibration.

3.3. β- and α-dose attenuation factors in enamel

ESR dating of teeth requires the determination of the dose rates received by the enamel, which is the dated material. Enamel is generally considered to be a low-radioactive material, and it receives its dose mainly from the internal parts of the tooth and from the burial sediment. The attenuation of both α-and β-particles, whose ranges are much lower than, or respectively, about the same size as the enamel thickness, have to be calculated for determining the correct dose rates. Simulations can provide these factors by modeling the enamel and the adjacent internal parts of the tooth and the sediment. This modeling was done directly with the pilot text file, creating two adjacent voxels instead of using the larger main grid. The first voxel was defined as a clay type sediment (chemical composition in mass: SiO_2 55 %,

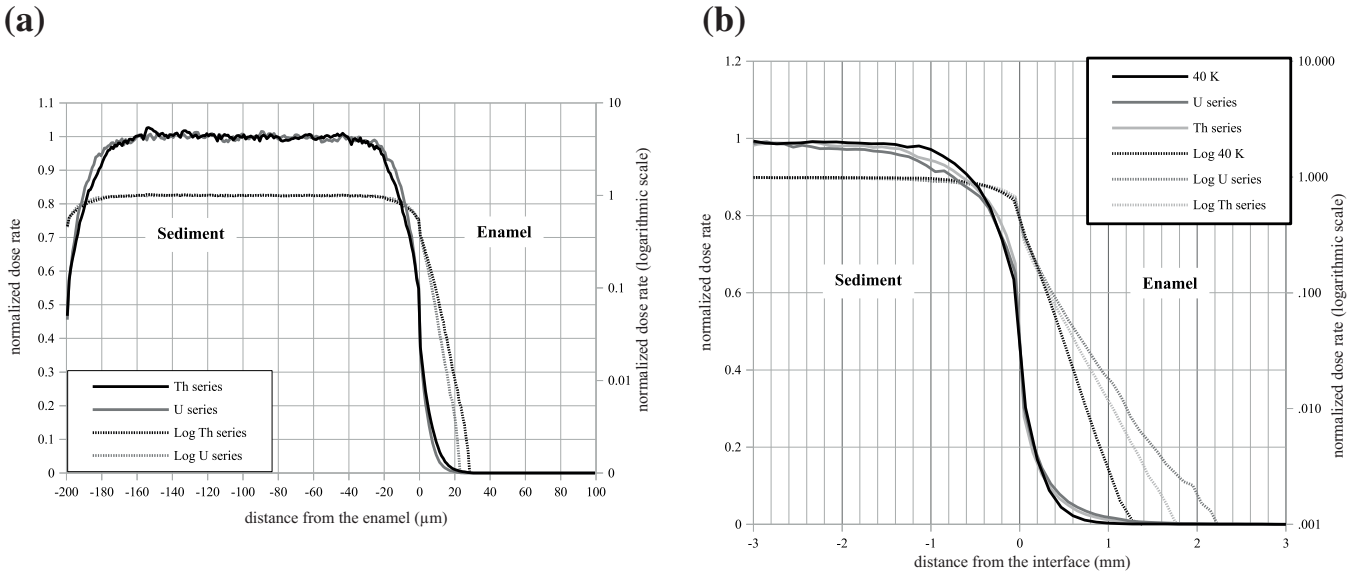

Figure 10. Dose rate attenuation in enamel from a clay sediment: (a) α-dose attenuation, (b) β-dose attenuation

Al_2O_3 35 %, Fe_2O_3 10 %; density: 2 g/cm^3, water content: 13 %), and the second is filled with hydroxyapatite (chemical raw formula: $Ca_5P_3O_{13}H$; density: 3.8 g/cm^3), which is the main component of enamel. The vertical probe was positioned in the center of the simulation space, perpendicular to the boundary between the two voxels. α- or β-particles were emitted from the sediment. In each situation, the voxel size was chosen to contain the entire radioactive environment that can be seen by the probe parts, superimposed on the enamel (Fig. 9). The absorbed α- and β-dose profiles for the uranium and thorium series spectra (and β only for ^{40}K) are given in Fig. 10. For a better legibility, the β-dose profile has been restricted to the 6 central millimeters around the interface between sediment and enamel, and the 100 last micrometers of the α-dose profile, where no dose deposition was recorded, are not shown.

The α-dose attenuation profiles indicate that the range of these particles in the enamel is lower than 30 μm. The β-particles range in enamel is close to 2 mm, and the β-dose profiles allow calculating the attenuation of the sediment dose rate.

3.4. β-dosimetry in a Neanderthal tooth enamel

This example illustrates the possibility offered by the *DosiVox* software to use 3D images for building the geometry. Indeed, dose attenuation is not the only factor necessary for calculating the dose rate to which the enamel is exposed: the tooth shape and the distribution of the radioelements in the dentin and ivory are often complex and affect the β-dose rate determination; they undoubtedly must be taken into account. A tooth model was built using a 3D image obtained from a micro-scanner tomography of a left maxillary deciduous molar associated to the Roc de Marsal Neanderthal child skull (Bayle et al., 2009). A 3D visualization of the model with the 3D viewer *ImageJ* plugin (available at the *ImageJ* website) is presented in Fig. 11; this 3D image is available in the NESPOS data base (https://www.nespos.org/display/openspace/Home). A uranium distribution model has been created considering a fast uranium uptake in the most organic parts of the tooth from the burial sediment, followed by a progressive diffusion of this radioelement in the dentin (Fig. 12). Because of the disequilibrium in the U series, each value of the uranium content has to represent the content averaged over the burial time. This model of uranium uptake does not match any real data from the tooth nor any real model of radio-elements uptake: it was simply constructed by successive dilatations in the three dimensions of the 3D image of the dental pulp zone, restricted at each step by the ivory zone. These operations were made with the 3D *ImageJ* suite plugin (Ollion et al., 2013).

Both the models concerning the structure and the radioactive distribution have been used as input data for the voxelised detector, and the simulation parameters have been set to create a dose distribution mapping in the enamel. Simulations of both the clay burial sediment dose and the internal dose have been performed. The resulting dose mapping can

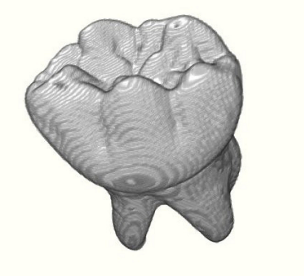

Figure 11. 3D view of the Neanderthal tooth model (*ImageJ*, 3D viewer plugin)

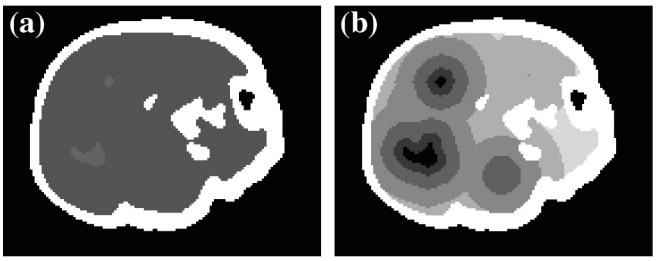

Figure 12. Slices of the tooth material 3D map and its radioactive content map: (a) material map, (b) radioactive content map (arbitrary scale, the darkest shades indicate the highest contents)

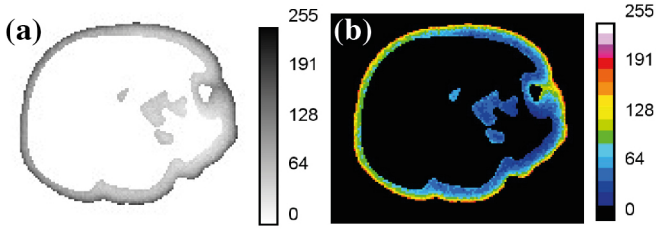

Figure 13. β-dose rate map in the tooth enamel (arbitrary scale): (a) dose distribution as a grey shades image, (b) dose distribution as a colour image

be read with the *ImageJ* software to reconstruct a 3D image of the dose distribution in the enamel. Figure 13 shows a slice of this image, corresponding to the Fig. 12 level. A heterogeneous dose distribution is observed in the enamel, as expected.

The results presented here are only intended to illustrate the possibility of calculating spatially resolved dose rates in a complex sample. In fact, there is no data for this precise sample about radioelements distribution, and no dating problematic about it either. In addition, the spectrum used for β-emission corresponds to the uranium series at equilibrium, which is obviously not common in a tooth because of the disequilibrium induced by the uptake of soluble elements of the series. But once again, the aim of this construction is not to discuss complex effects relating to uranium uptake but simply to illustrate the possibilities offered by *DosiVox*.

In the future, accurate data for both the tooth structure and

its radioactive contents, associated with a model of radioelement uptake during burial, should allow constructing reliable models in the same way as what was done in this example. Such a model would allow calculating the dose rates in every part of the tooth, for example, taking into account the disequilibrium in the U series.

3.5. β-micro-dosimetry in a stratified sediment

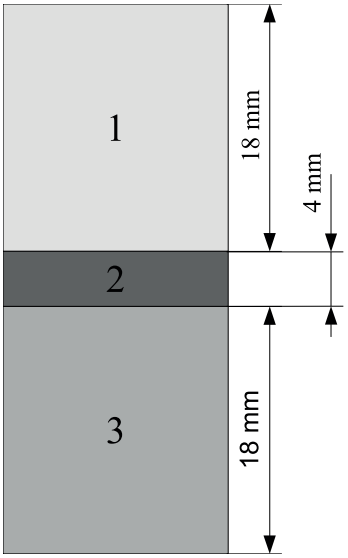

Figure 14. Plan of the geometry of the stratified sediment model: (1) clay, density = 2 g/cm^3, WF = 10 %, 100 μm grains with a compacity of 5 %, Th content: 2 ppm, (2) sand, density = 1.9 g/cm^3, WF = 18 % 40 % volumic of 200 μm grains, 45 % volumic of 100 μm grains, 15 % volumic of 50 μm grains with a total compacity of 60 %, Th content: 1 ppm, (3) clay with organic matter, density = 1.8 g/cm^3, WF = 15 %, 100 μm grains with a compacity of 5 %, Th content: 3 ppm

This example deals with the dose rates to which individual quartz grains distributed in a sediment are exposed. In the case of heterogeneous or micro-stratified sediments, micro-dosimetric phenomena can occur. In order to assess the influence of these effects on the dose received by the grains, we used the graphical interface for constructing a sedimentary environment. The simple model considered here is composed of a thin level of sand surrounded by two clay deposits, one of them being rich in organic matter (Fig. 14). The clay contained quartz grains of 100 μm in diameter, representing 5 % of the volume. The sand stratum is composed of 200 μm, 100 μm and 50 μm quartz grains, representing respectively 40 %, 45 % and 15 % of the volume of the grains. This volume accounts for 60 % of the sand level volume, and the remaining 40 % is filled with water (representing an average water content of about 18 % (in mass) for this stratum). In spite of the small thickness of this level compared to the clay levels (4 mm compared to 18 mm for the clay levels), about half of the 100 μm grains defined in this model are included in the sand stratum. Each stratum contains a different content of thorium, which are 2 ppm, 1 ppm and 3 ppm, respectively, for the clay stratum, the sand stratum and the stratum made of organic matter rich clay. *DosiVox* was used to calculate the β-dose distribution from the thorium series (at secular equilibrium) to the 100 μm grains, regardless of their location in the three defined levels. These doses were normalized with the medium dose received by the 100 μm grains localized in the part of the model non-affected by edge effects (i.e. for z values ranging from 5 mm to 35 mm). The micro-dosimetric impact of this configuration can be observed in Fig. 15, confirming that such scenarios can generate significant scatter in β-dose and dose distributions. The dose is distributed between three peaks corresponding to each level of the sediment and partially recovering themselves. The lower doses (centered around 0.6 of the average dose value), corresponding to grains localized in the sandy level, shows a Gaussian profile stretched in the direction of the higher doses. This shape results from grains located near the boundaries between the sand stratum and the more radioactive levels of clay.

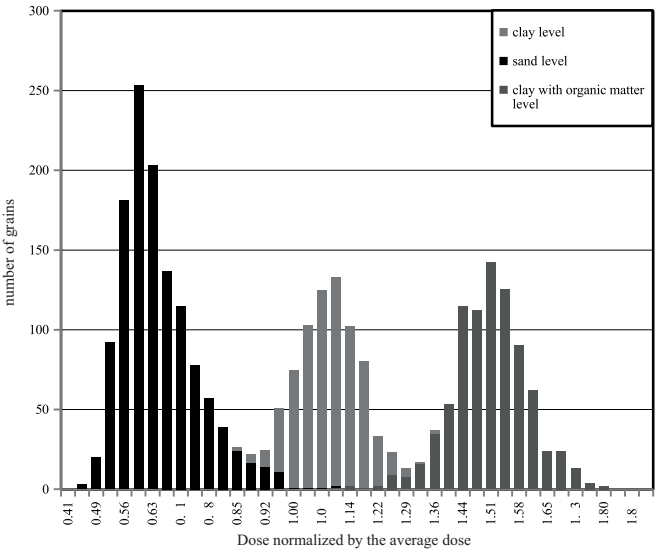

Figure 15. Dose distribution in the 100 μm grains. The tints indicate the stratum of origin of the grains

It is also interesting to notice that, in considering the average β-dose and the water content of the present model, it is possible to calculate the dose one could determine in performing, for instance, γ-ray spectrometry measurements on a bulk sediment (resulting from the mixing of the three levels). The calculation shows that this dose would correspond to a value of 1.3 of the average simulated dose received by all the 100 μm quartz grains.

3.6. Bursts of β- and α-particles

The interactions of ionizing particles in matter depend largely on the particles nature, their energy and the matter properties in which they pass through. Studying these interactions can be useful for understanding many dosimetric effects. With *DosiVox*, it is easy to model a burst of particles and to record the dose deposited in a particular material. This

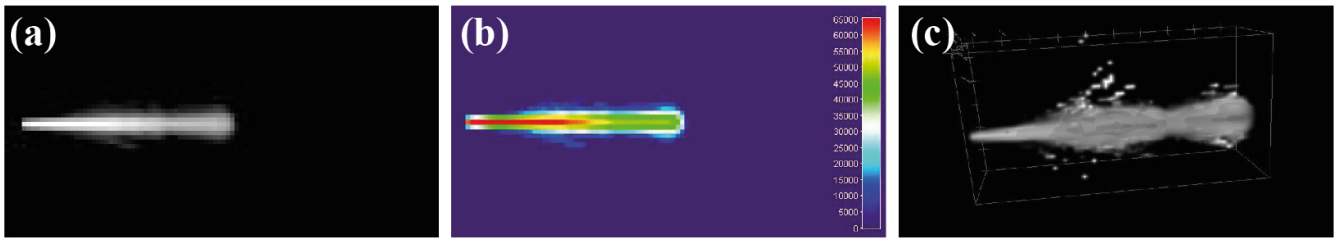

Figure 16. Dose deposition map for an α-particles spray with the energetic spectrum of the thorium series

model has been constructed with the *ImageJ* software and is based on a cubical 3D image made of $100 \times 100 \times 100$ voxels, containing a single grey tinted voxel defining the emission point. This image, saved as an ASCII text image sequence, has been first loaded in *DosiVox* to define the voxelised detector and secondly, filled with a clay type material (chemical composition in mass: SiO_2 55 %, Al_2O_3 35 %, Fe_2O_3 10 %; density: 2 g/cm^3, water content: 13 %). A unidirectional emission was chosen, and the dose deposited in the detector recorded as a 16 bits 3D image.

The central slices of the images obtained for the β- and α-particles emitted by the thorium series are presented in Fig. 16 and Fig. 17, respectively. The visualization was made by importing the images in *ImageJ* as text images. In both of them, the grey values represent the dose deposited (using a logarithmic scale).

The dose distribution from α-particles seems localized in two volumes: a first burst corresponds to α-particles with energies between 3.8 MeV and 6.8 MeV, and a more distant zone results from the 8.8 MeV α-emission of the thorium series.

Conversely, the β-dose distribution in the detector indicates very diffusive trajectories for the particles, as expected.

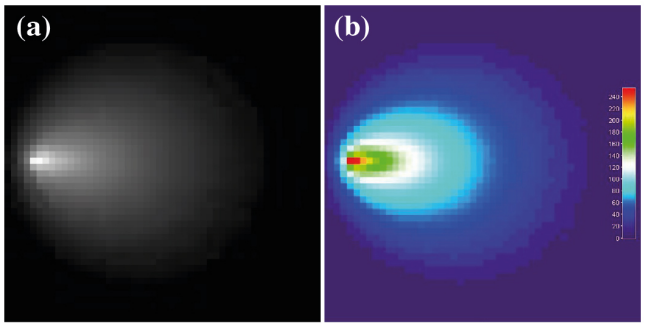

Figure 17. Dose deposition map for a β-particles spray with the energetic spectrum of the thorium series: (a) 8-bit slice of the dose deposition 3D map, (b) colored slice of the dose deposition 3D map (arbitrary logarithmic scale)

4. Discussions

The examples presented above were not intended specifically to deliver definitive data, rather to illustrate some of the numerous possibilities of the *DosiVox* software for modeling complex dosimetric systems, and providing a tool for dose rate calculations. The statistical precision of the results presented depends on simulation times, but users should also be conscious of other factors which influence the accuracy of such models.

The first category concerns the input data: to create a precise model of a sample, data concerning the structure, the chemical composition and the radioelement contents at the concerned size level are required. Where approximations are needed in describing the materials they can limit the accuracy of the calculated doses.

Additionally consideration should be given to the program input constraints. Since the main purpose of *DosiVox* was to create a user friendly interface to a flexible series of granular configurations there are limits to the complexity of the geometries that can be defined. In particular, the interface allows defining a grid with only 20 voxels in each direction. The user has then to choose wisely the dimensions of the geometry he wants to reproduce, considering the particle transport characteristics, the sample complexity, and possible edge effects, to ensure that the requested accuracy can be reached. Nevertheless, the user can define a higher resolution, as it was done in the last example, in loading in *DosiVox* 3D images.

Finally it is important to remember the limitations imposed by the models describing the physical interactions: the physics models available in *Geant4* do not perfectly reproduce the behavior of the particles , leaving small but non-zero errors induced by the modeling of the particle-matter interactions. An important parameter of the model is the secondary particle production cut-off, expressed as a range cut value and which can be chosen using the graphical interface or editing the pilot text file. This value is a limit in range for secondary particle production, below which these particles are not explicitly simulated by *Geant4*, but are replaced by a local energy deposition (this process allows avoiding any infrared divergence). Considering the range of the α-particles and the very diffusive path of the β-particles in sediment, sub micron cut-off values are recommended for these radiations. Above this value, simulation runs are considerably faster but the dose deposited in volumes with dimensions lower than a millimeter can be significantly biased. If one wants to set a cut in range higher than the micrometer for β- and α-particles, we recommend testing the simulation with a

smaller cut, to estimate the difference in the results.

Finally, one has to remember that the numbers manipulated by the processors of our computers often contain indeterminations related to conversions between the binary and decimal systems. These indeterminations can lead to small errors, which accumulate in particular when considering large sums of small numbers, as it can be the case for dose calculation.

5. Conclusions

The *DosiVox* software allows modeling numerous different configurations for which simulations are required for dosimetric calculations. For dating, when considering the appropriate data set and making reasonable hypotheses, it is possible to model a sample in its environment, to define the different materials and their radioactive contents and finally, to run simulations for calculating the dose rate to which it is exposed.

The graphical interface and the possibility of editing the pilot text file allow non-programmer users to easily create their own models and run their simulations. However, a minimal investment about the functioning of both the interface and the program remains necessary, considering the variety of parameters that have to be defined. Skills about image processing can be considerable, as much for creating complex geometrical models for inputting in the voxelised detector as well as for processing the images representing the deposited dose.

With actual computers, statistically accurate simulations require few hours to several days, but it is still possible to run several parallel simulations in the limits of the computing resources at hand (for instance in using several processing cores) and to compile the results of each of them. Clusters or multi-core computers are useful tools for this task as well.

DosiVox can then be freely downloaded at the following address: http://www.iramat-crp2a.cnrs.fr/spip/spip.php?article144.

Acknowledgments

The authors are grateful to Hélène Coqueugniot and Priscilla Bayle from the PACEA laboratory (Bordeaux, France) who provided the micro-scanner tomography images. We also thank Makoto Asai from SLAC (Stanford University, CA, USA) for his help concerning geometry navigation and optimization in *Geant4*, and Mathieu Karamitros from CENBG (Gradignan, France) for useful advice in programming. This work has been supported by the LaScArBx (Labex Sciences Archéologiques de Bordeaux) *ANR-10-LABX-52* and by the Conseil Régional d'Aquitaine DOSIART project.

References

Abràmoff, M.D., Magalhães, P.J., and Ram, S.J. *Image Processing with ImageJ*. Biophotonics International, 11(7): 36–42, 2004.

Agostinelli, S., Allison, J., Amako, K., Apostolakis, J., Araujo, H., Arce, P., Asai, M., Axen, D., Banerjee, S., Barrand, G., Behner, F., Bellagamba, L., Boudreau, J., Broglia, L., Brunengo, A., Burkhardt, H., Chauvie, S., Chuma, J., Chytracek, R., Cooperman, G., Cosmo, G., Degtyarenko, P., Dell'Acqua, A., Depaola, G., Dietrich, D., Enami, R., Feliciello, A., Ferguson, C., Fesefeldt, H., Folger, G., Foppiano, F., Forti, A., Garelli, S., Giani, S., Giannitrapani, R., Gibin, D., Cadenas, J.J. Gómez, Gonzlez, I., Abril, G. Gracia, Greeniaus, G., Greiner, W., Grichine, V., Grossheim, A., Guatelli, S., Gumplinger, P., Hamatsu, R., Hashimoto, K., Hasui, H., Heikkinen, A., Howard, A., Ivanchenko, V., Johnson, A., Jones, F.W., Kallenbach, J., Kanaya, N., Kawabata, M., Kawabata, Y., Kawaguti, M., Kelner, S., Kent, P., Kimura, A., Kodama, T., Kokoulin, R., Kossov, M., Kurashige, H., Lamanna, E., Lampén, T., Lara, V., Lefebure, V., Lei, F., Liendl, M., Lockman, W., Longo, F., Magni, S., Maire, M., Medernach, E., Minamimoto, K., de Freitas, P. Mora, Morita, Y., Murakami, K., Nagamatu, M., Nartallo, R., Nieminen, P., Nishimura, T., Ohtsubo, K., Okamura, M., O'Neale, S., Oohata, Y., Paech, K., Perl, J., Pfeiffer, A., Pia, M.G., Ranjard, F., Rybin, A., Sadilov, S., Salvo, E. Di, Santin, G., Sasaki, T., Savvas, N., Sawada, Y., Scherer, S., Sei, S., Sirotenko, V., Smith, D., Starkov, N., Stoecker, H., Sulkimo, J., Takahata, M., Tanaka, S., Tcherniaev, E., Tehrani, E. Safai, Tropeano, M., Truscott, P., Uno, H., Urban, L., Urban, P., Verderi, M., Walkden, A., Wander, W., Weber, H., Wellisch, J.P., Wenaus, T., Williams, D.C., Wright, D., Yamada, T., Yoshida, H., and Zschiesche, D. *Geant4–a simulation toolkit*. Nuclear Instruments and Methods in Physics Research Section A: Accelerators, Spectrometers, Detectors and Associated Equipment, 506(3): 250–303, 2003.

Aitken, M.J. *Thermoluminescence Dating*. Academic Press, London, 1985.

Aitken, M.J., Clark, P.A., Gaffney, C.G., and Løvborg, L. *Beta and gamma gradients*. Nuclear Tracks and Radiation Measurements, 10(4-6): 647–653, 1985.

Allison, J., Amako, K., Apostolakis, J., Araujo, H., Dubois, P.A., Asai, M., Barrand, G., Capra, R., Chauvie, S., Chytracek, R., Cirrone, G.A.P., Cooperman, G., Cosmo, G., Cuttone, G., Daquino, G.G., Donszelmann, M., Dressel, M., Folger, G., Foppiano, F., Generowicz, J., Grichine, V., Guatelli, S., Gumplinger, P., Heikkinen, A., Hrivnacova, I., Howard, A., Incerti, S., Ivanchenko, V., Johnson, T., Jones, F., Koi, T., Kokoulin, R., Kossov, M., Kurashige, H., Lara, V., Larsson, S., Lei, F., Link, O., Longo, F., Maire, M., Mantero, A., Mascialino, B., McLaren, I., Lorenzo, P.M., Minamimoto, K., Murakami, K., Nieminen, P., Pandola, L., Parlati, S., Peralta, L., Perl, J., Pfeiffer, A., Pia, M.G., Ribon, A., Rodrigues, P., Russo, G., Sadilov, S., Santin, G., Sasaki, T., Smith, D., Starkov, N., Tanaka, S., Tcherniaev, E., Tome, B., Trindade, A., Truscott, P., Urban, L., Verderi, M., Walkden, A., Wellisch, J.P., Williams, D.C., Wright, D., and Yoshida, H. *Geant4 developments and applications*. Nuclear Science, IEEE Transactions on, 53(1): 270–278, Feb 2006.

Aso, T., Kimura, A., Yamashita, T., and Sasaki, T. *Optimization of patient geometry based on CT data in GEANT4 for medical application*. Nuclear Science Symposium Conference Record, 2007.NSS '07. IEEE, Volume 4, 2007.

Baró, J., Sempau, J., J.M.Fernández-Varea, and Salvat, M. *PENELOPE: an algorithm for Monte Carlo simulation of the penetration and energy loss of electrons and positrons in matter*. Nuclear Instruments Methods in Physics Research B, 100: 31–46, 1995.

Bayle, Priscilla, Braga, José, Mazurier, Arnaud, and Macchiarelli, Roberto. *Dental developmental pattern of the Neanderthal child from Roc de Marsal: a high-resolution 3D analysis.* Journal of human evolution, 56(1): 66–75, January 2009.

Bell, W.T. *Alpha dose attenuation in quartz grain for thermoluminescence dating*. Ancient TL, 12: 4–8, 1980.

Fleming, S.J. *Thermoluminescence dating : refinement of the quartz inclusion method*. Archaeometry, 12: 133–147, 1970.

Guérin, G., Mercier, N., Nathan, R., Adamiec, G., and Lefrais, Y. *On the use of the infinite matrix assumption and associated concepts: a critical review. Radiation Measurements*. Radiation Measurements, 47: 778–785, 2012.

Incerti, S., Seznec, H., Simon, M., Barberet, Ph., Habchi, C., and Moretto, Ph. *Monte Carlo dosimetry for targeted irradiation of individual cells using a microbeam facility*. Radiation Protection Dosimetry, 133: 2–11, 2009.

Ivanchenko, V., Apostolakis, J., Bagulya, A., Abdelouahed, H.B., Black, R., Bogdanov, A., Burkhard, H., Chauvie, S., Cirrone, P., Cuttone, G., Depaola, G., Di Rosa, F., Elles, S., Francis, Z., Grichine, V., Gumplinger, P., Gueye, P., Incerti, S., Ivanchenko, A., Jacquemier, J., Lechner, A., Longo, F., Kadr, O., Karakatsanis, N., Karamitros, M., Kokoulin, R., Kurashige, H., Maire, M., Mantero, A., Mascialino, B., Moscicki, J., Pandola, L., Perl, J., Petrovic, I., Ristic-Fira, A., Romano, F., Russo, G., Santin, G., Schaelicke, A., Toshito, T., Tran, H., Urban, L., Yamashit, T., and Zacharatou, C. *Recent improvements in Geant4 electromagnetic physics models and interfaces*. Progress in Nuclear. Science and Technology, 2: 898–903, 2011.

Mejdahl, V. *Thermoluminescence dating: beta-dose attenuation in quartz grains*. Archaeometry, 21: 61–73, 1979.

Ollion, Jean, Cochennec, Julien, Loll, François, Escudé, Christophe, and Boudier, Thomas. *TANGO: a generic tool for high-throughput 3D image analysis for studying nuclear organization.* Bioinformatics (Oxford, England), 29(14): 1840–1841, July 2013.

Rasband, W.S. *ImageJ, U.S. National Institutes of Health, Bethesda, Maryland, USA*, 1997–2012. imagej.nih.gov/ij/.

Schneider, C.A., Rasband, W.S., and Eliceiri, K.W. *NIH Image to ImageJ: 25 years of image analysis*. Nature Methods, 671: doi:10.1038/nmeth.2089, 2012.

Sempau, J., Fernández-Varea, J.M., Acosta, E., and Salvat, F. *Experimental benchmarks of the Monte Carlo code PENELOPE*. Nuclear Instruments and Methods in Physics Research B, 207: 107–123, 2003.

Zimmerman, D.W. *Thermoluminescent dating using fine grains from pottery*. Archaeometry, 10: 26–28, 1971.

Reviewer

David Sanderson

Ancient TL

A portable system of X-ray irradiation and heating for electron spin resonance (ESR) dating

Frank Oppermann,[1*] and Sumiko Tsukamoto[1]

[1]Leibniz Institute for Applied Geophysics, Hannover 30655, Germany

[*]E-mail: Frank.Oppermann@liag-hannover.de and Sumiko.Tsukamoto@liag-hannover.de

Received: December 18, 2014; in final form: April 27, 2015

Abstract

In this study we present details of a portable system which contains an X-ray source and heater, designed to irradiate and heat samples within a quartz glass tube for electron spin resonance (ESR) dating. The spatial distribution of the X-ray beam was measured with a radiation sensitive film and the images were scanned and mapped using the Risoescan software. The reproducibility of irradiations was checked by multiple irradiations to alanine. The results confirmed that X-ray irradiations give reproducible doses to samples. The heating component can heat samples between 100°C and 600°C and can be used for preheating after irradiation and for resetting the natural signal for regeneration.

Keywords: ESR dating, X-ray irradiation, heater, spatial uniformity

1. Introduction

In electron spin resonance (ESR) dating the multiple aliquot additive dose (MAAD) method has been predominantly used for equivalent dose (D_e) estimation (see reviews of Grün, 1989; Rink, 1997; Schellmann et al., 2008). One of the problems of the multiple aliquots approach is scattering of signal intensity between different aliquots, which could lead to a large uncertainty in D_e. To avoid such problems single aliquot methods can be used, however, these methods are only practically possible if a radiation source is located close to an ESR spectrometer. In order to make a single aliquot procedure more feasible for ESR dating, we have developed a portable system which consists of a small X-ray tube (Varian VF-50J) with a maximum energy of 50 kV and a heater; the latter is both for preheating after X-ray irradiation and for signal resetting for regenerative dose estimations. The same type of X-ray tube has been used for automated luminescence readers (Hashimoto et al., 2002; Andersen et al., 2003). Here we report the design and performance of our mini X-ray/heating system. An X-ray irradiation system for ESR dating using a larger X-ray source with a maximum energy of 200 kV has been developed and reported by Grün (2012).

2. Apparatus and software

Fig. 1a shows a photograph and the schematic diagram of the system. The system is designed to irradiate and heat samples within Wilmad Suprasil quartz glass tubes with 3 mm outer diameter (2 mm inner diameter) and 159 mm long. The X-ray components are: a Varian VF-50J X-ray tube with tungsten target (4-50 kV high voltage, 5 mA emission current and 50 W maximum power) and a Spellman high voltage generator MNX50P50 which can produce high voltage (UHV) of 0-50 kV with an emission current (IE) up to 2 mA but limited to 50 W power (Fig. 1b). The power supply has a stability of 0.05% per 8 hours after 0.5 hour warm up with a temperature coefficient of 0.01%/°C (supplier information). To minimize any warm-up effects, the filament is always preheated at a current of 1.7 A. We also monitor the tube voltage, emission current, filament current and filament voltage.

The generated X-rays are emitted through a 76 μm beryllium end window of the tube. The X-ray components are located within a lead chamber (w x h x l = 80 x 120 x 40 mm) with 10 mm thick walls (Fig. 1b). The distance between the beryllium window and the sample tube is 30.5 mm. The X-ray beam has a diameter of 56 mm at the sample position. To reduce the effect of low energy components of X-rays a 200 μm aluminum filter has been inserted between the beryllium window and the sample position as suggested by

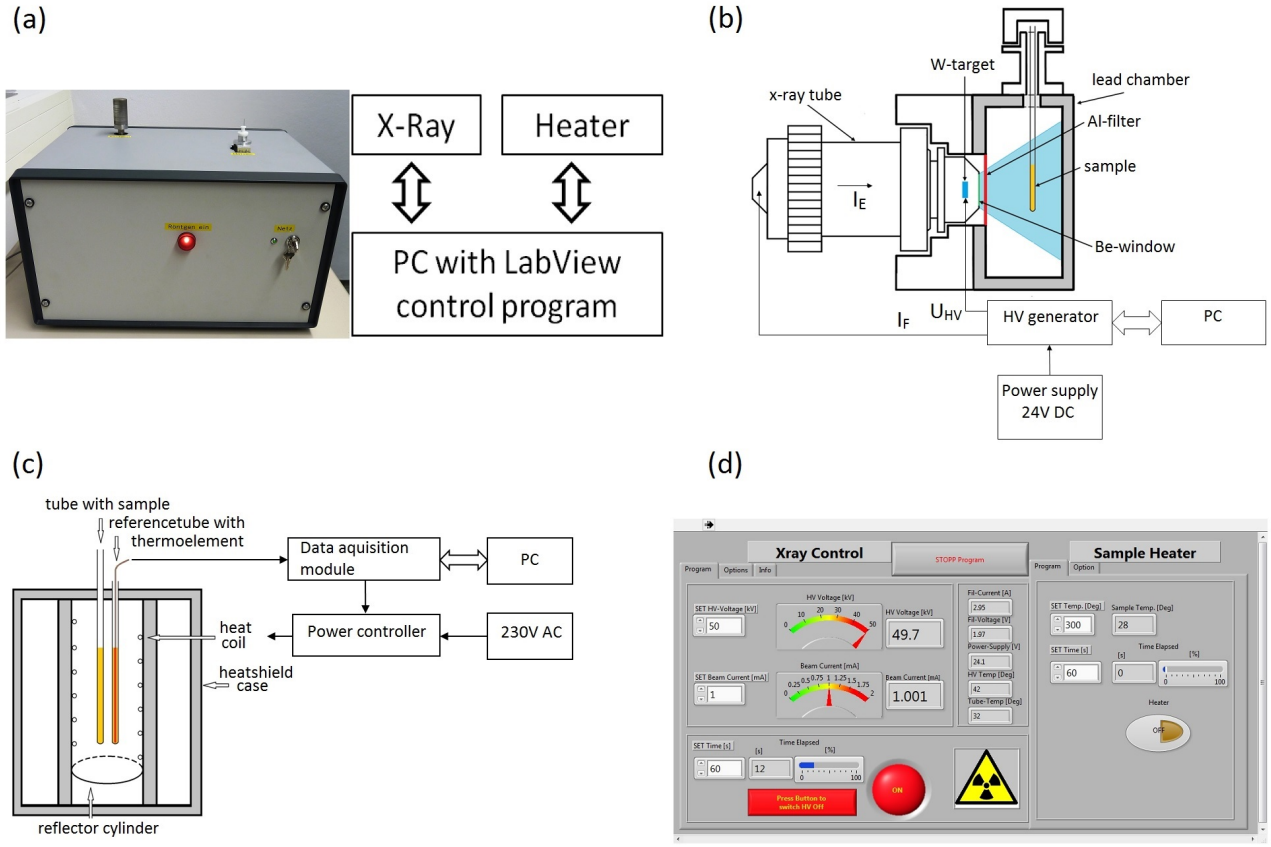

Figure 1. (a) Photograph and schematic diagram of the X-ray/heating system, and diagrams for (b) X-ray, (c) heater components and (d) software GUI.

Yawata & Hashimoto (2004) and Thomsen et al. (2006).

The heater can control the sample temperature within a tube between 100°C and 600°C. The sample tube is inserted beside a reference tube, which monitors the temperature within a steel reflector cylinder in a heat shield case (Fig. 1c). The heat energy is transmitted equally to the two tubes by a heat coil powered by a power controller, and a difference less than 1% between the two tubes was monitored. The reference temperature is measured with a data acquisition module using the thermoelement inside the reference tube.

The system is controlled by a Software-GUI written in LabView. Fig. 1d shows a screenshot of the program. In the X-ray control part (left) the high voltage [kV], the beam current [mA] and the exposure time [s] can be set by users. The actual high voltage, beam current, elapsed exposure time and other secondary parameters are monitored and shown on the screen. In the sample heater part (right) the sample temperature [deg] and the heating time [s] can be entered. The timer starts when the temperature reaches ± 5°C of set temperature. The reference temperature and elapsed heating time are monitored.

3. Spatial uniformity of the X-ray

The spatial uniformity of the X-ray beam was measured by taking images with a radiation sensitive film (Gafchromic HD-810) by irradiating for 3 different time intervals (50 kV, 1 mA for 200 s, 400 s and 600 s of irradiation) at the sample position without a sample tube and inside a quartz glass tube. These X-ray images were first scanned. The chromaticity of the images was calibrated into relative dose rate, and the distribution of the dose rate was mapped by the dosimetry software RisøScan (Helt-Hansen & Miller, 2004).

Fig. 2a shows the spatial dose distribution of the X-ray beam at the sample position for an irradiation time of 400 s. Fig. 2b shows the axial dose distribution inside the sample tube. The results indicate that the area of ∼ 1 cm diameter in the centre receives a relatively uniform irradiation of ± 1.6% precision. The position of the sample tube was chosen as to allow uniform irradiation of samples with a height of up to ∼ 1 cm (Fig. 2b). If ESR signals resulting from 1 cm sample height are too weak, it is possible to increase the height (and thus the amount of sample) up to 2 cm. The irradiation uniformity decreases to 3.1% for 1.5 cm sample height and 5.6% for 2 cm sample height, respectively. In order to avoid accumulation of non-uniformities by multiple irradiations of a single sample, and also to avoid signals originating

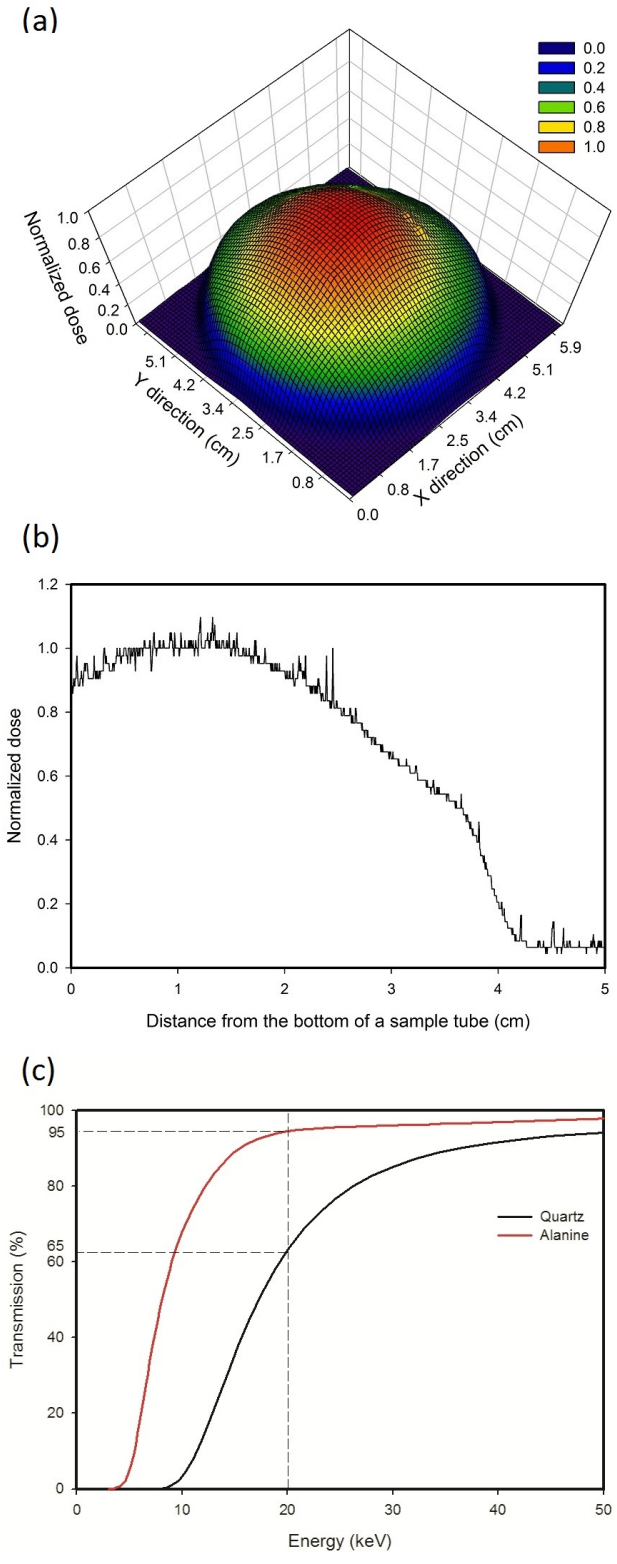

Figure 2. Spatial uniformity of the X-ray beam (a) horizontal cross-section at sample position (b) vertical cross-section thorugh a sample tube and (c) energy dependent transmission of X-ray intensity through 1 mm thick samples of alanine and quartz.

from the quartz glass tube itself, the tubes were sealed with parafilm and the tubes are turned upside down during each irradiation (Tsukamoto et al., 2015).

The comparison between the film images taken without a tube and inside the tube revealed that the wall of the quartz glass tube absorbed $\sim$ 60% X-ray dose. This was confirmed by a comparative irradiation experiment using 2 aliquots of 25 mg alanine; one was irradiated within a quartz glass tube the other was irradiated in a plastic straw with 3 mm diameter. The ESR signal intensity of the alanine irradiated inside the quartz glass tube was only 34% of the one irradiated in a plastic straw. Fig. 2c shows the energy dependent transmission of X-ray intensity through 1 mm thick samples (alanine and quartz) within a tube. The transmission was calculated assuming that a sample tube is filled with alanine or sand sized quartz with 30% porosity. At the peak energy of 20 kV the X-ray transmission (Andersen et al., 2003) between the inner surface and the centre of the tube is about 95% for alanine and about 65% for quartz. Therefore it would be better to rotate and/or vibrate tubes during irradiation in order to improve the uniformity of dose to sample grains and we plan to integrate such a mechanical function into the system in the near future.

4. Performance and calibration of the X-ray source

The dose response of X-ray irradiated alanine was compared with and without rotations in order to check the reproducibility of irradiations. One set of aliquots was irradiated with X-rays (50 kV, 1 mA) for 200 s without rotation. For the other set tubes were manually rotated 90° every 50 s during the 200 s irradiation. This process was repeated 4 times for each aliquot. Altogether 6 aliquots were measured (3 aliquots each with and without rotations). Each aliquot contained 50 mg of alanine. The 50 mg of alanine had a height of $\sim$ 2 cm in a quartz glass tube, which resulted in less homogeneous irradiations, however, signals for a smaller amount of material were too weak and irreproducible. ESR measurements were performed with a JEOL FA-100 with 2 mW microwave power, 0.3 mT modulation amplitude, and 20 mT sweep width. The scan time was 30 s and spectra were accumulated 3 times. The signal intensity around g = 2.003 was measured. Fig. 3a shows the increase of the alanine ESR signal intensity versus X-ray exposure time. Average intensities obtained from 3 aliquots (with and without rotations) and their 1-σ standard errors were plotted. Although a full penetration of X-rays throughout the thickness of samples was not expected (Fig. 2c), the intensities with and without rotations during irradiations are indistinguishable. We therefore conclude that rotations do not improve the homogeneity of our X-ray irradiations at least for alanine. The normalised increase of alanine ESR signals after each 200 s irradiation is shown in Fig. 3b as a histogram. The relative standard deviation of each measurement is 5.2%, including all other sources of measurement errors (e.g. adjusting heights of

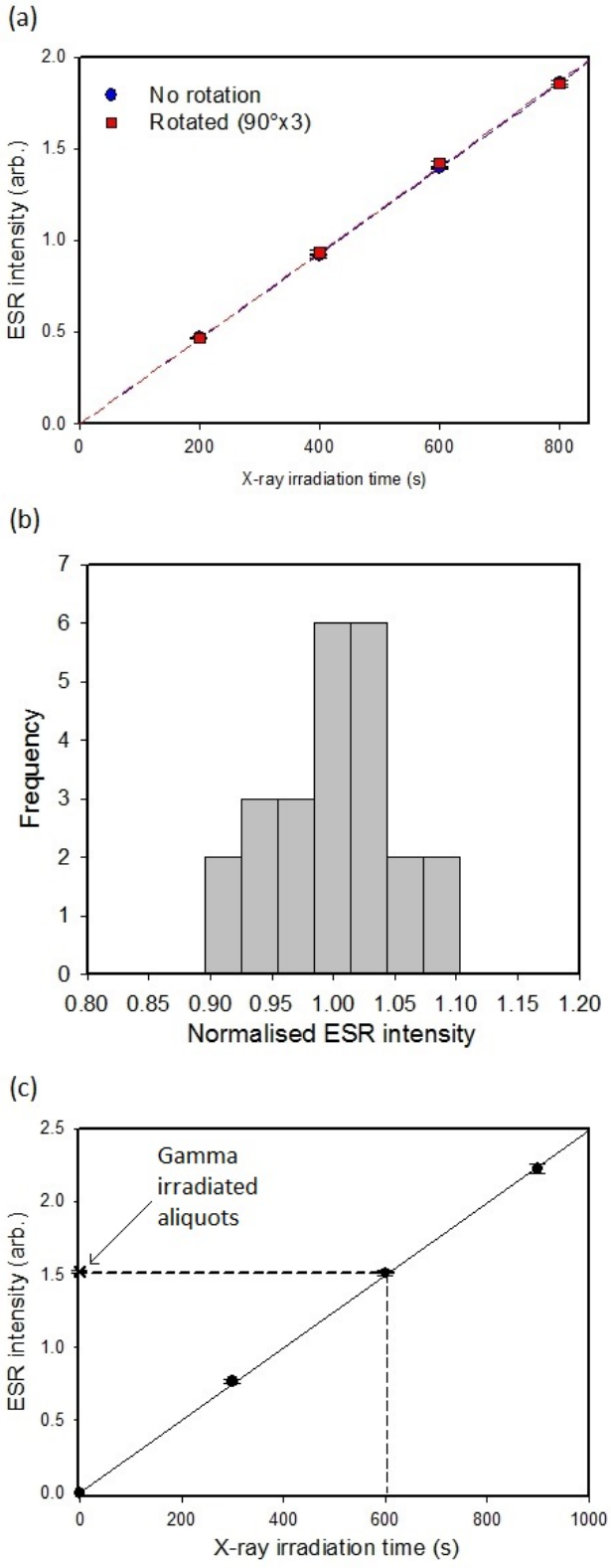

Figure 3. (a) Comparison of X-ray dose response curves with and without rotation during irradiations. (b) Histogram of relative alanine signal increase following 200 s irradiations. (c) Calibration of X-ray dose rate for alanine.

sample tubes at the irradiation and ESR measurement positions, and tuning of the microwave).

To calibrate the X-ray dose rate for alanine, 2 sets of aliquots were prepared. One set received a gamma dose in alanine of 75.2 Gy from a ^{60}Co source at the Technical University of Denmark. Another set of aliquots was irradiated with the X-ray and the intensities of the alanine radical for the gamma and X-ray irradiated aliquots were compared (Fig. 3c). Three aliquots each of gamma and X-ray irradiated aliquots were measured. The X-ray irradiation time which is equivalent to 75.2 Gy gamma dose was calculated as 603 $\pm$ 10 s. The resulting X-ray dose rate for alanine was thus 0.125 $\pm$ 0.002 Gy/s.

Our portable X-ray system provides the opportunities to conduct reproducible single aliquot ESR measurements, however, there is one disadvantage of using X-ray for artificial irradiation. Due to the low energy photons from the X-ray tube, the photoelectric effect dominates the energy transfer process, which depends on the atomic number of sample materials. Thus, calibration of the X-ray dose rate must be performed for each different material; the X-ray dose rate for quartz has been calibrated to 0.34 $\pm$ 0.01 Gy/s (Tsukamoto et al., 2015). Nevertheless this system provided us with the first opportunity to test the single aliquot regenerative dose method combined with preheat plateau tests using quartz ESR and therefore contributed to methodological developments in ESR dating (Tsukamoto et al., 2015).

5. Summary

This manuscript presents the details of our portable X-ray irradiation/heating system, which can be used to measure single aliquot equivalent doses in ESR dating. Although the experimental data with alanine showed that the reproducibility of the X-ray irradiation is not depending on the rotation of the sample tubes, for samples with higher density it might be advisable to rotate and/or vibrate the tubes. While using a higher energy X-ray tube is an alternative solution for the uniformity problem it would significantly increase cost and space requirements. The price for our system in total is approx.8000 Euro and it can easily fit on a desk. A higher energy system is about 20-30 times more expensive than the mini X-ray and needs much more space.

Acknowledgments

We thank Jakob Helt-Hansen, Torben Lapp, Jim Thorslund Andersen and Kristina Thomsen (Technical University of Denmark) for mapping the uniformity of X-ray irradiations and for gamma irradiations. Karsten Vollmer is thanked for his work on the lead chamber. Gudrun Drewes and Sonja Riemenschneider are thanked for their technical help. The constructive comments from David Sanderson and Regina DeWitt have greatly helped improve the paper.

References

Andersen, K., Bøtter-Jensen, L., and Murray, A.S. *A mini X-ray generator as an alternative to a $^{90}Sr/^{90}Y$ beta source in luminescence dating*. Radiation Measurements, 37: 557–561, 2003.

Grün, R. *Electron spin resonance (ESR) dating*. Quaternary International, 1: 65–109, 1989.

Grün, R. *Ionization efficiencies of alanine dosimeters and tooth enamel irradiated by gamma and X-ray sources*. Radiation Measurements, 47: 665–668, 2012.

Hashimoto, T., Nakagawa, T., Hong, D.G., and Takano, M. *An automated system for both red/blue thermoluminescence (TL) and optically stimulated luminescence (OSL) measurement*. Journal of Nuclear Science and Technology, 39: 108–109, 2002.

Helt-Hansen, J. and Miller, A. *RisøScan a new dosimetry software*. Radiation Physics and Chemistry, 71: 359–362, 2004.

Rink, W.J. *Electron spin resonance (ESR) dating and ESR applications in Quaternary science and archaeometry*. Radiation Measurements, 27: 975–1025, 1997.

Schellmann, G., Beerten, K., and Radtke, U. *Electron spin resonance (ESR) dating of Quaternary materials*. Quaternary Science Journal, 57: 150–178, 2008.

Thomsen, K.J., Bøtter-Jensen, L., Denby, L., and Murray, A.S. *Luminescence response to irradiation using mini X-ray generators*. Nuclear Instrumentas and Methods B, 252: 267–275, 2006.

Tsukamoto, S., Toyoda, S., Tani, A., and Oppermann, F. *Single aliquot regenerative dose method for ESR dating using X-ray irradiation and preheat*. Radiation Measurements, in press, doi:10.1016/j.radmeas.2015.01.018, 2015.

Yawata, T. and Hashimoto, T. *Availability of a small X-ray tube combined with Al-absorber as a new irradiator for luminescence researches*. Radioisotopes, 53: 207–212, 2004. (in Japanese with English abstract).

Reviewer

David Sanderson

Ancient TL

A new R function for the Internal External Uncertainty (IEU) model

Rachel K. Smedley[1]*

[1] Department of Geography and Earth Sciences, Aberystwyth University, Ceredigion, SY23 3DB, UK

*E-mail: rks09@aber.ac.uk

Received: March 24, 2015; in final form: May 26, 2015

Abstract

A new function (*calc_IEU*) is now available in the latest version of the R Luminescence package (version 0.4.2). The *calc_IEU* function can be used to calculate an equivalent dose (D_e) value for a given dose distribution using the Internal External Uncertainty (IEU) model. The IEU model is used in luminescence dating to determine a D_e value for a partially-bleached sample by calculating the weighted mean from the well bleached part of a partially-bleached population. The new *calc_IEU* function automates the calculation of the IEU model so that the results are produced rapidly and reproducibly. This is advantageous as the user can easily perform sensitivity tests of the model in response to changing input parameters.

Keywords: R, luminescence dating, Internal External Uncertainty (IEU) model, single grains

1. Introduction

The Internal External Uncertainty (IEU) model can be used to determine an equivalent dose (D_e) value for luminescence dating of a partially-bleached sample (Thomsen et al., 2007). The D_e value is calculated as the weighted mean from the grains in a partially-bleached population that the IEU model identifies to have been well bleached upon deposition. The IEU model has been successfully used in a number of studies to provide D_e values for sedimentary samples using both single grains and multiple grains (e.g. Reimann et al., 2012; Medialdea et al., 2014; Sim et al., 2014). A new function that automates the calculation of the IEU D_e value is now available in the latest version of the R Luminescence package (version 0.4.2; Kreutzer et al., 2012). The *calc_IEU* function aims to automate the calculations of the IEU model for luminescence dating, in addition to providing output features that rapidly assess the sensitivity of the IEU model to changing input parameters. The purpose of this work is to explain the calculations of the *calc_IEU* function and provide a worked example of the function using D_e values determined for single grains of quartz from a glaciofluvial sample taken from the U.K. that was partially bleached upon deposition (sample T4CEIF01; Fig. 1a).

2. The IEU model

The IEU model is based on the assumption that the well-bleached grain population in the dose distribution from a poorly-bleached sample is normally distributed, and that this population can be identified if the uncertainties assigned to individual dose estimates adequately describe the observed variability. It is standard practise to determine the uncertainties on individual D_e values from intrinsic sources (i.e. counting statistics, the instrument reproducibility and the dose-response curve fitting). Extrinsic factors such as heterogeneity of the beta dose-rate for individual grains may also cause variability in a dataset. Ideally, the uncertainty arising extrinsically for a given suite of samples is determined from a sample that has been well bleached in the natural environment, meaning that factors such as microdosimetry are considered within the uncertainty estimate. However, it is often difficult to determine this information for all samples due to the lack of analogue well-bleached sediments in certain depositional settings (e.g. glaciofluvial). Alternatively, Thomsen et al. (2007) use a number of gamma dose-recovery experiments, administering progressively larger given doses to measure the minimal amount of scatter expected in a well-bleached D_e distribution. The authors plot the absolute overdispersion values (in Gy) determined from these experiments against the CAM D_e values and fit a linear function to the data to determine the change in overdispersion with in-

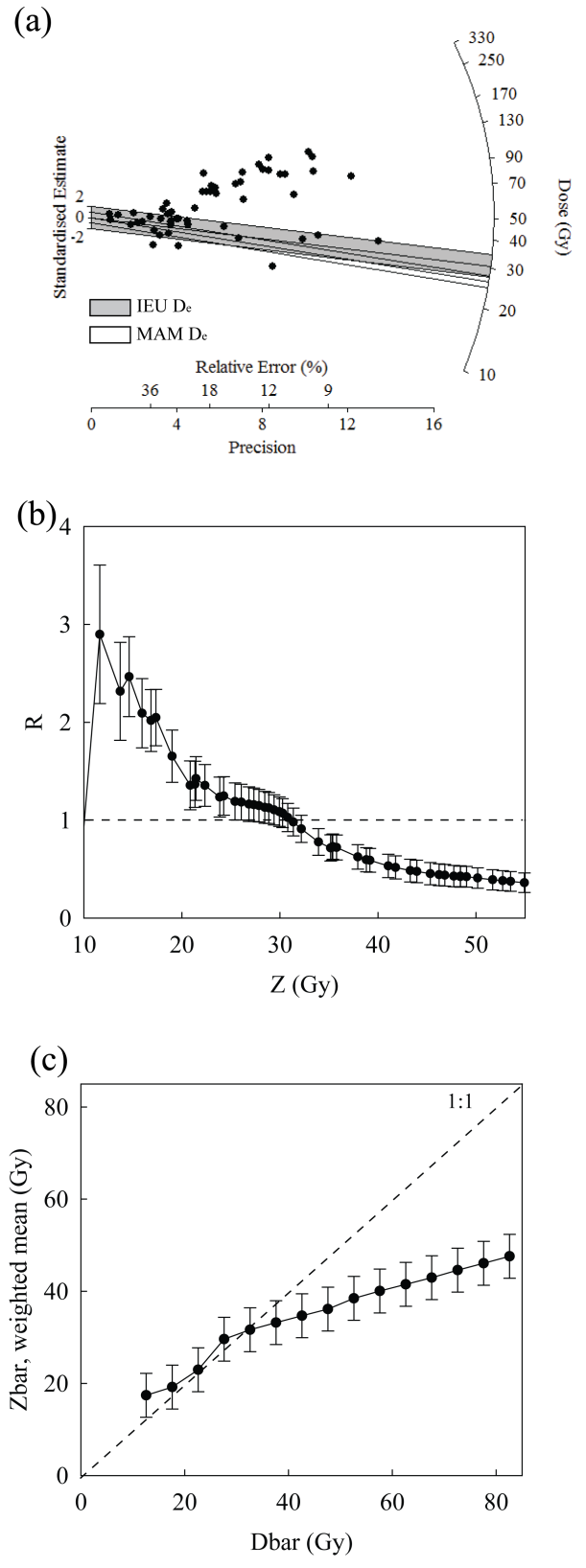

Figure 1. Results from applying the IEU model to D_e values determined from single grains of quartz from a partially-bleached sample taken from a glaciofluvial setting in the U.K. (sample T4CEIF01): (a) the D_e values are presented in a radial plot; (b) the values of *R* calculated for the final iteration of *Dbar* when determining the IEU D_e value for this dataset are plotted against Z; and (c) the output plot from calculating *Zbar* using fixed values of *Dbar* when a = 0.3

creasing given dose. In the IEU model the slope of this linear function is termed the *a* value, which by definition is similar to the σ_b value in the Minimum Age Model (MAM; Galbraith et al., 1999), while the intercept provides the *b* value, which defines how much overdispersion is expected in a D_e distribution for a 0 Gy dose (e.g. the absolute overdispersion which can be obtained from thermal transfer experiments).

The uncertainty on each individual D_e value can then be calculated using the uncertainty arising from counting statistics (σ_c^2), the *a* and *b* values, and the burial dose (*Dbar*) in Eq. 1 (Thomsen et al., 2007).

$$\sigma_{tot} = \sqrt{\sigma_c^2 + (a \cdot Dbar + b)^2} \qquad (1)$$

The value of *Dbar* in Eq. 1 is initially unknown and so Thomsen et al. (2007) suggest that it should be solved using an iterative approach. To iterate *Dbar*, an initial *Dbar* value is substituted into Eq. 1, and the total uncertainty assigned to each D_e value is calculated (σ_{tot}). The internal/external consistency criterion (Eqs. 2, 3 and 4) is then used to determine which grains (or aliquots) from the partially-bleached population were well bleached upon deposition (Thomsen et al., 2003). The weighted mean dose (termed *Z*) of the identified well-bleached part of the partially-bleached population is then calculated and compared to the value of *Dbar*. If *Z* is not equal to *Dbar*, the calculation of *Z* is repeated again using a new value of *Dbar*. This iteration process is continued until *Z* is equal to *Dbar*, where *Z* is calculated using only the grains (or aliquots) that are deemed to form the well-bleached part of the partially-bleached distribution (i.e. $R = 1$, see below). This value of *Z* that is equal to *Dbar* is the burial dose determined for this sample (termed the IEU D_e value in the *calc_IEU* function).

To calculate the internal/external consistency criterion the D_e values in a given distribution are first ranked from the smallest D_e value to the largest D_e value. Eq. 2 is then used to calculate the weighted mean (*Z*), where D_i are the individual D_e values, σ_i are the individual estimates of uncertainty for D_i and *N* is the total number of D_i.

$$Z = \frac{\sum_{i=1}^{N} D_i / \sigma_i^2}{\sum_{i=1}^{N} 1 / \sigma_i^2} \qquad (2)$$

The standard error of *Z* is then calculated in two ways: (1) as an internal measure (α^2_{in}) which is dependent upon how much variation there is within the counting statistics (Eq. 3); and (2) as an external measure (α^2_{ex}) which also is dependent upon how much variation arises from each individual D_e estimate varying from the mean (Eq. 4) (Topping, 1955; Thomsen et al., 2003).

$$\alpha^2_{in} = \frac{1}{\sum_{i=1}^{N} 1 / \sigma_i^2} \qquad (3)$$

$$\alpha^2_{ex} = \frac{\sum_{i=1}^{N} (D_i - Z)^2 / \sigma_i^2}{(N-1) \sum_{i=1}^{N} 1 / \sigma_i^2} \qquad (4)$$

Using these measures, the internal/external consistency criterion can be calculated from $R = \alpha^2_{in} / \alpha^2_{ex}$, where the

uncertainty on R is $(2(n-1))^{-0.5}$ and n is the number of data points used for the calculations. R is calculated cumulatively, starting with the lowest two D_e values and finishing with including all the D_e values into the calculation. All the grains (or aliquots) included in the calculation of an R value ≥ 1 are deemed to form the well bleached part of the partially-bleached population (e.g. Fig. 1b), and Z is calculated from only these grains (or aliquots).

3. The *calc_IEU* function: a worked example

The *calc_IEU* function works in a similar way to the existing age models built into the R 'Luminescence' package. It first requires the input of a data frame containing two columns; (1) the D_e values and (2) the uncertainties of the D_e values. Input variables (or arguments) are also required to define the parameters used for the calculations in the function (e.g. *a* and *b*). The following section works through an example of how to use the *calc_IEU* function and what outputs are produced. Fig. 1a shows a radial plot containing the D_e values for the example dataset determined from single grains of quartz from a glaciofluvial sample, which was partially bleached upon deposition. The individual estimates of uncertainty assigned to each D_e value shown in Fig. 1a are based on counting statistics, instrument reproducibility (measured as 2.5 %) and dose-response curve fitting. Similar to the σ_b value in MAM, accurate estimates of *a* and *b* values need to be considered for each sample. The uncertainty arising extrinsically for this sample was estimated from the overdispersion value determined for a sample from this environment that was naturally well bleached upon deposition; *a* and *b* values for this sample were estimated to be 0.30 and 0.01, respectively. To call the *calc_IEU* function the user is required to adapt the arguments written below, defining the correct input parameters where necessary (e.g. *a* and *b* values).

```
calc_IEU(data = data, a = 0.30, b = 0.01, interval
    = 5, trace = FALSE, verbose = TRUE, plot =
    TRUE)
```

data	**data.frame** (required): containing two columns; D_e and D_e uncertainties
a	**numeric** (required): slope (e.g. 0.30)
b	**numeric** (required): intercept (e.g. 0.01)
interval	**numeric** (required): interval used for fixed iteration of Dbar (e.g. 5 Gy)
trace	**logical**: print iteration of Dbar to screen (TRUE/FALSE)
verbose	**logical**: console output (TRUE/FALSE)
plot	**logical**: plot output (TRUE/FALSE)

Before the IEU D_e value is determined for a D_e distribution, the *calc_IEU* function will automatically calculate Z using fixed values of *Dbar* to assess whether there is more than one solution where $Z = Dbar$ ($R = 1$). Output plots of the results are provided to allow for comparisons if the user wishes to compare the influence of changing input parameter (e.g. *a*) or the characteristics of D_e distributions determined for different samples. Note that when performing the calculations of Z using a fixed value of *Dbar*, Z is referred to as *Zbar* to differentiate these calculations from the automatic iteration of *Dbar* used to calculate the IEU D_e value. The fixed values of *Dbar* range from an upper limit defined as the mean of the D_e distribution to a lower limit set as the lowest D_e value in the dataset. The *calc_IEU* function automatically determines the fixed values of *Dbar* from the upper limit to the lower limit by repeatedly subtracting the value defined in Gy by the argument *interval*. The size of the interval used will depend on the range of the D_e distribution. If the range in the D_e distribution is small then it would be advantageous to use smaller intervals to improve the resolution of the calculations. The calculations from using fixed values of *Dbar* to calculate *Zbar* are provided in an output table (e.g. Table 1), and the fixed values of *Dbar* are plotted against *Zbar* in an output plot (e.g. Fig. 1c).

Table 1 shows an example of what happens for the calculations when using fixed values of *Dbar*. The mean is first calculated for the D_e distribution, here it is 82.59 Gy, the fixed interval in Gy (i.e. 5 Gy) is then subtracted to determine the first *Dbar.fixed* value of 77.59 Gy. This *Dbar.fixed* value is then used to calculate R and determine how many grains form the well-bleached part of the D_e distribution. The weighted mean (*Zbar*) of these grains is then calculated and plotted against *Dbar.fixed* (e.g. Fig. 1c). The *calc_IEU* function will then automatically subtract 5 Gy from the present value of *Dbar* (i.e. 77.59 Gy) to set a new value of *Dbar.fixed* (i.e. 72.59 Gy) used to calculate the next value of *Zbar*. This process continues to be repeated until the function identifies that the value of *Dbar.fixed* is set as a value lower than the lowest D_e value, whence the *calc_IEU* function will cease calculations.

The fixed iteration of *Dbar* in Fig. 1c demonstrates that there are multiple solutions ranging from 17.6 to 32.6 Gy where $Dbar = Z$ and $R = 1$ for the example dataset used in this study, even though the final solution is determined to be (31.13 $\pm$ 2.54) Gy (see Table 2). In such cases, the IEU D_e value is the lowest value of Z that is equal to *Dbar*, because the model aims to determine a minimum dose from this D_e distribution. Given that there may be multiple solutions of the IEU model for some data sets, it is important that the automatic iteration of *Dbar* used to calculate the IEU D_e value begins by setting the first *Dbar* value equal to the lowest D_e value in the dataset and iterating to larger values of *Dbar*. Subsequent iterations of *Dbar* then automatically set Z that was calculated during the previous iteration as the new *Dbar*, and repeat the iterations until $Dbar = Z$ where $R = 1$.

The argument *trace* allows the user to print the results to the screen from the iterations of *Dbar* to calculate the IEU D_e value. The calculations of Z, α^2_{ex}, α^2_{in} and R used for the final iteration of *Dbar* that determines the IEU D_e value are provided in an output file, and the weighted mean (Z) is plotted against R in an output plot (e.g. Fig. 1b). A summary of the results from the IEU model are provided in an output

Dbar	Dbar.Fixed	Zbar	Zbar.Error	n	R	a	b
82.59	77.59	47.60	4.76	37	0.97	0.30	0.01
77.59	72.59	46.07	4.76	36	0.98	0.30	0.01
72.59	67.59	44.60	4.76	36	0.93	0.30	0.01
67.59	62.59	42.95	4.76	34	0.99	0.30	0.01
62.59	57.59	41.50	4.76	34	0.94	0.30	0.01
57.59	52.59	40.06	4.76	33	0.95	0.30	0.01
52.59	47.59	38.47	4.76	32	1.00	0.30	0.01
47.59	42.59	36.14	4.76	29	0.94	0.30	0.01
42.59	37.59	34.68	4.76	28	0.95	0.30	0.01
37.59	32.59	33.20	4.76	28	0.87	0.30	0.01
32.59	27.59	31.64	4.76	27	0.93	0.30	0.01
27.59	22.59	29.61	4.76	23	1.00	0.30	0.01
22.59	17.59	22.96	4.76	13	0.96	0.30	0.01
17.59	12.59	19.21	4.76	9	0.86	0.30	0.01
12.59	7.59	17.43	4.76	8	0.90	0.30	0.01

Table 1. Fixed iteration of *Dbar* determined for the example dataset using an *a* value of 0.30. The number of grains/aliquots determined to form the well-bleached part of the partially-bleached population is shown as *n*

file (e.g. Table 2), and contains the values for *Dbar, Z* (now referred to as the IEU D_e), the uncertainty on the D_e value, the number of D_e values defined as the well-bleached part of the partially-bleached population, and the *a* and *b* values used for the calculations. For the example dataset given in Fig. 1a, the IEU D_e value (31.13 Gy $\pm$ 2.54 Gy) determined using an *a* value of 0.30 was consistent with the MAM D_e value of (26.51 Gy $\pm$ 4.99 Gy), which was calculated using a σ_b value of 0.30 (Fig. 1a). An example of an R script that a user can copy to call the *calc_IEU* function and save the output files is shown below (after Burow, Pers. Comm.).

```
## Load library
library("Luminescence")
## Input data
setwd("C:/Users/Documents/R/EXAMPLE")
data <- read.table("Example.txt", header = F)
## Calculate the IEU model
pdf(paste0("IEU_Plots.pdf"))
IEU <- calc_IEU(data = data, a = 0.30, b = 0.01,
    interval = 5, trace = FALSE, verbose = TRUE,
    plot = TRUE)
dev.off()
## Write tables
tables <- get_RLum.Results(IEU, "tables")
for(i in seq_along(tables)) {
write.table(tables[[i]], file = paste0(names(
    tables)[i], ".txt"))
}
```

Dbar	IEU.D_e (Gy)	IEU.Error (Gy)	Number of D_e	a	b
31.13	31.13	2.54	26	0.3	0.01

Table 2. Results from calculating the IEU model for the example dataset shown in Fig. 1a.

Although it is not the case for the example dataset shown in this study, the IEU model may not always be able to determine a D_e value using the input parameters provided, and an error message will be produced by the *calc_IEU* function. It is likely that an error message is provided because the population of grains that are deemed to form the well bleached part of the partially-bleached distribution is less scattered than can be explained by the value of *a*. In such cases, it is likely that the value of *a* is too large and overestimates the amount of scatter in a D_e distribution determined from a well-bleached sample of this material; thus, the value of *a* needs revising for the IEU model to be able to calculate a D_e value for this sample.

4. Sensitivity of the IEU model to changing parameters

The outcome of any minimum age model that accounts for the uncertainties on individual D_e values (e.g. the IEU model and MAM) is critically dependent upon the accuracy of the individual uncertainties assigned. Where the assigned uncertainties are overestimated, such a statistical model will overestimate the number of grains that form the well-bleached part of the D_e distribution, and consequently overestimate the D_e value. Similarly, if the assigned uncertainties are too small then too few of the grains are determined to have been well-bleached upon deposition and the D_e value is underestimated. The uncertainties assigned to the individual D_e estimates must therefore be as accurate as possible in order to provide accurate D_e values for a given D_e distribution; this includes using appropriate estimates of *a* and *b* for the IEU model.

A major advantage of the *calc_IEU* function is that a rapid assessment of the sensitivity of the IEU model to different parameters (e.g. *a*) can be provided. This can be a useful tool for luminescence dating of sedimentary samples from the natural environment because it is often difficult to determine the amount of scatter arising from extrinsic factors, such as external microdosimetry. Previous studies using single-grain and multiple-grain dating of quartz have reported that the

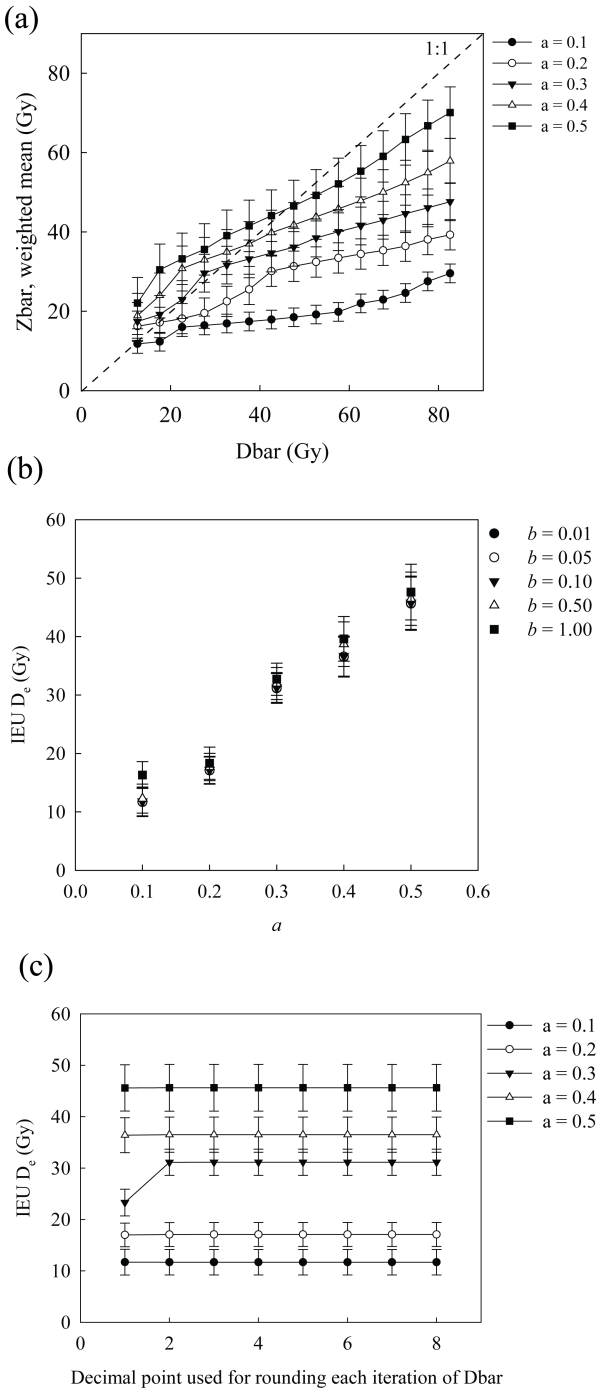

Figure 2. Results from applying the IEU model and changing different parameters for the example datasets: (a) fixed iteration of *Dbar* using a range of *a* values; (b) IEU D_e values calculated when varying both the *a* and *b* values; (c) IEU D_e values determined when the values of *Dbar* and *Z* are calculated to different decimal points for comparison using different *a* values.

sensitivity of the IEU D_e value to changing values of *a* can be different for D_e distributions determined from different samples (Medialdea et al., 2014; Sim et al., 2014). The example dataset (Fig. 1a) is used in this study to test how sensitive the IEU model is to varying the values of *a* and *b*, and the number of decimal points that the values of *Dbar* and *Z* are calculated to for comparison. The results from performing fixed iterations of *Dbar* when changing the *a* value from 0.1 to 0.5 are shown in Fig. 2a, and suggest that the fixed iteration of *Dbar* using an *a* value of 0.3 is the only dataset that has multiple solutions for *Dbar* = *Zbar*. Fig. 2a plots the corresponding IEU D_e values calculated when automating the iteration of *Dbar* using *a* values from 0.1 to 0.5, in addition to simultaneously varying the value of *b* from 0.01 to 1.00. These sensitivity experiments demonstrate that the IEU D_e value for this sample is highly sensitive to changes in the value of *a* value but less sensitive to changes in the value of *b*. This is because the value of *b* only becomes important for the calculations when the D_e distributions contain several low D_e values, which is not the case for the sample shown in Fig. 2. The differences in the IEU D_e values in Fig. 2 emphasise the need to accurately quantify the amount of scatter in a naturally well-bleached D_e distribution for this material, which is also an important requirement when applying the MAM.

The number of decimal points that the values of *Dbar* and *Z* are calculated to for comparison is also varied for the example dataset to assess whether this influenced the calculation of the IEU D_e value (Fig. 2c). The results from varying the number of decimal points from one to eight show how it did not affect the IEU D_e value for the majority of cases. However, the IEU D_e value calculated using an *a* value of 0.3 was lower when *Dbar* and *Z* were calculated to one decimal point (23.3 Gy $\pm$ 2.6 Gy), in comparison to when it was calculated to two decimal points (31.13 Gy $\pm$ 2.54 Gy). Although this is a very minor part of the calculations of the IEU model, Fig. 2c shows that it can have a large impact upon the D_e value determined. As a result, the *calc_IEU* function is designed to consistently calculate *Dbar* and *Z* to two decimal points for comparison to ensure that all results are reproducible.

5. Conclusions

A new function (*calc_IEU*) is now available in the R 'Luminescence' package and can be used to calculate burial dose estimates for a given D_e distribution. The IEU model can be used to determine D_e values for luminescence dating of partially-bleached samples by calculating the weighted mean from the grains of a partially-bleached population that were well bleached upon deposition (Thomsen et al., 2007). The *calc_IEU* function is easy to use and rapidly automates the calculations. In addition to calculating the IEU D_e value, the function uses fixed values of *Dbar* across a range of the D_e distribution to assess whether there is more than one solution for the model using the specified parameters. The efficiency of the *calc_IEU* function in calculating the IEU D_e value for a dataset means that sensitivity tests of the model to changing input parameters can be rapidly assessed. The sensitivity of the IEU D_e value to varying the amount of uncertainty arising from the scatter in a naturally well-bleached D_e distribution (i.e. the *a* value) has been investigated for the ex-

ample dataset in this study. The results demonstrate that the IEU D_e value for these data is highly sensitive to the value of a used. Performing sensitivity tests of the IEU D_e value to parameters (e.g. a) can be particularly useful for luminescence dating of samples that are potentially complicated by additional sources of extrinsic uncertainty that are difficult to quantify (e.g. microdosimetry or bioturbation).

Acknowledgments

The author is grateful to K. Thomsen for checking the calculations performed in the *calc_IEU* function and for her insightful comments when reviewing this manuscript. C. Burow and S. Kreutzer are acknowledged for their contributions in integrating the function into the R 'Luminescence' package. Thanks also to G. Duller for the problem solving discussions during the writing of parts of this function and to G. King and A. Stone for feedback on initial drafts of this manuscript. This paper was written while the author was supported by a Natural Environment Research Council consortium grant (BRITICE-CHRONO NE/J008672/1)), and the sample used as an example in this study (T4CEIF01) forms part of the BRITICE-CHRONO project.

References

Galbraith, R.F., Roberts, R.G., Laslett, G.M., Yoshida, H., and Olley, J.M. *Optical dating of single and multiple grains of quartz from Jinmium rock shelter, northern Austrailia: part I, experimental design and statistical models*. Archaeometry, 41: 339–364, 1999.

Kreutzer, S., Schmidt, C., Fuchs, M., Dietze, M., Fischer, M., and Fuchs, M. *Introducing an R package for luminescence dating analysis*. Ancient TL, 30: 1–8, 2012.

Medialdea, A., Thomsen, K.J., Murray, A.S., and Benito, G. *Reliability of equivalent-dose determination and age models in the OSL dating of historical and modern palaeoflood sediments*. Quaternary Geochronology, 22: 11–24, 2014.

Reimann, T., Thomsen, K.J., Jain, M., Murray, A.S., and Frechen, M. *Single-grain dating of young sediment using the pIRIR signal from feldspar*. Quaternary Geochronology, 11: 28–41, 2012.

Sim, A.K., Thomsen, K.J., Murray, A.S., Jacobsen, G., Drysdale, R., and Erskine, W. *Dating recent floodplain sediments in the Hawkesbury-Nepean River system, eastern Australia using single-grain quartz OSL*. Boreas, 43: 1–21, 2014.

Thomsen, K.J., Jain, M., Bøtter-Jensen, L., Murray, A.S., and Jungner, H. *Variation with depth of dose distributions in single grains of quartz extracted from an irradiated concrete block*. Radiation Measurements, 37: 315–321, 2003.

Thomsen, K.J., Murray, A.S., Bøtter-Jensen, L., and Kinahan, J. *Determination of burial dose in incompletely bleached fluvial samples using single grains of quartz*. Radiation Measurements, 42: 370–379, 2007.

Topping, J. *Errors of Observation and their treatment*. The Institute of Physics and The Physical Society, London, 1955. pp. 91 93.

Reviewer

Kristina Thomsen

Ancient TL

Re-examination of common extraction and purification methods of quartz and feldspar for luminescence dating

N. Porat,[1*] G. Faerstein,[1] A. Medialdea,[2,3] A.S. Murray[3]

[1]Geological Survey of Israel, 30 Malkhe Israel St., Jerusalem, Israel
[2]Department of Geography - University of Sheffield, Sheffield, England
[3]Nordic Laboratory for Luminescence Dating, Department of Geoscience, Aarhus University, Risø Campus, Roskilde, Denmark

*Corresponding Author: naomi.porat@gsi.gov.il

Received: December 4, 2014; in final form: May 31, 2015

Abstract

We tested common mineral extraction and purification procedures used in luminescence dating. Coarse grain quartz and alkali feldspar (KF) were extracted and etched from three samples of different geological setting and mineralogical maturity, using a variety of laboratory procedures. This was followed by particle size distribution measurement, SEM/EDS and XRF analyses, and D_e determinations employing SAR protocols – all used to characterize the mineral extracts.

Etching quartz in 40 % HF for 40 min removed all feldspars, with some preferential etching along fissures and grain boundaries. For mineralogically less mature samples, HF reduced average quartz grain size by 30–50 μm, whereas in mature samples extended etching of up to 60 min reduces grain size by ~10 μm. Ca-fluorides precipitated during HF etching but were fully removed by soaking overnight in 16 % HCl. Extracting quartz by heavy liquids or by magnetic separation (both followed by HF etching) resulted in equally pure quartz, with statistically identical D_e values.

Soaking KF for 40 min in 10 % HF resulted in uneven etching, severe micro-scale erosion along cleavage plains, grain disintegration, substantial precipitation of K-fluorides and the reduction of more than 100 μm in modal grain size, probably due to grain breakage along etched plains. The effects of etching vary greatly between samples from different geological provinces; more mature samples are etched in a more uniform way whereas mineralogically less mature samples are fragmented by etching.

The best benefits for KF are obtained by etching in diluted HF for short duration. For quartz, more concentrated HF and longer etching might be considered if grains are to have their entire α-affected zone (20 μm) removed. Since concentrated HF dissolves all feldspar contamination in quartz, there is no need for re-sieving after HF as that would bias the original grain size. Our results provide confidence in standard laboratory quartz sample preparation.

Keywords: Luminescence, HF-etching, K-feldspar, Sample preparation

1. Introduction

Extracting coarse (fine-sand size) quartz or alkali feldspars from sandy sediments for luminescence dating usually follows routine and established laboratory protocols (e.g. Wintle, 1997). This involves sieving, dissolving carbonates and oxidizing organic material, and concentrating quartz or feldspars using heavy liquids (density separation, Aitken, 1998, p. 67) or magnetic separation (Porat, 2006). To remove the α-affected zone of quartz grains, these are etched in concentrated hydrofluoric acid (HF) followed by soaking in hydrochloric acid (HCl) to dissolve fluorides. It was estimated that 40 min etching in 40–48 % HF would remove 10 μm from the outer zone of the grains – the area affected by α particles (Aitken, 1985, p. 255–258); this estimate was

based on weight loss during etching, since devices that measure particle size by laser diffraction were not available at the time.

The revival of alkali feldspar (KF) dating using the post IR-IR at elevated temperatures (Thomsen et al., 2008; Buylaert et al., 2009; Li & Li, 2011), brings again to attention issues concerning dose rate evaluations, namely the a-value and internal K-content of the extracted KF; knowing these correctly is crucial for obtaining accurate and precise ages. For a-values, a very large range can be found in the literature, from 0.2 for coarse grains (Rendell et al., 1993) to 0.07 for fine grains (Kreutzer et al., 2014). Removing the α-affected zone by etching would be most beneficial as knowing the a-value would no longer be necessary. Currently, laboratories vary in their practice, from not applying any etching at all (e.g., Porat et al., 2004; Trauerstein et al., 2014), to extended immersion in diluted HF (e.g., Li & Li, 2011; Buylaert et al., 2013). However previous studies showed that etching does not remove a uniform layer around feldspar grains but rather the acid penetrates along cleavage planes (Duller, 1992, p. 16). K-content in KF is either measured (Porat et al., 2004) or assigned a fixed value, usually 12.5 % (Huntley & Baril, 1997). As we will show, etching with HF might have bearings also on the K-contents of the KF.

Extraction procedures are often described briefly, even in the more applied, hand-on reviews and books (e.g., Wintle 1997, Aitken 1998, p. 66–67), and many of these protocols may have not been tested in years, if ever. This study brings together the results of a series of experiments that test various steps in conventional preparation protocols used to extract quartz and KF. The topics investigated were:

1. Is magnetic separation as effective as the 2-step density separation for producing pure quartz extracts?
2. Does conventional HF etching (40–48 % HF for 40 min) remove the 10 μm zone affected by α-particles?
3. How common are precipitated fluorides and do we need the ensuing step of dissolving them in HCl?
4. What are the effects of etching with diluted HF on feldspars?
   (a) By how much is grain size reduced?
   (b) Does etching uniformly remove the α-affected zone?
   (c) Does the D_e change with etching?

One important property of clastic sediments commonly dated by luminescence methods is their maturity, which is reflected among other things in the presence of rock fragments and the quantity and type of feldspars and heavy minerals. Sediments mature physically by repeated deposition/resuspension and long distance transport of the sediment grains from their source; this results in a reduction in grain size and the preferential breakdown and removal of unstable minerals and rock fragments (Blatt & Tracy, 2005). For quartz it entails the disintegration of grains rich in other mineral inclusions and air bubbles, leaving behind the more resistant grains. For feldspars the removal of the mineralogically less stable grains (e.g., plagioclase) and altered (cericitised) grains results in a K-rich and resilient feldspar fraction. This process appears to increase some desirable luminescence properties of quartz, such as brightness and sensitivity (Pietsch et al., 2008). In this study we tested sediments of high and low level of maturity, to see how each responds to conventional laboratory procedures.

2. Samples and laboratory methods

Coarse grain quartz and KF were extracted from three samples from the collection of the Geological Survey of Israel luminescence dating laboratory, of different geological setting and mineralogical maturity:

- RAM-8: mature, fine sandy, quartz-rich sediment derived from reworked dunes in the western Negev, Israel, with the sand originating from the Nile (Ben-David, 2003). K-rich feldspars were concentrated from this sample.
- FGA-26: coarse desert loess from the Negev Mts. (Faerstein, 2003), for which the source of the quartz is distant dunes (Enzel et al., 2010) with mature mineralogy (Muhs et al., 2013). Quartz was extracted from this sample.
- 23-5: Fluvial sand from Nahal Avrona, southern Negev (Amit et al., 2002), derived from a nearby igneous terrain, containing abundant rock fragments and heavy minerals. Both quartz and K-rich samples were separated from this mineralogically less mature sample.

After sieving each sample to the desired grain size and dissolving carbonates with 8 % HCl, the ensuing treatments varied. The different treatments and analyses performed on each sample are listed in Table 1 and the captions therein.

Scanning Electron Microscope (SEM) imaging was used to observe the effects of etching on the surface morphology of quartz and KF grains. Energy Dispersive Spectrometer (EDS) was used to check the purity of the quartz extracts by mapping K and Na contents, and to identify fluorides and analyze their composition in HF-etched quartz and KF. Grain size analysis before and after HF-etching, measured using a laser Malvern Mastersizer, was used to check the reduction in grains size due to etching. An XRF module attached to a Riso reader was used to measure the relative K-contents (of the sum K+Na+Ca) in the different separated and etched KF fraction (Kook, 2012). D_e was measured on large (8 mm) multi-grain aliquots using the SAR protocol for quartz (Murray & Wintle, 2000) and the post IR-IR$_{290}$ SAR for KF (Thiel et al., 2011).

Preparation						Analyses			
Sample	Grain size (μm)	Density separation		Magnetic separation	HF [Strength (%) / duration (min)]	HCl 16%	D_e	SEM	XRF	Grain size
		2.62 (g/cm^3)	2.58 (g/cm^3)							
Alkali Feldspar										
RAM-8	149–177	x	x		0		x	x	x	
		x	x		10/10		x	x	x	
		x	x		10/20		x		x	
		x	x		10/40		x	x	x	
23-5	125–177	x	x		0		x	x	x	x
		x	x		10/10		x	x	x	
		x	x		10/20		x		x	x
		x	x		10/40		x	x	x	
Quartz										
23-5	125–177	x			0			x		x
		x			40/40			x		
		x			40/40	x	x	x		x
23-5	177–212			x	0			x		x
				x	40/40			x		
				x	40/40	x	x	x		x
FGA-26	74–125			x	0			x		x
				x	40/40			x		
				x	40/40	x	x	x		x
				x	40/60					x

Table 1. Samples used and analyses carried out in this study. The samples were sieved to the required grain size, soaked in 10 % HCl overnight to dissolve carbonates, rinsed and dried. This was followed by either density separation (Sodium-Polytungstate with density of 2.62 g/cm^3) or magnetic separation (Frantz LB-1, 1.4 A on the magnet). HF etching was carried out for the durations and concentrations listed, which for some samples was followed by rinsing in 16 % HCl overnight. All preparations and analyses were performed at the laboratories of the Geological Survey of Israel, except for XRF that was measured in Risø-DTU using a modified Risø Reader with an XRF attachment (Kook, 2012). Grains size was measured with Malvern Mastersizer laser particle size analyzer.

3. Results

SEM/EDS mapping showed that before HF-etching, all quartz samples contained small amounts of feldspars (3–10 %), indicating that neither density separation nor magnetic separation can fully remove all feldspars, and that HF etching is essential. SEM/EDS mapping also showed that the alkali feldspar extracts contained some quartz grains (∼5 %). Roughly15 % Na-rich grains were observed within the predominantly K-rich feldspars of sample 23-5.

3.1. Comparison of extraction procedures for quartz

For sample 23-5, SEM images followed by EDS mapping of Si and K, showed that the two size fractions (125–177 μm and 177–212 μm), each extracted by a different procedure (and followed by HF-etching), contained pure quartz, with no contaminating KF (Fig. 1). The measured D_e values (on 24 aliquots for each size fraction) were statistically identical, 10.8 $\pm$ 1.0 Gy and 9.7 $\pm$ 1.6 Gy for the 125–155 μm and 177–212 μm, respectively.

3.2. Reduction in grain size

Grain size reduction of quartz due to etching in 40 % HF for 40 min varies among samples (Fig. 2). The mineralogically mature sample FGA-26 was etched by ∼10 μm; increasing etching time to 60 min did not reduce grains size any further. As the shape of the particle size distribution did not change much by etching, only the peak shifted by 10 μm (Fig. 2a), we can deduce that reduction in grain size was fairly uniform. In the two grain size fractions of the less mature sample 23-5 (125–177 μm and 177–212 μm), 40 min etching reduced the modal grain size by 33 μm and 48 μm, respectively. Etching also resulted in broadening of the particle size distribution and an increased tail of smaller particles

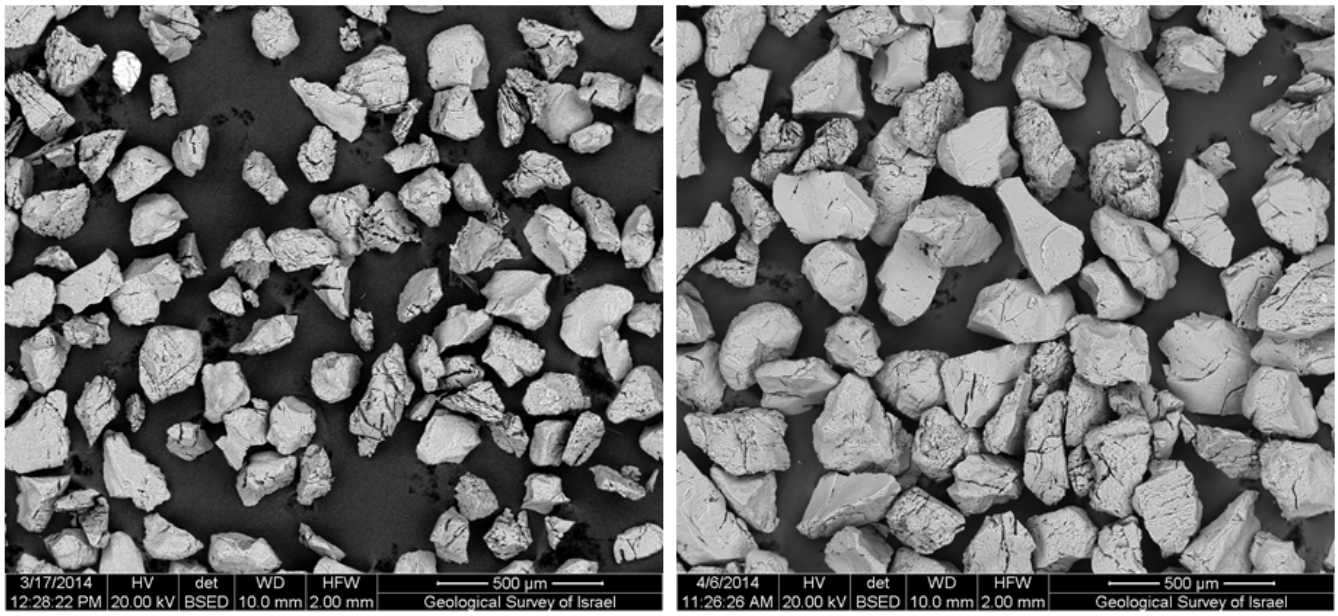

Figure 1. SEM images of two size-fractions of quartz sample 23-5, purified by different procedures. a. 125–177 μm, extracted using 2-step density separation (2.62 g/cm^3 and 2.58 g/cm^3), followed by HF etching and rinsing with HCl; D_e = 10.8 $\pm$ 1.0 Gy. b. 177–212 μm, extracted using magnetic separation, followed by HF etching and rinsing with HCl; D_e = 9.7 $\pm$ 1.6 Gy. Average D_e values are statistically identical, however the coarser grain size has higher scatter on the average D_e.

(Fig. 2b).

Etching KF sample 23-5 (125–212 μm) in 10 % HF for 20 min and 40 min resulted in grain fragmentation (Fig. 3c), and the modal grain size was reduced by 50 μm and 100 μm, respectively (Fig. 2c). Particle size distribution after etching is substantially shifted towards the smaller grains when compared to the original distribution, indicating that most grains had their size reduced, though perhaps not uniformly.

3.3. Removal of feldspars in quartz by HF

Soaking quartz in 40 % HF for 40 min was very efficient in removing all feldspars, regardless how much was previously present. SEM images and EDS mapping show no remaining KF (Fig. 1).

3.4. Fluoride precipitation and removal

In both mineral extracts, HF etching resulted in fluoride precipitation, observed using the SEM/EDS. These are shown in Fig. 3; the chemical composition of the precipitates is given in Table 2; and their EDS spectra are shown on Fig. 4. In the quartz extracts, poorly crystalline Ca-fluorides precipitated (Fig. 3e & 4c). Subsequent soaking of the HF-etched quartz samples in 16 % HCl overnight completely removed all Ca-fluorides (Figs. 1 & 3f).

In KF sample 23-5, well crystallized, idiomorphic K-fluoride crystals formed after 40 min etching in 10 % HF (Figs. 3c & 4b). In sample RAM-8 fluorides appeared as powdery coating of the KF grains (Fig. 3d). Subsequent soaking in HCl was not checked for the removal of K-fluorides precipitated in the KF samples.

(a)			
Element	**Weight %**	**Atomic %**	**Number of ions**
F	61.49	66.65	6.24
Na	0.61	0.55	0.05
Al	8.69	6.63	0.62
Si	1.62	1.19	0.11
Ca	11.68	6.00	0.56
Ba	1.31	0.20	0.02
O	14.60	18.79	1.76
Totals	100.00		
(b)			
Element	**Weight %**	**Atomic %**	**Number of ions**
F	29.82	38.06	4.62
Si	8.26	7.13	0.87
K	43.60	27.04	3.29
O	18.33	27.78	3.38
Totals	100.00		

Table 2. SEM/EDS analyses of selected precipitated fluoride crystals. (a) Ca-fluorides in HF-etched quartz sample FGA-26 (Fig. 4e); (b). K-fluorides in HF-etched KF sample 23-5 (Fig. 4c).

3.5. Uniformity of etching

SEM images show the manner in which HF dissolved the quartz and KF grain surfaces. In quartz, the mature sample

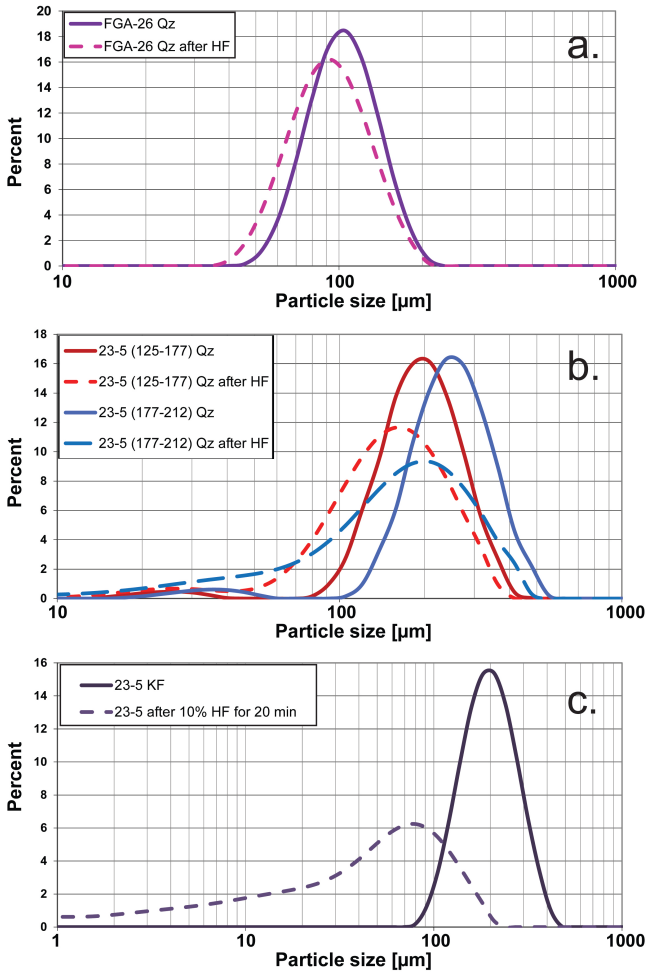

Figure 2. Grain size analyses (average of 3 measurements) before (solid line) and after (dashed line) etching. Quartz (a. and b.) was etched with 40 % HF for 40 min. a. 88–125 μm quartz extract, sample FGA-26. Etching reduced the modal grain size by 10 μm. b. 125–177 μm (red) and 177-212 μm (blue) quartz extracts, sample 23-5. Modal grain size was reduced by 33 μm and 48 μm, respectively. Note broadening of particle size distribution and increase in the proportions of smaller particles after etching. c. 125–212 μm KF extract, etched with 10 % HF for 20 min. Etching resulted in grain fragmentation and the modal grain size was reduced by 50 μm.

FGF-26 was etched in a more even manner when compared to the less mature sample 23-5 (compare Figs. 3e and 1b). In the latter, some quartz grains were etched preferentially along fissures and grain boundaries (Fig. 1), possibly because these grains contain mineral inclusions and air bubbles which are more susceptible to etching.

For the KF, etching was preferential along cleavage plains, becoming more severe with longer etching time. Ten min etching of the mature sample (RAM-8) had only a minor effect on the morphology of the grains, whereas that same duration of etching severely affected sample 23-5. Forty min etching of the latter resulted in severe grain fragmentation (Fig. 3c).

3.6. Effects of etching on the D_e values of KF

Removing the outer zone of grains should reduce their measured D_e values as the area dosed by α-particles is removed. For both KF samples (23-5 and RAM-8) the D_e values, measured using the post IR-IR$_{290}$, were reduced as a function of etching time (Figs. 5a & 5b) and after 40 min they were 10–15 % lower than that of the unetched samples. The reduction expected due to removal of 20 μm was calculated from the dose rates for the individual samples, and is shown on Fig. 5 as a horizontal bar. For sample 23-5, 10 min etching was sufficient to reduce the D_e value as expected; further etching has only a minor affect. However the D_e value for sample RAM-8 continues to decrease with longer etching time, to values well below those expected from the removal of the α-affected zone. This could be explained by the removal of a weathering rind or a thin clay mineral coating, not identified by the SEM or XRF.

3.7. Effects of etching on K-contents in KF

K-content was measured for the original, unetched KF extracts using inductively coupled plasma spectroscopy (ICP-AES), and the relative K-contents (as a fraction of the total K+Na+Ca) were measured for the original and etched fractions using XRF. For sample 23-5, etching increased relative K contents in the KF fraction by ~30 %, from 0.70 to 0.93 (a value of unity signifies pure orthoclase with 14 % K) and lowered the Na contents (Fig. 5c), which can be explained by preferential dissolution by HF of the Na-feldspar remaining in the sample after density separation. The increase in the K-contents by ~30 % (from the original value of 7.2 % as measured by ICP-AES) brings this value closer to the "ideal" 12.5 % commonly used for internal dose rate calculations (Huntley & Baril, 1997). On the other hand, for sample RAM-8, with original K-contents of 11.5 %, 40 min etching somewhat lowered the relative K-contents from 0.94 to 0.88, which can be explained by the removal of K-rich clay coating (also deduced from the reduction in D_e by etching).

4. Summary and Recommendations

In this study we found that routine HF etching of quartz (40 % HF, 40 min, ~5cc HF for each gram of quartz) removed 10 μm from geologically mature samples; increasing etching time to 60 min did not reduce grain size any further. The modal grain size of mineralogically less mature quartz samples was reduced with etching by 30–50 μm, possibly due to fragility of quartz grains. Although small, the α-dose rate remaining after the removal of 10 μm is not zero and it should be taken into account when calculating ages for some quartz samples, particularly those with low dose rates.

Ca-fluorides precipitated during HF etching in all quartz samples but were fully removed by soaking overnight in 16 % HCl. More experiments are needed to see if higher concentration of HCl coupled with shorted immersion time can achieve the same result. Also the effect of these precipitated fluorides on the luminescence signal and the measured

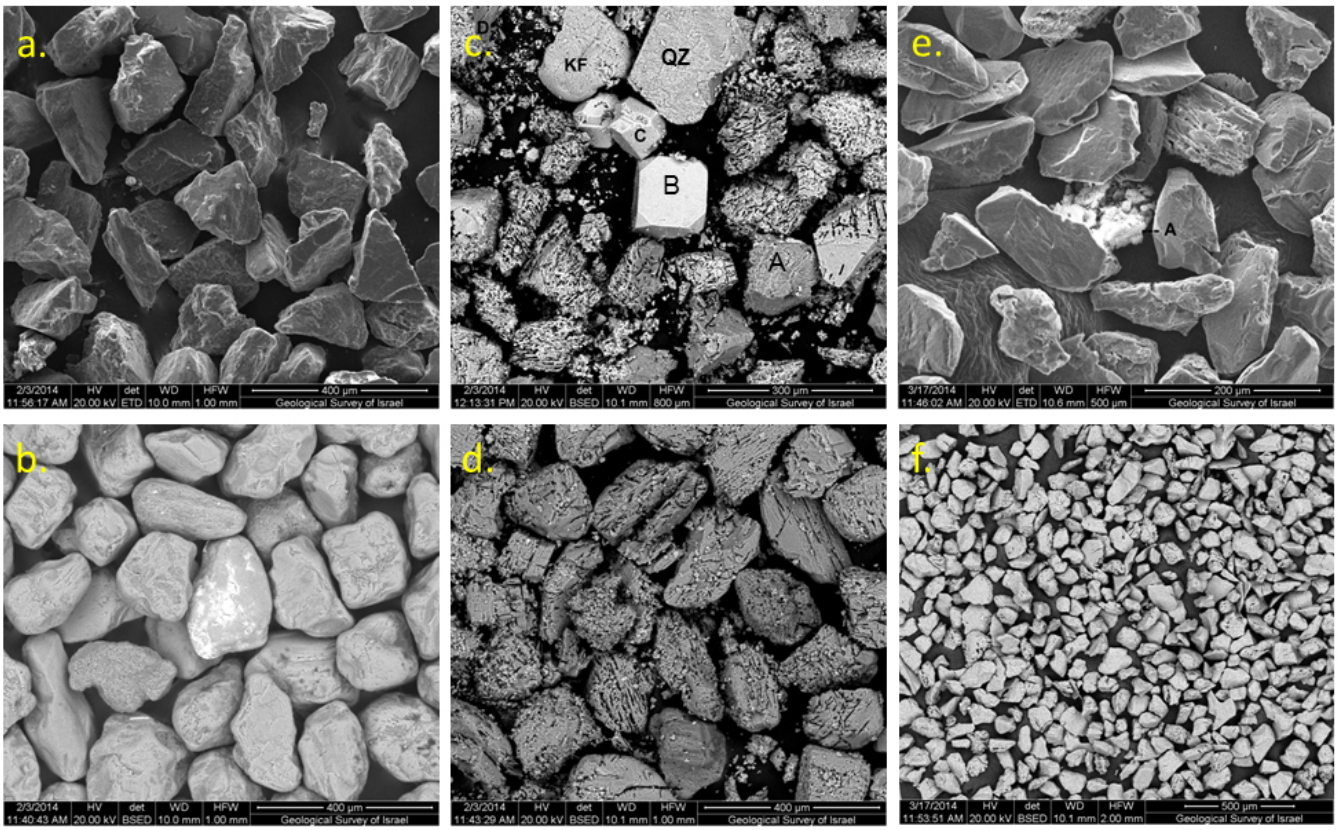

Figure 3. SEM/EDS images showing the effects of HF etching on KF and quartz. Unetched KF, 23-5 (a) and RAM-8 (b). Note angular and sharp grains in the less mature sample 23-5 against rounded and smooth grains in the mature RAM-8 samples. The same samples after 40 min etching in 10 % HF are shown on c. (23-5) and d. (RAM-8). For 23-5 (c), note highly pitted and disintegrated KF grains, isolated unaffected quartz (marked QZ) and KF (marked KF) grains, and newly precipitated idiomorphic, cubic fluoride crystals (marked A, B, C). Representative EDS spectra of the KF grain and crystal B are given in Fig. 5. Chemical composition of grain B is given in Table 2b. For RAM-8 (d), the grains are intact but are deeply etched along cleavage plains. The fluorides appear as fine crystals on the KF grain surfaces. e. and f. Quartz sample FGA-26 after HF etching, before (e) and after (f) rinsing overnight in 16 % HCl. In e. fluorides appear as white powder in the center. Representative EDS spectra and analyses are given in Fig. 5c. and Table 2a. After etching and soaking in HCl (f) no fluorides were observed.

D_e values need testing.

Etching KF, even with diluted (10 %) HF, affected the mineral grains in a complex manner. It resulted in uneven reduction in grains size so that the α-affected zone might not be removed in a fully uniform manner. Extended etching also created severe micro-scale corrosion along cleavage plains, grain disintegration and substantial precipitation of K-fluorides. The reduction of 100 μm in the modal grains size after 40 min etching is probably due to grain breakage along etched plains.

Nonetheless, particle size distribution show that the modal grain size is substantially reduces (50 μm after 20 min), suggesting that even though some grains are etched more than others, we can assume that for most grains at least 10 μm were removed. Additionally, etching cleans unwanted coatings from the grains and lowers D_e values sufficiently to assume that the α-affected zone is removed; and in cases it increased average K contents, probably by preferentially dissolving Na-feldspars. Thus, mild etching of KF is beneficial in several aspects.

Overall, the results presented here provide confidence in standard laboratory sample preparation procedures. More samples from other geological provinces should be tested in the manner presented here to fully confirm the presented observations.

Here are suggested modifications of the standard procedures for optimal quartz and KF purification:

- More concentrated HF might be considered if grains are to have their entire α-affected area (20 μm) removed. Otherwise one should not assume that the entire zone was etched.
- Soaking the HF-etched quartz grains in HCl (in this study it was overnight in 16 % HCl) is necessary to remove all fluorides and avoid the risk of these contributing to the luminescence signal of quartz.
- Since HF removes all feldspars in quartz-rich samples, there is no need to re-sieve the samples after HF, as that would bias the original grain size and the values

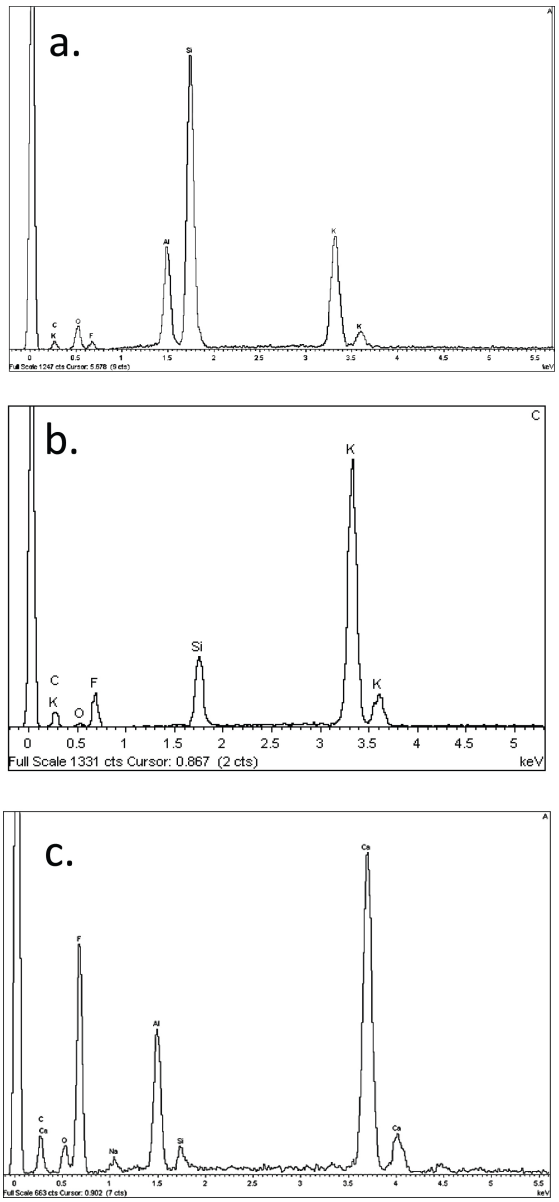

Figure 4. SEM/EDS composition spectra of selected mineral grains. a. Typical K-feldspar, sample 23-5. b. K-fluoride precipitate (see also Table 2b), sample 23-5. c. Ca-fluoride precipitate (see also Table 2a), sample FGA-26.

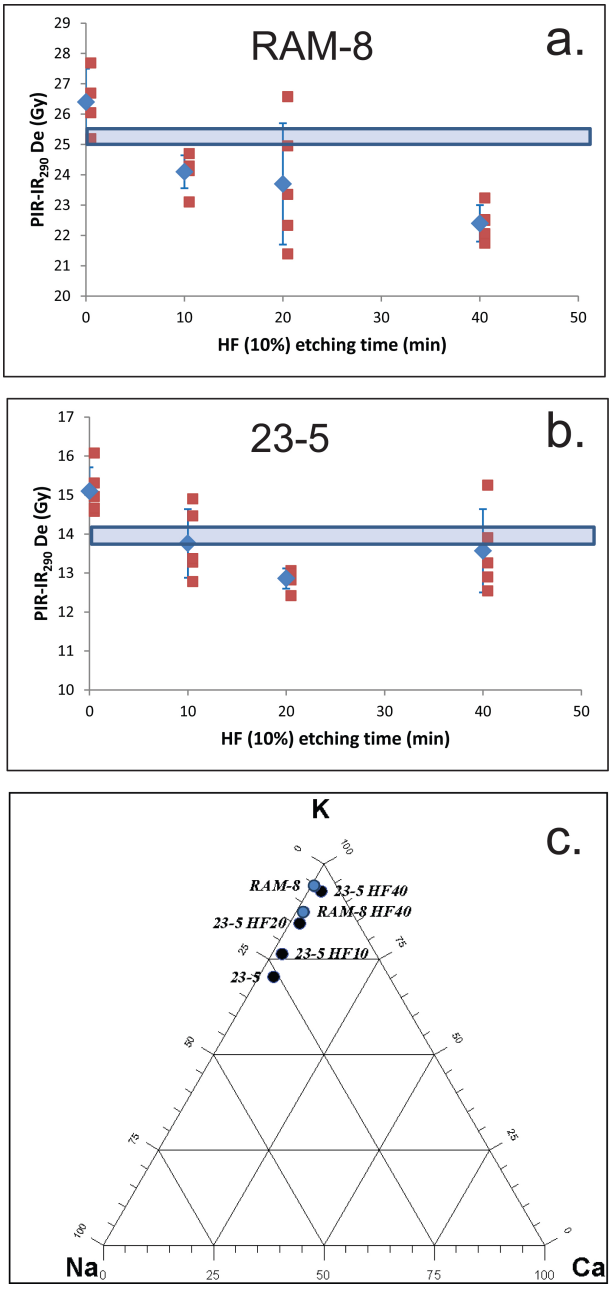

Figure 5. D_e values and chemical composition measured on KF extracted from two samples (using 2-step density separation), etched with 10 % HF for varying durations. a. & b. D_e values as a function of etching time for KF extracts of RAM-8 & 23-5, respectively. The horizontal bar shows the D_e expected after removing the 20 μm zone affected by α-particles, calculated from the original D_e (0 time etching), the sediment dose rate, 12.5 $\pm$ 0.5 % K in the KF and an a-value of 0.1 $\pm$ 0.05. Note that for sample RAM-8 (a) the reduction in D_e is greater than that explained by etching 20 μm. c. Ternary diagram of XRF measurements of KF extracts showing changes in relative K, Na and Ca contents (representing the feldspar minerals Orthoclase, Albite and Anorthite, respectively). For sample 23-5 (dark blue circles) etching substantially increased the concentration of K while reducing Na contents. For sample RAM-8 (light blue circles) 40 min etching somewhat reduced K contents.

used for calculating beta attenuation. But if sieving is done, a sieve size smaller by at least one mesh than the lower grain size should be used, so that only fragmented grains are removed.

- Caution should be used when etching KF; it is recommended to use diluted (no more than 10 %) HF for a short duration (10–15 min). This short duration will minimize K-fluoride precipitation and will most likely remove most of the α-affected zone. Longer etching might compromise some of the KF properties.

- An added step of soaking the HF-etched KF in 16 % HCl overnight to remove fluorides is advisable.

Acknowledgments

We thank M.H. Kook (Center for Nuclear technologies, Risø, DTU) for helping with the XRF measurements, Raanan Bodzin (Geological Survey of Israel) for helping with the SEM analyses, and Hadar Elyashive (Geological Survey of Israel) for particle size analyses.

References

Aitken, M.J. *Thermoluminescence dating*. Studies in archaeological science. Academic Press, 1985.

Aitken, M.J. *An Introduction to Optical Dating*. Oxford University Press, 1998.

Amit, R., Zilberman, E., Enzel, Y., and Porat, N. *Paleoseismic evidence for time dependency of seismic response on a fault system in the southern Arava Valley, Dead Sea rift, Israel*. Geological Society of America Bulletin, 114(2): 192–206, 2002. doi: 10.1130/0016-7606(2002)114⟨0192:PEFTDO⟩2.0.CO;2.

Ben-David, R. *Changes in desert margin environments during the climate changes of the Upper Quaternary*. PhD thesis, Hebrew University in Jerusalem, 2003. (in Hebrew, English abstract).

Blatt, H. and Tracy, R. *Petrology: Igneous, Sedimentary, and Metamorphic*. W. H. Freeman, 2005.

Buylaert, J.P., Murray, A.S., Thomsen, K.J., and Jain, M. *Testing the potential of an elevated temperature IRSL signal from K-feldspar*. Radiation Measurements, 44(5-6): 560–565, 2009. doi: 10.1016/j.radmeas.2009.02.007.

Buylaert, J.P., Murray, A.S., Gebhardt, A.C., Sohbati, R., Ohlendorf, C., Thiel, C., Wastegård, S., and Zolitschka, B. *Luminescence dating of the PASADO core 5022-1D from Laguna Potrok Aike (Argentina) using IRSL signals from feldspar*. Quaternary Science Reviews, 71: 70–80, 2013. doi: 10.1016/j.quascirev.2013.03.018.

Duller, G.A.T. *Luminescence Chronology of Raised Marine Terraces, South-West North Island, New Zealand*. PhD thesis, Institute of Earth Studies, University of Wales, Aberystwyth, 1992.

Enzel, Y., Amit, R., Crouvi, O., and Porat, N. *Abrasion-derived sediments under intensified winds at the latest Pleistocene leading edge of the advancing Sinai–Negev erg*. Quaternary Research, 74(1): 121–131, 2010. doi: 10.1016/j.yqres.2010.04.002.

Faerstein, G. *Improving OSL dating of fluvial sediments – application to the transition from aggradation to incision during the last glacial maximum in southern Israel*. Master's thesis, Hebrew University in Jerusalem, 2003. (in Hebrew, English abstract).

Huntley, D.J. and Baril, M.R. *The K content of the K-feldspars being measured in optical dating or in the thermoluminescence dating*. Ancient TL, 15(1): 11–13, 1997.

Kook, M.H., Lapp T. Murray A.S. Thiel C. *A RisøXRF attachment for major element analysis of aliquots of quartz and feldspar separates*, 2012. UK Luminescence and ESR Meeting, Aberystwyth, September 2012 (abstract), p. 37.

Kreutzer, S., Schmidt, C., DeWitt, R., and Fuchs, M. *The a-value of polymineral fine grain samples measured with the post-IR IRSL protocol*. Radiation Measurements, 69: 18–29, 2014. doi: 10.1016/j.radmeas.2014.04.027.

Li, B. and Li, S.-H. *Luminescence dating of K-feldspar from sediments: A protocol without anomalous fading correction*. Quaternary Geochronology, 6(5): 468–479, 2011. doi: 10.1016/j.quageo.2011.05.001.

Muhs, D.R., Roskin, J., Tsoar, H., Skipp, G., Budahn, J.R., Sneh, A., Porat, N., Stanley, J.-D., Katra, I., and Blumberg, D.G. *Origin of the Sinai–Negev erg, Egypt and Israel: mineralogical and geochemical evidence for the importance of the Nile and sea level history*. Quaternary Science Reviews, 69: 28–48, 2013. doi: 10.1016/j.quascirev.2013.02.022.

Murray, A.S. and Wintle, A.G. *Luminescence dating of quartz using an improved single-aliquot regenerative-dose protocol*. Radiation Measurements, 32(1): 57–73, 2000. doi: 10.1016/S1350-4487(99)00253-X.

Pietsch, T.J., Olley, J.M., and Nanson, G.C. *Fluvial transport as a natural luminescence sensitiser of quartz*. Quaternary Geochronology, 3(4): 365–376, 2008. doi: 10.1016/j.quageo.2007.12.005.

Porat, N. *Use of magnetic separation for purifying quartz for luminescence dating*. Ancient TL, 24(2): 33–36, 2006.

Porat, N., Wintle, A.G., and Ritte, M. *Mode and timing of kurkar and hamra formation, central coastal plain, Israel*. Israel Journal of Earth Sciences, 53(1): 13–25, 2004. doi: 10.1560/07KK-KGLU-0A9F-DE9C.

Rendell, H.M., Yair, A., and Tsoar, H. *Thermoluminescence dating of periods of sand movement and linear dune formation in the northern Negev, Israel*. Geological Society, London, Special Publications, 72(1): 69–74, 1993. doi: 10.1144/GSL.SP.1993.072.01.08.

Thiel, C., Buylaert, J.P., Murray, A.S., Terhorst, B., Hofer, I., Tsukamoto, S., and Frechen, M. *Luminescence dating of the Stratzing loess profile (Austria) - Testing the potential of an elevated temperature post-IR IRSL protocol*. Quaternary International, 234(1-2): 23–31, 2011. doi: 10.1016/j.quaint.2010.05.018.

Thomsen, K.J., Murray, A.S., Jain, M., and Bøtter-Jensen, L. *Laboratory fading rates of various luminescence signals from feldspar-rich sediment extracts*. Radiation Measurements, 43(9-10): 1474–1486, 2008.

Trauerstein, M., Lowick, S.E., Preusser, F., and Schlunegger, F. *Small aliquot and single grain IRSL and post-IR IRSL dating of fluvial and alluvial sediments from the Pativilca valley, Peru*. Quaternary Geochronology, 22: 163–174, 2014. doi: 10.1016/j.quageo.2013.12.004.

Wintle, A.G. *Luminescence dating: Laboratory procedures and protocols*. Radiation Measurements, 27: 769–817, 1997.

Reviewer

Michel Lamothe

Reviewer's Comment

1. This study demonstrates that sediment maturity, a concept developed in sedimentary petrology, has a definite link to mineral solubility in HF and hence, would explain some of the variability seen in the purity of HF-treated quartz extracts. 2. Routine luminescence dating laboratory procedures should include laser diffraction particle size analysis as it allows for more precise assessments of both equivalent dose and dose-rate.

Ancient TL

A note on OSL age estimates in the presence of dose rate heterogeneity

Rex Galbraith,[1*]

[1] Department of Statistical Science, University College London, Gower Street, London, WC1E 6BT, UK

[*]E-mail: r.galbraith@ucl.ac.uk

Received: February 25, 2015; in final form: June 9, 2015

1. Introduction

There has been some discussion on the estimation of OSL ages in the presence of beta dose rate heterogeneity. For example, Jacobs et al. (2008) used an 'adjusted dose rate' method to account for observed equivalent doses that appeared to follow a finite mixture distribution, while Guérin et al. (2013) argued that an estimate based on an average or central age was more appropriate. I recently commented on the latter article to say, among other things, that the mathematical argument presented there did not justify that conclusion and that further statistical analysis was needed (Galbraith, 2015). In this note I will consider dose rate heterogeneity from a statistical point of view.

2. OSL age estimates

An OSL age is usually estimated as a ratio: an equivalent dose divided by a dose rate, each of which is estimated separately. The numerator of that ratio, the equivalent dose, is usually some sort of average or representative value obtained from a sample of mineral grains, that is intended to represent a radiation dose of interest — such as the radiation energy absorbed by the mineral grains in the sample since they were last exposed to sunlight. A variety of methods can be used, depending on the context, to estimate that numerator, including the use of common age, central age, minimum age and finite mixture models. Such models may be expressed either in terms of observed equivalent doses or in terms of their logarithms, depending on whether the dominant sources of variation are additive or multiplicative. Details and rationale of these models can be found in Galbraith & Roberts (2012).

There is a separate industry devoted to estimating the denominator of that ratio, i.e., the relevant 'environmental' dose rate. This is typically a weighted sum of contributions from several sources, including alpha, beta and gamma radiation, and cosmic rays, all of which are estimated or measured separately in the field and in the laboratory, using a variety of emission counting techniques and techniques that directly measure elemental concentrations of U, Th and K. In practice, a single dose rate is usually obtained that represents an 'average' value pertaining to the sample location and its near environment. It is recognised that individual grains in the sample might experience different dose rates, especially from beta sources which can vary across small spatial distances, but dose rates experienced by individual grains are not measured by the current standard techniques. Nevertheless such variation in dose rates will be reflected to some extent in the observed single-grain equivalent doses. What implications might this have for OSL age estimation?

3. A common age model with additive errors

Suppose that we have observed equivalent doses for n mineral grains along with their empirically determined standard errors. Denote these by y_i and s_i, respectively, for $i = 1, 2, \ldots, n$. Let us consider the simplest case where we think that every grain has the same true age t. If the dose rates vary between grains, then the observed equivalent doses will vary partly because of this and partly for other reasons, including natural variation and measurement error. We can express this as

$$y_i = t\xi_i + e_i \qquad (1)$$

where ξ_i is the unobserved dose rate experienced by grain i and e_i is an unobserved random 'error' drawn from a distribution with mean zero and standard deviation σ_i, say. I have used the Greek notation ξ_i, rather than a friendlier symbol such as x_i, to remind us that the individual dose rates are not observed. The error standard deviation σ_i will include variation from all sources other than varying dose rates — including natural variation between grains and measurement error — and will typically be larger than s_i. We should remember too that the assumption that the error distribution has mean 0 is not trivial.

There is little we can do in practice with equation (1),

as ξ_i is not observed or measured. Some further theoretical analysis might be done by making assumptions about the statistical distribution of the dose rates, but before doing so, it is worth noting that if we average both sides of equation (1) we get

$$\bar{y} = t\bar{\xi} + \bar{e} \tag{2}$$

where $\bar{y}$, $\bar{\xi}$ and $\bar{e}$ are the average observed equivalent dose, unobserved dose rate and unobserved error, respectively, for the n grains. A similar equation could be obtained by taking a weighted average: that is, we could regard $\bar{y}$, $\bar{\xi}$ and $\bar{e}$ in (2) as corresponding weighted, rather than unweighted (or straight), averages. In either case, $\bar{e}$ is also a random 'error' drawn from a distribution with mean zero. It follows that if we could estimate $\bar{\xi}$, we could then estimate the age t by dividing $\bar{y}$ by that estimate of $\bar{\xi}$; that is, by dividing an (unweighted or weighted) average equivalent dose by an estimate of the corresponding (unweighted or weighted) average dose rate experienced by the n grains in question.

One problem with the above is that $\bar{\xi}$, the average dose rate for the n grains in our sample, may differ somewhat from the average environmental dose rate that is actually measured, which is an average for a much wider population of grains. In other words, the dose rates for the n sampled grains need to be representative of those for the population for which the average dose rate is actually measured (i.e., the population of all grains in the sample location and its near environment), which might or might not be the case in practice.

Equations (1) and (2) above are analogous to Equations (1) and (2) in Guérin et al. (2013) but are expressed here as a statistical model rather than as relationships between 'true' values. The above argument (with the caveats mentioned) supports their suggestion that, when all grains have the same true age, then this age may be estimated using an average or central age, regardless of how the individual dose rates vary. However, that does not mean that this is the *best* method or even that it is necessarily a good one.

4. Modelling the dose rate distribution

The model equation (1) could be extended to specify a distribution for the single-grain dose rates ξ_i. In practice there is usually very little independent information about what form this distribution might take, other than what can be seen in the observed equivalent doses. Let us consider two simple possibilities.

1. A normal distribution. For example, in the absence of other information, we might assume that ξ_i was drawn from a normal distribution with mean μ_ξ and standard deviation σ_ξ, independently for each grain. Then equation (1) can usefully be expressed as

$$y_i = t\mu_\xi + t(\xi_i - \mu_\xi) + e_i\,. \tag{3}$$

We might regard the measured environmental dose rate as an estimate of μ_ξ, i.e., the mean dose rate for the population from which the grains were sampled. Then the quantity $t(\xi_i - \mu_\xi)$ would be another component of error, from a normal distribution with mean 0 and variance $t^2\sigma_\xi^2$. If e_i was also from a normal distribution, and independent of ξ_i, then the overall error would be from a normal distribution with mean 0 and variance $t^2\sigma_\xi^2 + \sigma_i^2$. In that case, the optimal OSL age estimate would be that obtained from the 'unlogged' version of the central age model.

In other words, making this quite natural assumption about the unobserved single-grain dose rates leads directly to the central age model for optimal estimation of the burial dose and hence the burial age. The dispersion parameter in this central age model will include variation between single grain dose rates, as the above analysis shows.

2. A two component mixture. Another possibility might be to assume that the dose rates come from a two-component mixture distribution where ξ_i takes the value $\mu_{\xi 1}$ with probability p or $\mu_{\xi 2}$ with probability $1-p$, say. Then equation (1) could be written as

$$y_i = t\mu_{\xi 1}u_i + t\mu_{\xi 2}(1-u_i) + e_i \tag{4}$$

where u_i is a bernoulli random variable that takes the value 1 with probability p and 0 with probability $(1-p)$. So the equivalent doses also have a two component mixture distribution with component means $\mu_1 = t\mu_{\xi 1}$ and $\mu_2 = t\mu_{\xi 2}$. The common age t is given by several expressions, including

$$t = \frac{p\mu_1 + (1-p)\mu_2}{p\mu_{\xi 1} + (1-p)\mu_{\xi 2}} = \frac{\mu}{\mu_\xi}\,,$$

where μ and μ_ξ are the mean equivalent dose and mean dose rate, respectively, for the population from which the grains were drawn. So, as usual, the age t can be estimated by dividing an estimate of μ by an estimate of μ_ξ.

One could imagine estimating μ either by fitting a two-component mixture to estimate p, μ_1 and μ_2, and hence $\mu = p\mu_1 + (1-p)\mu_2$, or by simply using an average equivalent dose, ignoring the two-component mixture structure. In the latter case one might consider using either an unweighted average or a weighted average with weights proportional to the reciprocals of the error variances. What are the relative merits of these methods?

In theory, if the data really do come from a two-component mixture distribution, with a well specified error distribution, then it must be optimal to use that model for estimation by maximum likelihood, say. Nevertheless it is useful to consider this in more detail.

Suppose that, as before, e_i has a normal distribution with mean 0 and standard deviation σ_i for grain i. Consider first the hypothetical case that σ_i is the same for all grains ($\sigma_i = \tau$, say) whether or not they are from the same component. Then weighting by $1/\sigma_i^2$ is the same as weighting by $1/\tau^2$, i.e., using a straight (unweighted) average. In that case, it can be shown that this gives exactly the same estimate of μ as that obtained by fitting the two-component mixture.

Now suppose that σ_i is the same for all grains within the same component, but different for grains in different components. That is, $\sigma_i = \tau_1$ if grain i is from component 1 and $\sigma_i = \tau_2$ if grain i is from component 2. Then it can

be shown that using an unweighted average of the equivalent doses will still produce exactly the same estimate of μ as that obtained by fitting the two-component mixture. But weighting by $1/\sigma_i^2$ (i.e., by $1/\tau_1^2$ and $1/\tau_2^2$) will produce a different estimate, and it is easy to construct cases where such weighting produces a grossly biased estimate. This is because the unweighted mean implicitly combines the observations from the different components in the same proportions as those estimated by fitting the two-component mixture, whereas the weighted mean does not, unless τ_1^2 and τ_2^2 happen to be in the ratio of $1-p$ to p (which is unlikely).

The usual situation in practice is that the error standard deviations σ_i differ across grains, both within and between components. In that case, the estimate of μ obtained by fitting a two component mixture does differ from the unweighted mean equivalent dose — but typically not by very much if the differences between σ_is in the same component are small compared to those in different components. On the other hand, weighting by $1/\sigma_i^2$ will generally produce a rather different estimate.

Of course a more detailed numerical analysis would be needed to quantify these differences, but a general message is that if the y_is come from a two component mixture, then it could be misleading to combine them by weighting them by the reciprocals of their error variances ignoring the mixture structure, which is what the central age model does.

Finite mixture models are often used to estimate the parameters of specific sub-populations. The use here of a two component mixture as a form of 'error' distribution differs in concept, though it is not unknown in statistical applications where it has sometimes been used to deal with samples containing small numbers of outliers or 'unusual' values.

In the 'adjusted dose rate' method of Jacobs et al. (2008), a finite mixture model was fitted to the equivalent doses but the age was estimated from just one of the component means (μ_1, say) which was divided by an 'adjusted dose rate' (i.e., an estimate of $\mu_{\xi 1}$). That method, as I understand it, was used as an attempt to deal with equivalent doses that were thought to come from well-bleached grains that were buried at the same time but looked as if they were from a finite mixture distribution with one component containing a large majority of the grains. The rationale behind that method merits discussion, but there is no reason in principle why it should not give a valid estimate. Reasons for focusing on just one of the mixture components might include the possible unreliability of data in the other components, though this also raises the question of how to best estimate a dose rate specific to that component.

5. Models with multiplicative errors

Sometimes the dominant source of error variation in observed equivalent doses is multiplicative rather than additive. Signs of this are a strong positive skewness in a histogram of the y_is and a strong positive association in a scatter plot of s_i against y_i. Then an equation analogous to (1) may be expressed as

$$y_i = t\xi_i e^{u_i}\,, \tag{5}$$

where u_i is a random error drawn from a distribution with mean 0 and standard deviation τ_i, say. This could be rewritten as an additive model for the log doses:

$$\log y_i = \log t + \log \xi_i + u_i\,. \tag{6}$$

A parallel analysis to that in the previous section can be made for the model equation (6). For example, assuming that the log dose rates are a random sample from a normal distribution would lead to the usual 'logged' version of the central age model as being the optimal method.

It should be emphasised that equations (1) and (5) represent the same physical relationship. The only difference between them is in their 'error' distributions, which lead to different methods of estimating the burial dose μ. It would be possible to have either an additive error or a multiplicative error also for estimating the environmental dose rate μ_ξ, and there is no reason in principle why you should not have an additive error for the estimated dose rate and multiplicative errors for the equivalent doses. It would be wrong to say, for example, that because the dose rate is an arithmetic average of physical quantities then one should use an arithmetic average of equivalent doses to estimate the burial dose μ. In short, the appropriate method of estimation depends not only on the definition of the parameters but also on the *error* distributions.

6. Summary remarks

I have tried to highlight some statistical issues relating to how OSL ages are estimated when dose rates vary between grains, as is often the case for the beta dose rate contribution. Most of the statistical concepts I have used here are explained briefly in Galbraith & Roberts (2012, Appendix A). A key aspect is to identify the relevant parameters: not only the equivalent dose that corresponds to the burial dose (or the dose of interest), but also the relevant dose rate that corresponds to that equivalent dose. A second key aspect is that appropriate methods of estimating these parameters depend of the errors associated with individual measurements.

I have used models with additive errors for illustration. In that case, the assumption that the unobserved single grain dose rates follow a normal distribution leads to the 'unlogged' central age model for the equivalent doses. But the central age model is not necessarily appropriate for other dose rate disributions. Models with multiplicative errors may often be more appropriate in practice — and are in some ways simpler because relative errors do not depend on the scale of measurement — and the same issues arise there. In particular, the assumption that the unobserved single grain dose rates follow a log-normal distribution leads to the 'logged' central age model for the equivalent doses. Such models could be generalised to include situations where the OSL ages vary between grains. Their usefulness depends partly on how, or how much, any heterogeneity in dose rates

affects the estimation of the relevant equivalent dose, and indeed whether there is other relevant information about the dose rates that could be obtained, particularly about the nature or form of the dose rate distribution in any given application.

However, I would take issue with the idea that "modelling of the dose rate distribution is both unnecessary and undesirable" (Guérin et al., 2013, page 315). The simple analysis above has produced some useful insight, not only in suggesting appropriate methods of estimation in different situations but also in identifying a component of error variance that might be reduced if it were possible to measure single-grain dose rates. The assertions that such modelling "cannot improve accuracy, and must introduce additional uncertainties" (Guérin et al., 2013, page 315) are also incorrect, as explained above.

Statistical models are important not only for providing a basis for assessing the merits of any given method of estimation, but also for assessing sources of variation. The relevance of a statistical model to a given situation depends on the scientific context and it is not always easy to judge what models are most appropriate. Sometimes it can help to try more than one method. If different methods result in similar estimates, then some reassurance may be achieved; if not, then it may be illuminating to find out why.

Acknowledgments

I thank Jane Galbraith for criticisms and suggestions and Zenobia Jacobs and Bert Roberts for explanations of how dose rates are measured in OSL dating.

References

Galbraith, R.F. *On the mis-use of mathematics: a comment on "How confident are we in the chronology of the transition between Howieson's Poort and Still Bay?" by Guérin et al. (2013).* Journal of Human Evolution, 80: 184–186, 2015. doi: http://dx.doi.org/10.1016/j.jhevol.2014.10.006.

Galbraith, R.F. and Roberts, R.G. *Statistical aspects of equivalent dose and error calculation and display in OSL dating: An overview and some recommendations*. Quaternary Geochronology, 11: 1–27, 2012.

Guérin, G., Murray, A.S., Jain, M., Thomsen, K.J., and Mercier, N. *How confident are we in the chronology of the transition between Howieson's Poort and Still Bay?* Journal of Human Evolution, 64: 314–317, 2013.

Jacobs, Z., Wintle, A.G., Roberts, R.G., and Duller, G.A.T. *Equivalent dose distributions from single grains of quartz at Sibudu, South Africa: context, causes and consequences for optical dating of archaeological deposits*. J. Archaeol. Sci., 35: 1808–1820, 2008.

Reviewer

Regina DeWitt

Ancient TL

The Analyst software package for luminescence data: overview and recent improvements

G.A.T. Duller,[1*]

[1] Aberystwyth Luminescence Research Laboratory, Department of Geography and Earth Sciences, Aberystwyth University, Ceredigion, United Kingdom SY23 3DB

[*]E-mail: ggd@aber.ac.uk

Received: June 4, 2015; in final form: June 8, 2015

1. Introduction

Luminescence data collected for geochronology and dosimetry requires different types of manipulation and analysis in order to extract the information of interest. As automated systems for measurement of luminescence signals have developed (Bøtter-Jensen et al., 2010), the rate at which data can be acquired has increased. In addition, the development of equipment to obtain luminescence signals from individual mineral grains, whether using scanning systems (Duller et al., 1999) or imaging systems (Thomsen et al., in press), has further exacerbated this situation. It is not uncommon to make equivalent dose measurements of thousands of grains for each sample, involving tens of thousands of individual luminescence measurements.

In recent years a number of routines for analysis of luminescence data have been written in R (e.g., Kreutzer et al. 2012, Peng et al. 2013). These provide a range of tools for the manipulation and analysis of luminescence data and have the advantage that at least some of them (Kreutzer et al., 2012) are open source and thus it is explicit what numerical operations are undertaken. However, although these packages are capable of extremely complex analyses, they do require some understanding of the R environment, and there is currently no visual interface so interaction is primarily through command line statements (or scripts).

Analyst is a Windows based software package written in Delphi that has been developed over the last 15 years. It was originally written to analyse data collected in instruments built at Risø National Laboratory (e.g. Bøtter-Jensen et al. 2003), but can also be used for the analysis of data collected on other instruments provided that they generate compatible data files. Although the software has been used widely during the last 15 years, an overview of the capabilities of the software has never been given. Furthermore, a recent update to the software has included a number of significant enhancements. This paper seeks to summarise the overall capabilities of the software and to focus on recent improvements and additional capabilities.

2. Overview of software capability

The data format used by instruments built at Risø consists of a series of records, one for each luminescence measurement that is made. Each record contains a header (Table S1) which includes more than 60 parameters, some of which describe the conditions used to collect the data (e.g. the type of light source used for optical stimulation, the heating rate used for TL measurements, or the number of data points collected), and some of which are used to store information that can be used during data processing (e.g. whether the measurement is of a natural signal, or a regenerated signal). Following each header is a block of data collected during the measurement. The number of data points is specified in the header. The BINX file format consists of any number of headers and data blocks (i.e. header, data block, header, data block, header, data block...). The BIN file formats that were generated by previous versions of the Sequence Editor have the same overall structure as the BINX files, but the headers contain fewer parameters. Analyst is able to read all versions of BIN and BINX files.

Analyst provides a means for manipulating and viewing thermoluminescence (TL) and optically stimulated luminescence (OSL) data. The functionality can be split into three groups: (a) editing the header contents and selecting which data is appropriate for analysis, (b) visualisation of data, and (c) data analysis (e.g. construction of dose response curves, fading tests or component fitting).

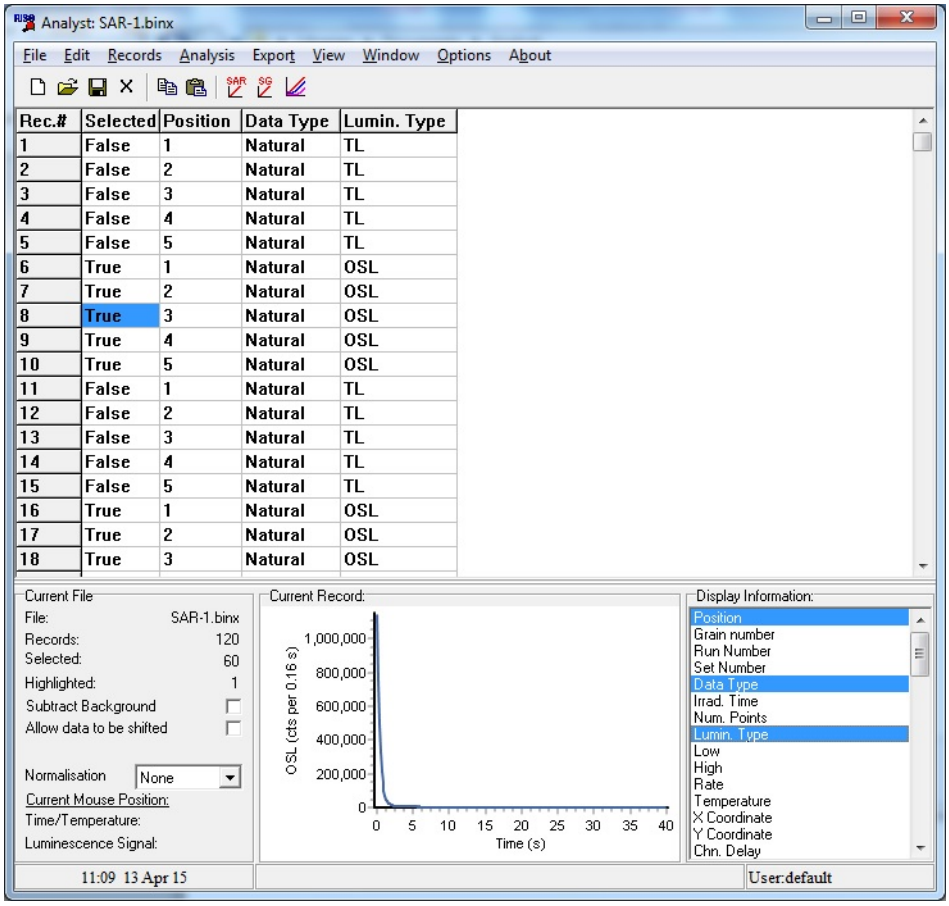

Figure 1: The front page of Analyst can be customised to show whichever parameters from the header are wanted - in this case the sample position on the carousel, the type of data and the type of luminescence measurement.

3. Editing header contents and selection of data

A large number of the parameters stored in the header for each luminescence measurement are set during data collection, for example the number of data points, the date and time of collection, the temperature at the time of collection, the heating rate that was used to reach this temperature, and if appropriate the type of optical stimulation that was used and the percentage stimulation power. Within the main screen of Analyst the user can select which of these parameters to display (Figure 1).

Some parameters are not set at run time, but can be edited in Analyst to give additional information that can be used in data analysis. For instance, when determining equivalent dose (D_e) using multiple aliquots it is important to specify which aliquots retain their natural luminescence signal, and which have had additive doses given, or regeneration doses given. Analyst allows any of the parameters in the header (except the number of data points) to be edited, either working on individual records at a time, or selecting a block of records and changing parameters for all of the records (using the 'Block Edit' function). The irradiation dose given to different aliquots is also important if equivalent dose is to be determined. The irradiation that each aliquot received prior to measurement may be edited in Analyst, though the irradiation time can also be automatically inserted into the BINX file by the Sequence Editor making it unnecessary to edit this parameter manually.

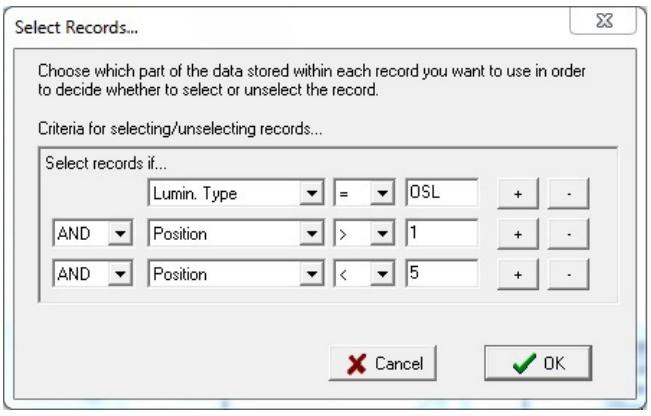

Figure 2: Selecting records from a BINX file for data collected for carousel positions 2, 3 and 4 and which are OSL measurements.

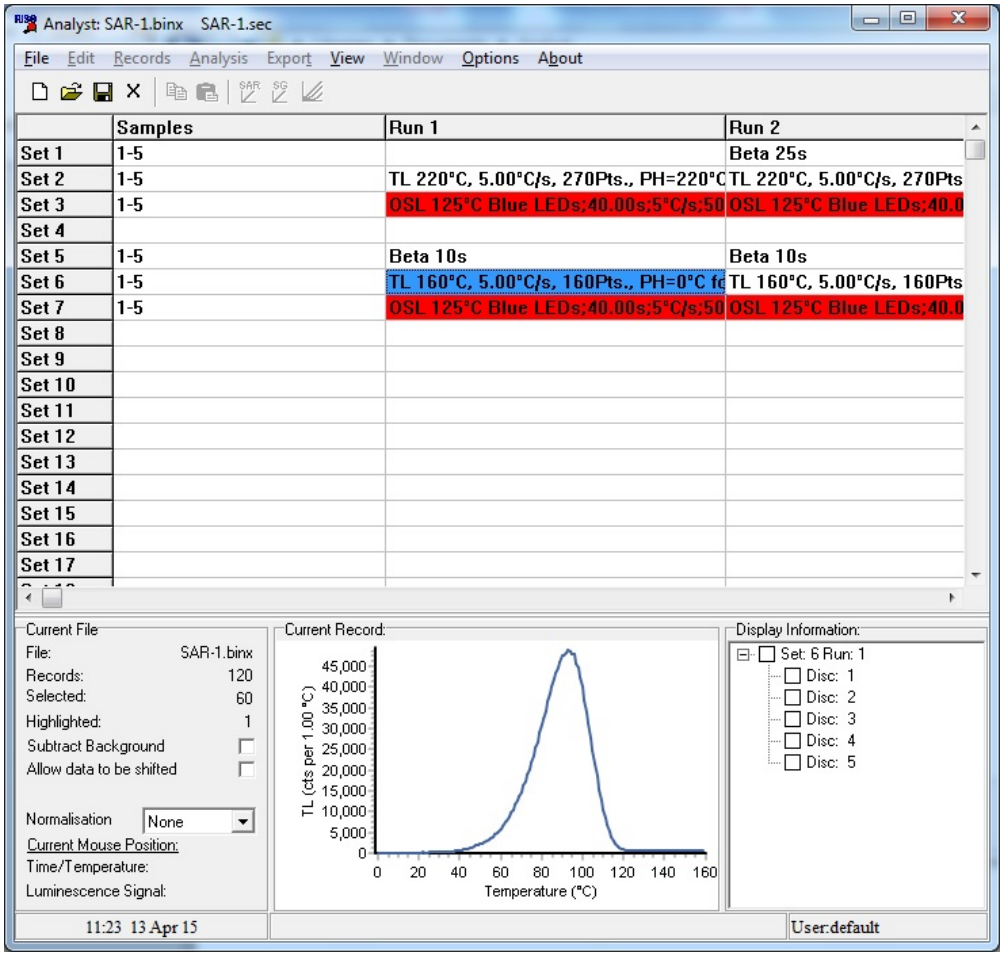

Figure 3: Visualising a BINX file using the sequence used to collect the data. In this example the cell shown in blue is highlighted. This part of the sequence collected TL data for aliquots in positions 1 to 5, and a list of these data is shown in the bottom right hand side of the screen. At present, none of this TL has been selected for analysis and so none of the tick boxes in the bottom right panel are selected, and the cell in the main panel is not coloured red.

Perhaps the most common activity under this heading is to select which of the records in a BINX file are to be used in subsequent data analysis. It is possible to delete records, but this deletion is permanent. A better approach is to mark which records are to be selected for subsequent analyses, and which are not. This is done by setting the 'Select' entry in the header of each record. Individual records can be selected or unselected individually using key strokes, but a more sophisticated approach is to filter which records are to be selected or unselected based upon some aspect of the header information (Figure 2). A common application of this approach would be in post-IR IRSL procedures (Thomsen et al., 2008) where IRSL has been measured at two or more temperatures (e.g. IR_{50} and IR_{225}), but analysis is required using only one of these data sets. This can be achieved by selecting records where the temperature parameter in the header is equal to 225, or can be achieved by selecting specific set numbers or run numbers.

A recent addition to Analyst is the ability to display the data in a format that reflects the sequence used to collect the data (Figure 3). This option is available if the copy of the sequence file (.SEC) used to collect the data is stored in the same directory where Analyst accessed the BINX file. This option is useful for navigating through complex sequences, and can also be used to conveniently select all the records collected by a command in the Sequence file.

4. Visualisation of data

Visualisation is an essential part of exploring data and Analyst provides a range of opportunities to do this. In the main display the data for individual luminescence measurements is displayed at the bottom of the screen. A new facility within the package is to be able to compare up to 30 records simultaneously by plotting them on the same graph (Figure 4a). It is possible to select which records to display either by dragging and dropping them onto the graph page, or by using a filtering command similar to that used to select data (Figure 2). The drag and drop option makes it possible to compare records from different BINX files. As many

(a)

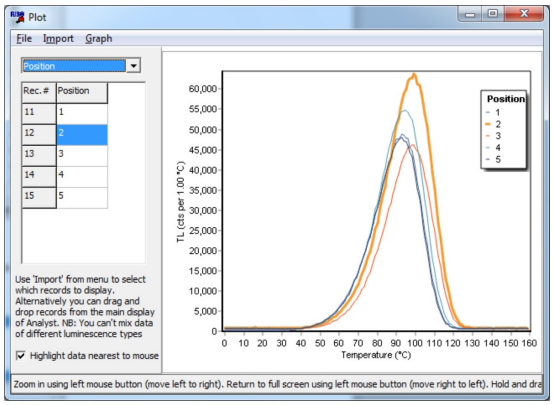

(b)

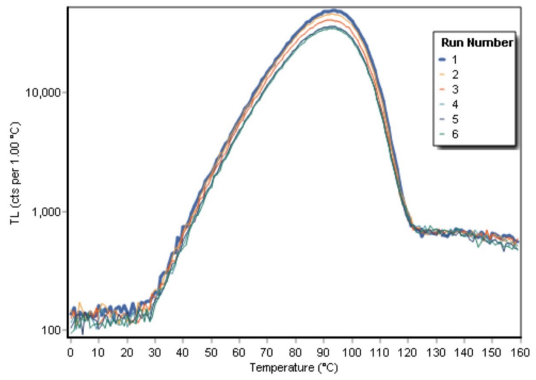

Figure 4: Selecting records from a BINX file for data collected for carousel positions 2, 3 and 4 and which are OSL measurements.

graphs as required can be displayed simultaneously. Furthermore, the characteristics of these graphs can be manipulated by the user, for instance whether to use logarithmic axes, what range of data to show on the axes, and the font size (e.g. Figure 4b).

5. Data analysis

Four major types of data analysis are supported in Analyst, (1) multiple aliquot determination of equivalent dose (D_e), (2) single aliquot (and single grain) determination of D_e, (3) calculation of fading rates and (4) component fitting of CW-OSL data.

5.1. Multiple aliquot D_e determination

Equivalent dose determination using multiple aliquots has been a feature of Analyst for many years, and both the additive dose and regenerative dose methods are supported. In each case it is possible both to calculate a D_e based upon integration of a region of interest (e.g. a specific temperature range for TL measurements, or a specific part of the OSL decay curve), and also to calculate a D_e plateau over a range of values (Figure 5). A variety of equations can be used to fit the dose response curve and the most important ones are listed in Table 1.

5.2. Single aliquot and single grain D_e determination

The same range of equations (Table 1) are also available when fitting dose response curves generated from single aliquot or single grain data sets. It has long been possible in Analyst to apply a range of acceptance criteria (Jacobs et al., 2006) to individual aliquots in order to assess whether the D_e value should be accepted for subsequent analysis or not. One of the more recent additions is the ability to screen on the basis of recuperation. The recuperation is assessed by looking at the signal when no dose has been given to the aliquot in the SAR sequence. The magnitude of the recuperated signal can be expressed in one of three ways. The first and most commonly used in published work, is to express the recuperated signal as a percentage of the natural signal. However, where samples are very young and the natural signal is weak, this may yield misleading results. One alternative is to express the recuperation as a percentage of the largest regeneration dose, and the final possibility is to extrapolate the dose response curve to where it intersects the dose axis and to use this as the 'apparent recuperated dose'. This provides an absolute measure (expressed in seconds or Gy) of the magnitude of the recuperated signal.

The assessment of uncertainty of the calculated D_e is critical, and the approach used in Analyst has been described previously by Duller (2007). The uncertainty in the measurement of individual luminescence signals is calculated from the counting statistics using the method described in Galbraith (2002), and an additional uncertainty associated with instrumental uncertainty (e.g. Armitage et al. 2000, Thomsen et al. 2005) can be combined in quadrature. Two approaches are possible in Analyst for how to propagate these uncertainties in luminescence intensity into uncertainties in equivalent dose. The default approach is to use the uncertainty calculated for the natural signal and propagate this through the interpolation onto the dose response curve. In

Linear

$$y = a + bx$$

Saturating exponential

$$y = a\left(1 - e^{-\frac{x+c}{b}}\right)$$

Saturating exponential plus linear

$$y = a\left(1 - e^{-\frac{x+c}{b}}\right) + gx$$

Sum of saturating exponentials

$$y = a\left(1 - e^{-\frac{x}{b}}\right) + c\left(1 - e^{-\frac{x}{d}}\right) + g$$

Table 1: Some of the equations available within Analyst for fitting dose response curves generated from multiple aliquot, single aliquot or single grain data sets.

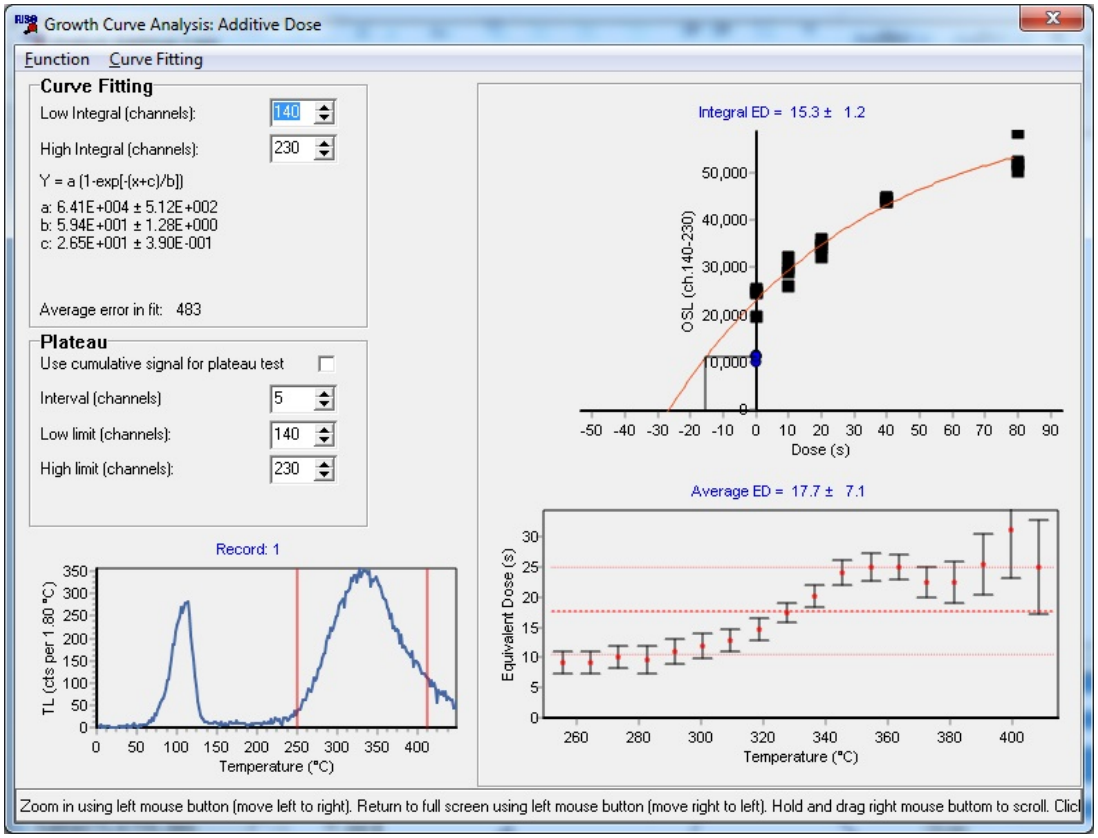

Figure 5: Example of analysis of a multiple aliquot additive dose data set, both showing the De calculated over a broad integral (upper right), and a plateau test (lower right) across a range of temperatures from 250 to 410°C

this approach, additional uncertainty in the fit of the data to the dose response curve is accounted for by including an additional uncertainty calculated from the average deviation of data points from the dose response curve (Eqn. 7 of Duller 2007). A second approach is to use a Monte Carlo method to determine the impact of uncertainties in all the L_x/T_x ratios determined for an aliquot upon the D_e. Whilst the Monte Carlo method requires greater computational time, analysis using this method is still fast on most modern computers. These two approaches are still available in Analyst. At high doses where there is significant curvature of the dose response curve the uncertainties are likely to be asymmetric (Murray & Funder, 2003) and Analyst will now calculate estimates of the positive and negative uncertainties (e.g. 230^{+25}_{-14}).

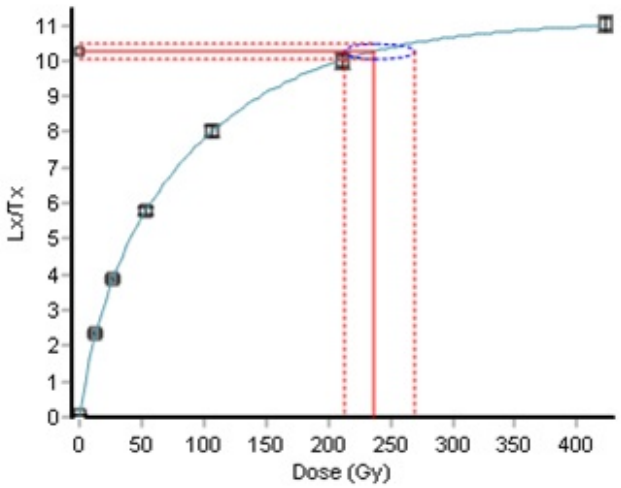

Figure 6: Dose response curve where the dose is expressed in Gray, generated by Analyst.

Analysis of BINX files containing data for tens, hundreds or thousands of equivalent dose measurements would take a long period of time to step through individually. Analyst is able to automatically step through a BINX file and attempt to calculate a D_e value for every aliquot or grain. In such automated analysis the acceptance criteria (e.g. recycling, recuperation) are used to decide whether an individual D_e estimate is accepted or rejected. A further addition to Analyst is the display of a range of summary statistics for the suite of D_e values obtained from a BINX file (at present these are based only on symmetrical uncertainties). The range of summary statistics describing the distribution of D_e values includes the mean, weighted mean, common age model, central age model, overdispersion (Galbraith et al., 1999) and mean square of weighted deviates (MSWD).

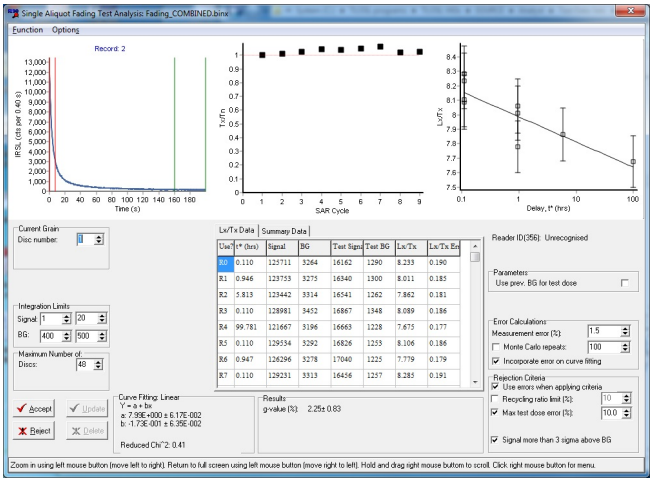

Figure 7: Fading data combining data measured for short storage periods (up to 6 hours) undertaken as part of a single sequence with data obtained after storage for 100 hours outside the instrument.

A final change in the most recent version of Analyst is the ability to calculate D_e values in Gray as well as seconds. The latest BINX format includes a parameter defining the dose rate of the source used for irradiation, so that irradiation times in seconds can be converted to Gy. This dose rate parameter may either be set automatically by the Sequence Editor when the data is collected, or changed in Analyst. Providing that a dose rate is set, the user can select whether to work in seconds or Gy when calculating D_e values. This makes it relatively simple to generate dose response curves of moderate quality for talks or publication which are expressed in Gy (e.g. Figure 6), and not seconds.

5.3. Calculating fading rates

The development of analytical protocols designed to isolate a signal from feldspar which has negligible anomalous fading (Thomsen et al., 2008) has reinvigorated study of this mineral group for geochronology. An important part of many studies is to explicitly test the rate of fading observed over laboratory timescales, and the methods outlined by Huntley & Lamothe (2001) and Auclair et al. (2003) are commonly used. These involve making prompt and delayed measurements, with a test dose correction applied. Critical to calculation of fading rates is knowledge of the time between irradiation and luminescence measurement so that t^* can be calculated (Auclair et al., 2003). The time since irradiation is one of the new parameters stored in BINX headers. If irradiation and subsequent measurement are undertaken within a single measurement sequence then this time since irradiation is set automatically when data are collected. If storage outside the automated reader is used to obtain data extending over longer periods of time, to improve the characterisation of the fading rate, then the time since irradiation needs to be input into the header by the user in Analyst. Once this time since irradiation parameter has been set, Analyst is able to calculate t^*, plot the drop in luminescence as a function of time (t^*) and fit the data to obtain a g-value (normalised to 2 days; Figure 7).

5.4. Component fitting of CW-OSL data

An experimental part of Analyst that has been included in the most recent version can be used to fit a sum of exponential decays to continuous wave OSL (CW-OSL) data (Figure 8). The equation used for fitting is

$$y = a + \left[n_1.b_1 e^{-b_1 t}\right] + \left[n_2.b_2 e^{-b_2 t}\right] + \left[n_3.b_3 e^{-b_3 t}\right]$$

where the number of components can be changed from one to three (the equation above is for a three component fit). A Levenberg-Marquardt method is used for fitting. Initial estimates of the parameters are generated automatically, but the user can edit these initial estimates if desired. Additionally, the user can fix any parameter (for instance the parameter b_1 which is the rate of decay of the fastest component, e.g. Rowan et al. (2012). The challenges of this type of fitting have been described by Bailey et al. (2011). Initial experiments to incorporate routine curve fitting of this type into Analyst so that component resolved D_e values can be determined have been undertaken, but at present the system is not sufficiently robust to be reliable, and more complex approaches such as the differential evolution method described by Bluszcz & Adamiec (2006) may be required to ensuring that global best fits are always obtained rather than falling into localised minima.

6. Accessibility of data

Analyst provides a range of options for manipulating, interrogating and analysing luminescence data, but any package of this nature can never be a complete solution to all the requirements that users may have. Analyst has been designed to make it as easy as possible for data to be exported so that it can be analysed using other software and so that more complex graphs can be generated. The main display of Analyst provides the opportunity to export both information from the headers and the luminescence data via the Windows clipboard, making it simple to paste into other packages (e.g. Excel), and similar facilities are available to export the data generated during single aliquot D_e determination or fading analysis for individual aliquots, or for groups of aliquots. The new graph tool used throughout the package also makes it possible to export both the raw data used to generate the graph (e.g. the doses and L_x/T_x ratios used to generate a dose response curve), and any of the analytical data produced (e.g. the dose response curve that is fitted, or the results of the Monte Carlo replicates used to estimate the uncertainty on D_e values).

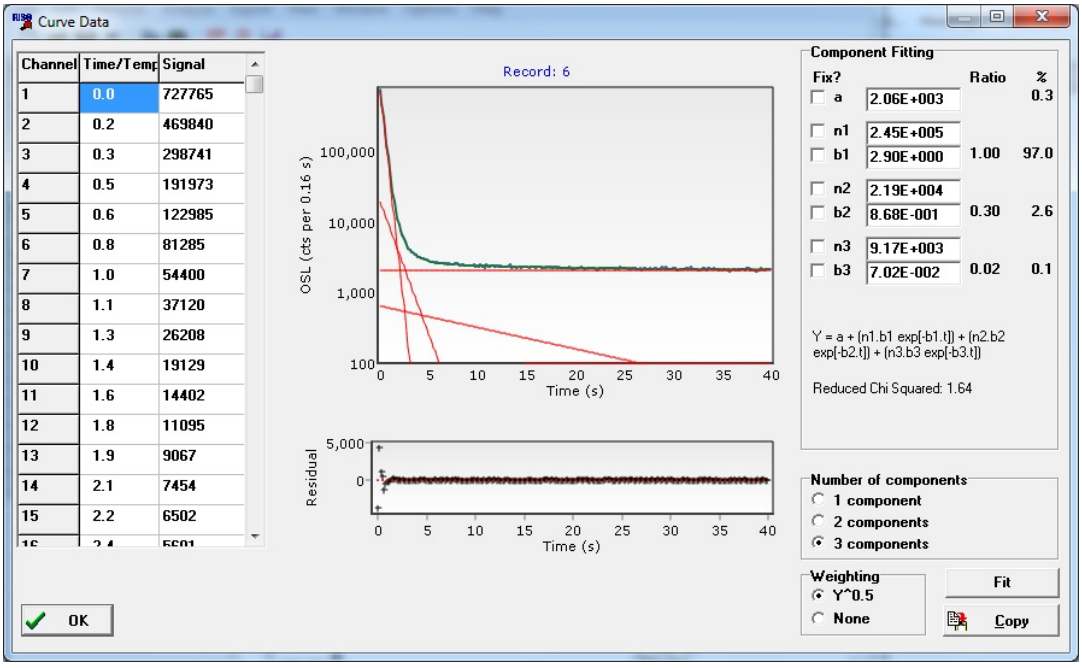

Figure 8: Example of component fitting a CW-OSL decay curve. The fitted parameters are given on the right hand side of the screen and can easily be copied to the clipboard for further processing.

7. Conclusion

The latest version of Analyst (v.4.31.7) is freely available either from the Aberystwyth Luminescence Research Laboratory website (http://www.aber.ac.uk/alrl) or from the DTU Nutech website (http://www.nutech.dtu.dk/english/Products-and-Services/Dosimetry/Radiation-Measurement-Instruments/TL_OSL_reader/Software). In addition to the new facilities described above, the package now contains an integrated context-sensitive help system (available by pressing F1 at any time) and a 77 page manual (Duller, 2015). It is hoped that this package will provide a user friendly, and highly visual, tool for analysing a range of luminescence data.

Supplementary Information

Table S1 is available as Supplementary Information at http://www.ecu.edu/cs-cas/physics/Ancient-Timeline/ancient-TOC33.cfm

Acknowledgments

I would like to thank colleagues in Aberystwyth and Risø over the last 25 years who have encouraged and supported me during the development of Analyst, and the many colleagues from around the world who have provided valuable feedback (including bug reporting) and suggestions for future improvements.

References

Armitage, S.J., Duller, G.A.T., and Wintle, A.G. *Quartz from southern Africa: sensitivity changes as a result of thermal pretreatment*. Radiation Measurements, 32: 571–577, 2000.

Auclair, M., Lamothe, M., and Huot, S. *Measurement of anomalous fading for feldspar IRSL using SAR*. Radiation Measurements, 37: 487–492, 2003.

Bailey, R.M., Yukihara, E.G., and McKeever, S.W.S. *Separation of quartz optically stimulated luminescence components using green (525 nm) stimulation*. Radiation Measurements, 46: 643–648, 2011.

Bluszcz, A. and Adamiec, G. *Application of differential evolution to fitting OSL decay curves*. Radiation Measurements, 41: 886–891, 2006.

Bøtter-Jensen, L., Andersen, C.E., Duller, G.A.T., and Murray, A.S. *Developments in radiation, stimulation and observation facilities in luminescence measurements*. Radiation Measurements, 37: 535–541, 2003.

Bøtter-Jensen, L., Thomsen, K.J., and Jain, M. *Review of optically stimulated luminescence (OSL) instrumental developments for retrospective dosimetry*. Radiation Measurements, 45: 253–257, 2010.

Duller, G.A.T. *Assessing the error on equivalent dose estimates derived from single aliquot regenerative dose measurements*. Ancient TL, 25: 15–24, 2007.

Duller, G.A.T. *Analyst v4.31.7 user manual*. Technical report, 77pp, 2015.

Duller, G.A.T., Bøtter-Jensen, L., Kohsiek, P., and Murray, A.S. *A high-sensitivity optically stimulated luminescence scanning system for measurement of single sand-sized grains*. Radiation Protection Dosimetry, 84: 325–330, 1999.

Galbraith, R.F. *A note on the variance of a background-corrected OSL count*. Ancient TL, 20: 49–51, 2002.

Galbraith, R.F., Roberts, R.G., Laslett, G.M., Yoshida, H., and Olley, J.M. *Optical dating of single and multiple grains of quartz from Jinmium rock shelter, northern Australia: part I, experimental design and statistical models*. Archaeometry, 41: 339–364, 1999.

Huntley, D.J. and Lamothe, M. *Ubiquity of anomalous fading in K-feldspars and the measurement and correction for it in optical datin*. Canadian Journal of Earth Sciences, 38: 1093–1106, 2001.

Jacobs, Z., Duller, G.A.T., and Wintle, A.G. *Interpretation of single grain D_e distributions and calculation of D_e*. Radiation Measurements, 41: 264–277, 2006.

Kreutzer, S., Schmidt, C., Fuchs, M., Dietze, M., Fischer, M., and Fuchs, M. *Introducing an R package for luminescence dating analysis*. Ancient TL, 30: 1–8, 2012.

Murray, A.S. and Funder, S. *Optically stimulated luminescence dating of a Danish Eemian coastal marine deposit: a test of accuracy*. Quaternary Science Reviews, 22: 1177–1183, 2003.

Peng, J., Dong, Z.B., Fan, F.Q., Long, H., and Liu, X.J. *R package numOSL: numeric routines for optically stimulated luminescence*. Ancient TL, 31: 41–48, 2013.

Rowan, A.V., Roberts, H.M., Jones, M.A., Duller, G.A.T., Covey-Crump, S.J., and Brocklehurst, S.H. *Optically stimulated luminescence dating of glaciofluvial sediments on the Canterbury Plains, South Island, New Zealand*. Quaternary Geochronology, 8: 10–22, 2012.

Thomsen, K.J., Murray, A.S., and Bøtter-Jensen, L. *Sources of variability in OSL dose measurements using single grains of quartz*. Radiation Measurements, 39: 47–61, 2005.

Thomsen, K.J., Murray, A.S., Jain, M., and Bøtter-Jensen, L. *Laboratory fading rates of various luminescence signals from feldspar-rich sediment extracts*. Radiation Measurements, 43: 1474–1486, 2008.

Thomsen, K.J., Kook, M.H., Murray, A.S., Jain, M., and Lapp, T. *Single-grain results from an EMCCD-based imaging system*. Radiation Measurements, in press. doi: doi:10.1016/j.radmeas.2015.02.015.

Reviewer

Regina DeWitt

Thesis Abstracts

Index

Hayley Candice Cawthra

The Marine Geology of Mossel Bay, South Africa

May 2014

Department of Geological Sciences, Faculty of Science, University of Cape Town

Degree: Ph.D.
Supervisor: John S. Compton

This thesis presents work undertaken to better understand the complex evolution of the terrestrial landscape now submerged by high sea levels offshore of Mossel Bay along the South Coast of South Africa. Three marine geophysical surveys and scuba diving were used to examine evidence of past sea-level fluctuations and interpret geological deposits on the seafloor. Additional geological mapping of coastal outcrops was carried out to link land and sea features and rock samples were dated using Optically Stimulated Luminescence (OSL). Geophysical investigations include a regional seismic survey extending from Still Bay in the west to Buffels Bay in the east out to a maximum water depth of 110 m; a high-resolution investigation of the Mossel Bay shelf using multi-beam bathymetry, side-scan sonar and sub-bottom profiling; and a shallow seismic pinger survey of Swartvlei, the most prominent coastal lake in the Wilderness Embayment. This study presents 9 discrete seismic sequences, and describes major offshore geomorphic features such as submerged sea cliffs, palaeo-coastal zones and fluvial systems. Oscillation in sea level between ∼2.7 and 0.9 Ma likely resulted in the formation of the prominent -45 m terrace, which separates a relatively steep inner from a low-gradient mid shelf. Beach and dune deposits span from Marine Isotope Stage 15 (MIS 15) (582 ka) to Recent based on an age model that integrates OSL ages and the established eustatic sea-level record. The most prominent deposits date from the MIS 6 glacial to MIS 5 interglacial periods and include incised lowstand river channels and regressive aeolianites that extended at least 10 km inland from their associated palaeoshorelines. The MIS 5 deposits include transgressive beachrock, an extensive foreshore unit which prograded on the MIS 5e highstand, and regressive beach and dune deposits on the shelf associated with the subsequent fall in sea level. MIS 4 lowstand incised river channels were infilled with sediment truncated during rapid landward shoreface migration at the MIS 4 termination. Low-energy, back-barrier MIS 4/3 sediments are preserved as a result of overstepping associated with meltwater pulses of the MIS 2 termination. The MIS 1 sediment wedge comprises reworked sediment and is best developed on the inner shelf. Holocene highstand sedimentation continues to prograde. Accommodation space for coastal deposits is controlled by antecedent drainage pathways and the gradient of the adjacent inner continental shelf. The geological deposits on the emergent shelf indicate a greatly expanded glacial coastal plain that potentially received more rain feeding low-gradient meandering rivers and wetland lakes. These extensive wetland environments provided a rich source of diverse food types which along with abundant marine resources on the shoreline made the Southern Coastal Plain an ideal habitat for our ancestors.

Melissa S. Chapot

Testing the maximum limit of quartz luminescence dating at Luochuan, China

January 2015

Aberystwyth University, Wales, United Kingdom

Degree: Ph.D.
Supervisors: Helen M. Roberts and Geoff A. T. Duller

This study investigates the maximum age limit of quartz luminescence dating, which assesses the time since the last exposure of quartz grains to sunlight. The maximum age range of this technique has been difficult to define because the limiting factors are sample dependent, and difficult to assess due to the dearth of independent age control comparisons for samples older than 50 ka. This study proposes a new concept for testing the maximum limit by comparing natural and laboratory measurements. Twenty-two samples of wind-blown dust (loess) from the Luochuan section of the Chinese Loess Plateau were analysed using two different luminescence signals: optically stimulated luminescence (OSL) and thermally transferred OSL (TT-OSL).

Expected ages for the samples were calculated using an age-depth model based primarily on correlations of palaeosol/loess boundaries with marine isotope stages. This framework of independent age control was transformed into sample-specific estimates of the radiation energy absorbed

in nature (palaeodose) using sample-specific environmental dose rates. Natural dose response curves were then constructed by plotting natural luminescence signals from samples of different ages against their expected palaeodoses. Maximum limits of OSL and TT-OSL techniques were tested by comparing their natural dose response curves with luminescence signals measured after irradiation in the laboratory (laboratory dose response curves).

Optimal measurement conditions for each of the two signals were investigated including signal definition, pre-heat treatments, test dose magnitudes (for the OSL signal), and pulsed-irradiation procedures (for the TT-OSL signal). The results suggest that the current maximum limit of quartz luminescence dating is circa 150 Gy, but that either the OSL or TT-OSL signal may provide the oldest reliable ages depending on the sample specific-signal characteristics. A newly proposed reliability threshold based on the luminescence signal of a naturally saturated sample is suggested to be a more appropriate maximum limit than $2D_0$ for samples of unknown age.

Margret C. Fuchs

Surface processes in response to tectonic and climatic forcing in the Pamir

October 2014

Helmholtz-Zentrum Dresden-Rossendorf, Helmholtz Institute Freiberg for Resource Technology, Freiberg, Germany

Degree: Dr. rer. nat. (Ph.D.)
Supervisors: Matthias Krbetschek, Richard Gloaguen, Frank Preusser, Andreas Lang

The interplay between topographic, tectonic, and climatic factors has fundamental relevance for understanding the mechanisms of mountain evolution and their susceptibility to changes. This thesis combines geomorphometric analyses with geochronological techniques to determine the rates of surface processes in the Pamir. Influenced by the Westerlies and the Indian Summer Monsoon, the Pamir provides ideal conditions to explore the surface process response to climate, and to compare such results with those found in other actively deforming mountains. This thesis addresses four main issues – (1) the distribution of tectonic and climatic factors in the Pamir, and their effects on geomorphometry; (2) the challenge of accurate sediment dating for precise process rates in high mountains; (3) the variability of fluvial incision and its implications for the evolution of the Pamir river network; and (4) which factors control erosion, and how erosion rates relate to local lowering of base levels.

Chapter 2.2 discusses how the collinearity of the major tectonic structures and mountain ranges exert long-term control on flow orientation and local base levels. Due to the dry climate on the Pamir Plateau, fluvial activity is low, and glacial processes are restricted to high altitudes. High topographic variability at the Pamir margins coincide with both, neotectonic activity along orogenic bounding faults and orographic precipitation from the Westerlies. The trunk stream, the Panj River, indicates major re-organizations of the river network. Successive river captures across the Pamir domes suggest dominant structural control accompanied by possible re-activation of dome bounding faults.

Luminescence dating is of paramount importance for decoding the sedimentation histories, but material from high mountains is challenging due to differential bleaching histories and postdepositional sediment mixing. To address this, Chapter 3.2 describes a transparent, reproducible analysis routine in three data processing templates using the R package 'Luminescence'. The challenges posed by properties of high mountain materials are addressed in Chapter 3.3, comparing multiple grain and single grain techniques applied to quartz, K-feldspar and plagioclase. These methods allow us to identify prominent events in sediment deposition without interference from bleaching and sediment mixing, or signal loss due to anomalous fading.

Chapter 4.2 applies optically stimulated luminescence (OSL) methods to quantify the variations in fluvial incision along the Panj River. Paleo-glaciations during Marine Isotope Stage (MIS) 2 and MIS 1/2 may have triggered the deposition of terrace sediments, but the rate of incision is primarily consistent with terrace location, rather than time of formation. Where the Panj cuts across the Shakhdara Dome in the southern Pamir, high incision rates of 7 - 10 mm/yr indicate intense river adjustment. Lower incision rates of 2 - 4 mm/yr are consistent with more graded profile sections of the Panj parallel to southern dome boundaries. To the north-east, the Panj incision reflects transient conditions - only the increased incision of 6 mm/yr marks the river response across the Darvaz Fault Zone. These data highlight the structural control of sudden base level drop due to successive river captures, while climatic factors - as well as rock erodibility and drainage architecture - are of secondary importance.

Chapter 5.2 complements the indications from geomorphometry and fluvial incision with cosmogenic nuclide (CN)-based basin-wide erosion rates. Results suggest a rapid average topographic evolution in the Pamir. However, the pace of erosion at the Pamir Plateau shows a strong contrast to the Pamir margins. High erosion rates of 0.55 - 1.43 mm/yr integrate over millennial scale conditions at the western Pamir margin, whereas lower rates of 0.05 - 0.17 mm/yr at the Pamir Plateau also integrate effects of the MIS 1/2 deglaciation. The correlation of erosion with steep slopes (R_2 of 0.82) defines the precondition for high rates in the Pamir. The influence of precipitation only becomes evident in multiple linear regression analyses, explaining erosion as a function of slope and precipitation (R_2 of 0.93). The almost tenfold discrepancy between fluvial incision rates along the Panj River and basin-wide erosion rates reflects the transience of the landscape with the Panj incising faster than hillslopes adjust. The rate of adjustment increases where the Westerlies supply moisture during winter. This suggests that an effcient sediment transport relates to seasonal peak discharge during the melting season.

The methods and results described, highlight the dominance of tectonic structures in controlling surface processes. In contrast to the southern escarpment of the Himalayas where the Indian Summer Monsoon provides intensive rainfalls, precipitation in the Pamir is limited and hence, works as a restricting factor for hillslope adjustment to fluvial incision. Major reorganisations of the Pamir River network highlight river captures as an important trigger of high surface response rates due to the sudden drop in base levels.

A PDF of this thesis can be downloaded from *Ancient TL*.

Vinícius Ribau Mendes

Santa Catarina coastal dunefields chronology and sedimentology

May 2012

Institute of Geociences University of São Paulo, São Paulo , Brazil

Degree: Master

Supervisors: Paulo César Fonseca Giannini

This thesis refers to five areas with active and stabilized eolian dune fields in the central coast of the Santa Catarina State, southern Brazil. In this region, a recent tendency to stabilization of active dune fields is inferred from the comparison between aerial photographs of different years. Meteorological data obtained between 1962 and 2010, including daily records of rainfall, wind intensity and wind direction, indicate increasing precipitation and weakening wind to this period. The combination of these two factors inhibits the eolian sediment transport to the dune field, as effect of increasing sand cohesion by wetting and plant colonization in deflation zones. Being persistent in the last three decades, these factors have reduced gradually the sand areas exposed to eolian reworking and decreased more and more the effective eolian drift, culminating in the stabilization of dune fields.

The sedimentary deposits of eolian dunes and paleodunes were grouped, by morphological, stratigraphic, granulometric and mineralogical criteria in four generations (G1 to G4), analogous to that previously recognized in the literature. The older generation (G1) has a wider age distribution than previously thought and can be subdivided regarding the geochronological aspect. The grain-size analysis data indicate trends of sediment coarsening, better sorting and more positive skewness, from the older to the younger generation, what is attributed to the influence of successive reworking of sediments between generations, without discarding the effect of changes in the transport energy and/or beach morphodynamics. The ages of the three older generations obtained by optically stimulated luminescence (OSL) method show coincidence with contexts of stable coastline and with climate in transition from less to more wet.

The observed relationship between the OSL ages, relative sea level (RSL) and paleoprecipitation curves, besides the model of recent dune stabilization (by the wet increasing and wind energy decreasing), allow us to suggest that the initiation of the dune fields in their different generations, in this coastal region, can be favored by moments of stable and / or in reversal trend RSL, as well by less humid and more windy weather. In other hand, the stabilization of the dune fields would be favored by higher RSL, increasing rain and decreasing wind intensity. From the perspective of climate control, the mentioned condition to initiation of dune fields agree with moments of weakening of the South America Summer Monsoon System (SASM), related to warmer periods in the northern hemisphere. Analogously, the favorable condition for the stabilization of dune fields would coincide with moments of intensification of the SASM, related to colder periods in the northern hemisphere.

A PDF of this thesis can be downloaded from: http://www.teses.usp.br/teses/disponiveis/44/44141/tde-27022013-144047/pt-br.php

Ferdinand Messens

Luminescence dating of tsunami sand in south central Chile a feasibility study

June 2014

Department Geology and Soil Science, Ghent University, Ghent, Belgium

Degree: Master

Supervisors: Dimitri Vandenberghe, Marc De Batist, Philipp Kempf

This work presents an explorative study into the potential of luminescence dating techniques for application to tsunami-laid sands in south-central Chile. The investigated sediments come from a core that was taken in the coastal Lake Huelde; the sequence was about 5 m long and comprised six sandy layers interpreted as being deposited by tsunami events. In the frame of this work, four of these layers were examined using luminescence methods.

The luminescence investigations initially focussed on quartz. However, no pure quartz could be extracted from the samples. The luminescence characteristics of the separates were therefore investigated using a double-SAR protocol, which uses stimulation with IR light prior to the OSL-measurement to minimize the contribution from feldspar. The post-IR OSL signals were dim, not dominated by a fast component, and behaved very poorly in the SAR protocol (as indicated by the SAR procedural tests: recuperation, recycling ratio and dose recovery). Microscopic observations using thin sections were used to relate this luminescence behaviour to the mineralogical composition and provenance of the sediments. It is concluded that OSL signals from quartz are not suitable for dating these tsunami-laid sands.

The investigations were therefore directed towards an alternative dosimeter, K-feldspar. Stimulation was with IR at 50°C (IR50) and the luminescence characteristics of this signal were investigated using a SAR protocol. All samples

emitted bright IRSL signals that behaved well in the SAR protocol in terms of recycling and recuperation. The dependence of equivalent dose, anomalous fading and fading-corrected age on preheat temperature was examined for two samples. It is concluded that a low preheat temperature of 60 s at 80°C is required to minimize significant age overestimation owing to thermal transfer. In line with earlier finds, we find no evidence that higher preheat temperatures isolate a signal that is thermally more stable. The distribution of equivalent dose, fading rate and fading-corrected age was then examined in each of the four samples. Broad distributions were observed for all samples. Apart from a few outlying values, the corrected age distributions in the two lowermost samples appear to belong to a single population. The spread observed in these samples (RSD: 20 %) was therefore taken as a measure for the spread that can be expected for a well-bleached, undisturbed and unmixed sample. The distributions obtained for the two uppermost samples are clearly asymmetric, with values extending over a wider and higher age range. Using our estimate of the spread that can be expected in the ideal situation, the population with the lowest corrected ages was isolated from these distributions; these values are more likely to approximate the depositional age of the sediments. The fading-corrected IR50-ages are broadly consistent with the stratigraphic position of the samples and range from 0.174 ka to 1.64 ka. Interestingly, a slight age inversion was observed for the two lowermost samples; it remains to be established whether this relates to an underestimation of the uncertainties, dosimetric issues (e.g. related to the non-uniformity in the radioactive surroundings of the samples) and/or the specific nature of the erosion and transport process. Following the investigations using IR50, we also briefly examined the potential of a post-IR IRSL signal, which was obtained by stimulating with IR at 290°C following a stimulation with IR at 50°C (pIRIR290); this approach has been shown to circumvent any correction for anomalous fading. The pIRIR290-signal behaves well in the SAR protocol, and laboratory measurements of signal stability confirm the earlier finds with respect to anomalous fading. The pIRIR290-ages overestimate the IR50-ages by 6 ka, which may be due to thermal transfer and/or incomplete resetting. It is concluded that, despite its attractive dosimetric properties, the pIRIR290 signal is unlikely to be applicable to Holocene deposits. In general, it is concluded that IR50-signals from K-feldspar provide a powerful means for establishing chronologies for tsunami-laid sands in this region. This conclusion is corroborated through a comparison of the IR50-ages with the available independent age information (such as historical records and ^{14}C-dating of comparable sequences in the study region). The study also provides the first evidence for a tsunami triggered by the 1837 AD seismic event. Finally, our study also demonstrates the importance of direct numerical age information for tsunami-laid sands to correlate palaeoseismological records derived from cores that were taken in the same sediment archive (i.e. Lago Huelde).

A PDF of this thesis can be downloaded from: http://lib.ugent.be/fulltxt/RUG01/002/163/647/RUG01-002163647_2014_0001_AC.pdf

Fabiano do Nascimento Pupim

Geomorphology and paleo-hydrology of the Cuiabá and São Lourenço fluvial megafans, Quaternary of Pantanal (Geomorfologia e paleo-hidrologia dos megaleques dos rios Cuiabá e São Lourenço, Quaternário da Bacia do Pantanal)

September 2014

Instituto de Geociências e Ciências Exatas, Universidade Estadual Paulista, Rio Claro - SP, Brazil

Degree: D.Sc.
Supervisor: Mario Luis Assine

The Upper Paraguay River Basin comprises three areas with remarkable differences regarding their physical and biological aspects: plateaus, erosional lowlands and the Pantanal plain. The Pantanal is the worlds largest freshwater wetland and is characterized as a complex depositional system tract fed by fluvial megafans. The origin of these large depositional landforms is related to the tectonic setting and basin subsidence; however the Late Quaternary dynamic has been mainly influenced by climate change and interactions with the surroundings erosional terrains. Considering the peculiarities and environmental importance of the area, the main aim of this study was to investigate aspects of the Late Quaternary evolution of fluvial megafans formed by the Cuiabá and São Lourenço rivers in the northern portion of the Pantanal, as well as the degradational systems of the Cuiabana lowlands in the source area. Remote sensing, geomorphological, facies analysis and geochronological data were used to achieve these goals. Satellite images and digital elevation models were used to unveil contrasting channel patterns and distinguish geomorphic zones. Optically stimulated luminescence dating (OSL) allowed to establish a chronology and to reconstruct the chain of main events that shaped the megafans. The depositional systems formed by Cuiabá and São Lourenço rivers are, respectively, the second and the third biggest fluvial megafans in the Pantanal, exhibiting fan shaped morphology, low topographic gradient and unconfined flow to downstream. Three different fluvial channel styles were recognized, reflecting distinct phases of aggradation and incision during the Late Quaternary. Distributary braided paleochannels preserved on the surface of Pleistocene lobes record semi-arid climate conditions and scarce vegetation, and a period of high aggradation during the Late Glacial. The Pleistocene lobes have been dissected by small streams radiating from the fan apex and the rain waters tend to produce widespread sheet flows, reworking the surficial sediments. No OSL ages were found between the Late LGM and the Holocene, indicating very low and localized sedimentation, and a period of fluvial incision in the upper fan settings; truncate ancient lobes' surface and create the incised valleys. The incised valleys were

mainly filled by Early and Middle Holocene-aged meander belt deposits, which consist of very fine sands interbedded with fine-grained deposits. Currently, the incised valley is a zone of sediment bypass and works as a feeder channel of the distal distributary sinuous channels. The distal lobes are the modern depositional site, formed by progradation of avulsion belts into a broad floodbasin. The Holocene avulsions are random. The timescale of regional avulsion (lobe changes) are around thousands of years, whereas the local avulsions (bifurcation in small channels) take less than ten years. The paleo-hydrological changes (braided-incision-meandering) observed in both systems were mainly controlled by Late Quaternary climatic fluctuations, being an example of tropical and subtropical river response to global climate changes. Cosmogenic nuclide analysis (^{10}Be) enabled the determination of erosion rates and exposure ages in the Cuiabana lowdands. The relief denudation has been driven by differential erosion and strong lithological control. The laterization of the deposits rich in quartzite clasts appears to be a key factor maintaining hilltop summits of the planation surface over long timescales. Clastic-lateritic deposits have slow erosion rates, similar to the worlds slowest, preserving an ancient surface planation whose minimum age is Middle Pleistocene.

Keywords: fluvial megafans; channel patterns; Cuiabana lowlands; cosmogenic nuclides; OSL dating.

Eren Şahiner

TL/OSL And ESR Methods Used in Paleoseismology Studies: Kütahya-Simav and North Anatolian Fault Zone

April 2015

Ankara University, Graduate School of Natural and Applied Sciences, Department of Engineering Physics

Degree: Ph. D.
Supervisors: Niyazi Meriç

Thermoluminescence (TL), Optically Stimulated Luminescence (OSL) and Electron Spin Resonance (ESR) techniques stand among the basic research tools in the fields of (a) ionizing radiation dosimetry, (b) archaeological and geological dating and retrospective dosimetry, (c) authenticity testing of archaeological artifacts. Dating by applying these methods is based on the measurement of trapped electronic charges that are accumulated in crystalline materials as a result of low-level natural radioactivity present at sites, which help to calculate the time since the traps were empty. For TL and OSL, the population of trapped charges is measured by the amount of light emitted by electrons released from their traps via heat and light, correspondingly. Electrons are not evicted by ESR spectrometry; the strength of the signal emitted by trapped electrons provides a measure of the population size.

The present study examined the feasibility of using TL/OSL and ESR techniques for paleosismological studies in order to date fault gouges traces from Anatolia. The basic effort was towards examining the validity of basic assumptions on luminescence dating technique using samples with age constraints. The aim and scope of the thesis can be summarized in two broad categories, including methodological aspects and feasibility of dating. In this process, new protocols were developed, tested and applied, including multiple, independent equivalent dose estimation approaches which were adopted, using both luminescence and ESR techniques; de-convolution approximations as well as Thermally Assisted OSL, TA-OSL, stimulation with simultaneous heating of the Very Deep Traps (VDT) were applied towards possible extension of age limit in luminescence dating applications. According to the results yielded, in some special conditions age limits could be extended over one order of magnitude using TA-OSL after stimulating VDT in the natural minerals. Furthermore, one approach is succesed in order to improve the understanding of the trapped electron recombination lifetime in the crystal sutructure. Finally, it was established that Infrared stimulated luminescence (IRSL) of samples of mixed mineralogy at elevated temperatures stimulates quartz mineral as well.

This study therefore provides a basis for the application of trapped charge dating methods and concludes that it can play a significant role in studies related to trap-charge dating researches and luminescence mechanisms in the crystal structures.

Keywords: Thermoluminescence (TL), optically stimulated luminescence (OSL), electron spin resonance (ESR), de-convolution, Very Deep Traps (VDT), Thermally Assisted OSL (TA-OSL), paleosismologi, luminescence dating, ESR dating, fault gouges, PostIR-OSL, SAR, equivalent dose, annual dose.

Qingfeng Shao

Combined ESR/U-series Dating of Fossil Teeth from Middle Pleistocene Sites in Northern Europe and Mediterranean Area: Contributing to the Chronology of the Acheulian Settlements of Europe

2011

Muséum National d'Histoire Naturelle; Département de Préhistoire

Degree: Ph.D.
Supervisors: Jean-Jacques Bahain, Christophe Falguères

Combined ESR/U-series dating of fossil teeth has been increasingly used in geochronological research over the past two decades. Results prove that it can be potentially applied to sites in different geological contexts (fluvial/lacustrine or karstic environments) over a timescale of $10^4 - 10^6$ years, and it is an interesting dating method for studies of the Pleistocene human migrations, such as the dispersal of Acheulian bifacial technology.

The present work mainly contains 1) a detailed study of the combined ESR/U-series dating theory for understand-

ing its limitations; 2) the development of an age calculation software ESRUSAGE with Monte Carlo simulation for age and age error estimation; 3) the creation of a new U-uptake model named AU model, which allows age calculations for teeth that probably experienced U-leaching; and geochronological applications to four major archaeological sites: 4) Mauer, Germany, eponym locality of discovery of the Mauer mandible, holotype of the *Homo heidelbergensis* species; 5) Isernia la Pineta, Italy, allowing a comparative study with $^{40}Ar/^{39}Ar$ dating; 6) Thomas Quarry 1 Hominid Cave, Morocco, Acheulian site previously dated by OSL dating of quartz and LA-MC-ICP-MS on hominin tooth; and 7) Qesem Cave, Israel, allowing a comparison with TL dating of heated flints and $^{230}Th/^{234}U$ dating of speleothems.

These applications demonstrate that the newly developed ESRUSAGE program and AU model really improve the applicability of combined ESR/U-series dating approach. Comparative studies show that this approach can be successfully used to Middle Pleistocene caves and open air sites, but can be limited by geological dosimetric changes. The age estimates obtained in the present work on the four Acheulian related sites support the general consensus that the first appearance of Acheulian in Europe is probably not before 700 - 600 ka.

Keywords: ESR/U-series dating method; Early Middle Pleistocene; Acheulian settlement; U-uptake and leaching; Mauer; Isernia la Pineta; Thomas Quarry 1; Qesem Cave

Erratum: Thesis Abstracts

Erratum: In the last issue we published an incorrect abstract for Sebastian Kreutzer's dissertation. The correct abstract is:

Sebastian Kreutzer

Luminescence based chronologies on Late Pleistocene loess-palaeosol sequences: An applied-methodological study on quartz separates

February 2013

Geographical Institute, Geomorphology, University of Bayreuth, 95440 Bayreuth, Germany
(present address: IRAMAT-CRP2A, Université Bordeaux Montaigne, Maison de l'Archéologie, Esplanade des Antilles, 33607 Pessac Cedex, France)

Degree: Dr. rer. nat. (Ph.D.)
Supervisors: Markus Fuchs, Ludwig Zöller

Understanding morphological processes that sculpt former terrestrial landscapes is one of the driving rationales in Quaternary research. Loess records have been found to be valuable archives for reconstructing palaeoenvironmental conditions. However, once identified, characterised and classified by fieldwork, the stratigraphic significance of such records has to be revealed by numerical dating. Luminescence dating, especially optically stimulated luminescence (OSL), is the leading dating approach for establishing chronologies on loess archives. Furthermore, the development of luminescence dating techniques on sediments is closely connected with the history of loess research and vice versa. As part of the European loess belt the Saxonian Loess Region is located in a transition zone between oceanic dominated western and continental dominated eastern climates. The Saxonian Loess Region comprises up to 20 m thick Weichselian loess accumulations, with intercalated palaeosols. For the first time, during the work on this thesis, high-resolution numerical chronologies were established in the Saxonian Loess Region on five loess sections using OSL dating on quartz separates. The dating was employed as a comparison of three quartz grain size fractions commonly used for luminescence dating: (1) coarse (90–200 μm), (2) middle (38–63 μm) and (3) fine grain (4–11 μm). As a survey on four loess sections, three from Germany (Saxony and Saxony-Anhalt) and one from the Czech Republic, these studies investigate the question whether the use of different grain size fractions from one sample yield consistent luminescence characteristics and age results. In summary seven studies are presented along with an extended summary. Four studies present numerical chronologies using OSL dating techniques on different grain size and (mineral) fractions. Two studies deal with technical issues that arose during the dating applications. Firstly, an **R** package for luminescence dating data analysis ('Luminescence') was developed and secondly, the cross-bleaching behaviour of IR-LEDs of Risø luminescence readers were quantified. One study treats the question whether the common practice of using an identical alpha-efficiency (a-value) for the conventional IR_{50} and $pIRIR_{225}$ dating is justified under theoretical and empirical viewpoints. It was found that for the established numerical chronologies on loess the fine grain quartz fraction results in reliable age estimates up to the Eemian (MIS 5e, 5d). The high-resolution dating in Saxony uncovered a prominent hiatus of ca. 30 ka between the early and the late Weichselian found in all investigated loess sections in Saxony. The fine grain quartz age results are confirmed by the polymineral fine grain dating. For lower dose ranges ($D_e < 100$ Gy) age results of all three grain size fractions agree within uncertainties. However, the coarse and middle grain fractions show highly scattered distributions. For higher doses ($D_e > 180$ Gy) the luminescence signals of the coarse and middle grain fractions are in saturation. In contrast, the luminescence signal of the fine grain fraction still grows and is reproducible as shown by test measurements. The results of a cross-bleaching survey on 10 luminescence readers revealed substantial cross-bleaching behaviour of the IR-LEDs (mean cross-bleaching: ca. 0.026 %), which is an order of magnitude higher than for blue LEDs. The investigation on the a-values of polymineral fine grain samples gave evidence for significant differences between the mean a-values obtained with the IR_{50} and the $pIRIR_{225}$ signals. The a-value obtained with the $pIRIR_{225}$ signal was found to be always higher, but further investigations are needed.

A PDF of this thesis can be downloaded from:
https://epub.uni-bayreuth.de/1673

Bibliography

Compiled by Daniel Richter

From 1st November 2014 to 15th May 2015

Alexanderson, H., and Fabel, D. (2015). Holocene Chronology of the Brattforsheden Delta and Inland Dune Field, Sw Sweden. *Geochronometria* **42,** 1-16.

Antoine, P., Goval, E., Jamet, G., Coutard, S., Moine, O., Hérisson, D., Auguste, P., Guérin, G., Lagroix, F., Schmidt, E., Robert, V., Debenham, N., Meszner, S., and Bahain, J. J. (2014). Les séquences loessiques pléistocène supérieur d'havrincourt (Pas-de-Calais, France): Stratigraphie, paléoenvironnements, géochronologie et occupations paléolithiques. *Quaternaire* **25,** 321-368.

Arbogast, A. F., Luehmann, M. D., Miller, B. A., Wernette, P. A., Adams, K. M., Waha, J. D., O'Neil, G. A., Tang, Y., Boothroyd, J. J., Babcock, C. R., Hanson, P. R., and Young, A. R. (2015). Late-Pleistocene paleowinds and aeolian sand mobilization in north-central Lower Michigan. *Aeolian Research* **16,** 109-116.

Asfora, V. K., Guzzo, P. L., Pessis, A.-M., Barros, V. S. M., Watanabe, S., and Khoury, H. J. (2014). Characterization of the burning conditions of archaeological pebbles using the thermal sensitization of the 110 °C TL peak of quartz. *Radiation Measurements* **71,** 485-489.

Aydaş, C., and Aydın, T. (2015). An investigation of the dosimetric and kinetic properties of sand using ESR and TL techniques. *Applied Radiation and Isotopes* **101,** 65-74.

Bacon, A.-M., Westaway, K., Antoine, P.-O., Duringer, P., Blin, A., Demeter, F., Ponche, J.-L., Zhao, J.-X., Barnes, L. M., Sayavonkhamdy, T., Thuy, N. T. K., Long, V. T., Patole-Edoumba, E., and Shackelford, L. (2015). Late Pleistocene mammalian assemblages of Southeast Asia: New dating, mortality profiles and evolution of the predator–prey relationships in an environmental context. *Palaeogeography, Palaeoclimatology, Palaeoecology* **422,** 101-127.

Bakraji, E. H., Rihawy, M. S., Castel, C., and Abboud, R. (2015). PIXE multivariate statistics and OSL investigation for the classification and dating of archaeological pottery excavated at Tell Al-Rawda site, Syria. *Nuclear Instruments and Methods in Physics Research Section B: Beam Interactions with Materials and Atoms* **347,** 20-25.

Bickel, L., Lüthgens, C., Lomax, J., and Fiebig, M. (2015). Luminescence dating of glaciofluvial deposits linked to the penultimate glaciation in the Eastern Alps. *Quaternary International* **357,** 110-124.

Boeda, E., Clemente-Conte, I., Fontugne, M., Lahaye, C., Pino, M., Felice, G. D., Guidon, N., Hoeltz, S., Lourdeau, A., Pagli, M., Pessis, A.-M., Viana, S., Da Costa, A., and Douville, E. (2014). A new late Pleistocene archaeological sequence in South America: the Vale da Pedra Furada (Piaui, Brazil). *Antiquity* **88,** 927-953.

Brown, A. G., Basell, L. S., and Toms, P. S. (2015). A stacked Late Quaternary fluvio-periglacial sequence from the Axe valley, southern England with implications for landscape evolution and Palaeolithic archaeology. *Quaternary Science Reviews* **116,** 106-121.

Burrough, S. L., Thomas, D. S. G., Orijemie, E. A., and Willis, K. J. (2015). Landscape sensitivity and ecological change in western Zambia: The long-term perspective from dambo cut-and-fill sediments. *Journal of Quaternary Science* **30,** 44-58.

Cano, N. F., Munita, C. S., Watanabe, S., Barbosa, R. F., Chubaci, J. F. D., Tatumi, S. H., and Neves, E. G. (2014). OSL and EPR dating of pottery from the archaeological sites in Amazon Valley, Brazil. *Quaternary International* **352,** 176-180.

Cano, N. F., Ribeiro, R. B., Munita, C. S., Watanabe, S., Neves, E. G., and Tamanaha, E. K. (2015). Dating and determination of firing temperature of ancient potteries from São Paulo II archaeological site, Brazil by TL and EPR techniques. *Journal of Cultural Heritage* **16,** 361-364.

Casas, L., Ramírez, J., Navarro, A., Fouzai, B., Estop, E., and Rosell, J. R. (2014). Archaeometric dating of two limekilns in an industrial heritage site in Calders (Catalonia, NE Spain). *Journal of Cultural Heritage* **15,** 550-556.

Chauhan, N., Adhyaru, P., Vaghela, H., and Singhvi, A. K. (2014). EMCCD based luminescence imaging system for spatially resolved geo-chronometric and radiation dosimetric applications. *Journal of Instrumentation* **9,** P11016.

Chen, Y., Li, Y., Wang, Y., Zhang, M., Cui, Z., Yi, C., and Liu, G. (2015). Late Quaternary glacial history of the Karlik Range, easternmost Tian Shan, derived from 10Be surface exposure and optically stimulated luminescence datings. *Quaternary Science Reviews* **115,** 17-27.

Colonge, D., Claud, E., Deschamps, M., Fourloubey, C., Hernandez, M., Sellami, F., Anderson, L., Busseuil, N., Debenham, N., Garon, H., and O'Farrell, M. (2015). Preliminary results from new Palaeolithic open-air sites near Bayonne (south-western France). *Quaternary International* **364,** 109-125.

Constantin, D., Cameniţă, A., Panaiotu, C., Necula, C., Codrea, V., and Timar-Gabor, A. (2015). Fine and coarse-quartz SAR-OSL dating of Last Glacial loess in Southern Romania. *Quaternary International* **357,** 33-43.

Counts, R. C., Murari, M. K., Owen, L. A., Mahan, S. A., and Greenan, M. (2015). Late Quaternary chronostratigraphic framework of terraces and alluvium along the lower Ohio River, southwestern Indiana and western Kentucky, USA. *Quaternary Science Reviews* **110,** 72-91.

Cunningham, A. C., Wallinga, J., Hobo, N., Versendaal, A. J., Makaske, B., and Middelkoop, H. (2015). Re-evaluating luminescence burial doses and bleaching of fluvial deposits using Bayesian computational statistics. *Earth Surf. Dynam.* **3,** 55-65.

Daura, J., Sanz, M., Julià, R., García-Fernández, D., Fornós, J. J., Vaquero, M., Allué, E., López-García, J. M., Blain, H. A., Ortiz, J. E., Torres, T., Albert, R. M., Rodríguez-Cintas, À., Sánchez-Marco, A., Cerdeño, E., Skinner, A. R., Asmeron, Y., Polyak, V. J., Garcés, M., Arnold, L. J., Demuro, M., Pike, A. W. G., Euba, I., Rodríguez, R. F., Yagüe, A. S., Villaescusa, L., Gómez, S., Rubio, A., Pedro, M., Fullola, J. M., and Zilhão, J. (2015). Cova del Rinoceront (Castelldefels, Barcelona): a terrestrial record for the Last Interglacial period (MIS 5) in the Mediterranean coast of the Iberian Peninsula. *Quaternary Science Reviews* **114,** 203-227.

do Nascimento, D. R., Sawakuchi, A. O., Guedes, C. C. F., Giannini, P. C. F., Grohmann, C. H., and Ferreira, M. P. (2015). Provenance of sands from the confluence of the Amazon and Madeira rivers based on detrital heavy minerals and luminescence of quartz and feldspar. *Sedimentary Geology* **316,** 1-12.

Döhler, S., Damm, B., Terhorst, B., Thiel, C., and Frechen, M. (2015). Late Pleistocene and Holocene landscape formation in a gully catchment area in Northern Hesse, Germany. *Quaternary International* **365,** 42-59.

Fruergaard, M., Andersen, T. J., Nielsen, L. H., Johannessen, P. N., Aagaard, T., and Pejrup, M. (2015). High-resolution reconstruction of a coastal barrier system: impact of Holocene sea-level change. *Sedimentology* **62,** 928-969.

Fruergaard, M., Pejrup, M., Murray, A. S., and Andersen, T. J. (2015). On luminescence bleaching of tidal channel sediments. *Geografisk Tidsskrift - Danish Journal of Geography* **115,** 57-65.

Frumkin, A., Zaidner, Y., Na'aman, I., Tsatskin, A., Porat, N., and Vulfson, L. (2015). Sagging and collapse sinkholes over hypogenic hydrothermal karst in a carbonate terrain. *Geomorphology* **229,** 45-57.

Fuchs, M., Reverman, R., Owen, L. A., and Frankel, K. L. (2015). Reconstructing the timing of flash floods using 10Be surface exposure dating at Leidy Creek alluvial fan and valley, White Mountains, California–Nevada, USA. *Quaternary Research* **83,** 178-186.

Galbraith, R. F. (2015). On the mis-use of mathematics: A comment on "How confident are we about the chronology of the transition between Howieson's Poort and Still Bay?" by Guérin et al. (2013). *Journal of Human Evolution* **80,** 184-186.

Gong, Z., Li, B., and Li, S.-H. (2015). Further studies on the relationship between IRSL and BLSL at relatively high temperatures for potassium-feldspar from sediments. *Journal of Luminescence* **159,** 238-245.

Guérin, G., Frouin, M., Talamo, S., Aldeias, V., Bruxelles, L., Chiotti, L., Dibble, H. L., Goldberg, P., Hublin, J.-J., Jain, M., Lahaye, C., Madelaine, S., Maureille, B., McPherron, S. J. P., Mercier, N., Murray, A. S., Sandgathe, D., Steele, T. E., Thomsen, K. J., and Turq, A. (2015). A multi-method luminescence dating of the Palaeolithic sequence of La Ferrassie based on new excavations adjacent to the La Ferrassie 1 and 2 skeletons. *Journal of Archaeological Science* **58,** 147-166.

Guérin, G., Jain, M., Thomsen, K. J., Murray, A. S., and Mercier, N. (2015). Modelling dose rate to single grains of quartz in well-sorted sand samples: The dispersion arising from the presence of potassium feldspars and implications for single grain OSL dating. *Quaternary Geochronology* **27,** 52-65.

Guo, X., Lai, Z., Lu, Y., Li, X., and Sun, Z. (2015). Optically Stimulated Luminescence (OSL) Chronology of the Dehenglong Landslide from Longyang Gorge to Liujia Gorge along Upper Yellow River, China. *Acta Geologica Sinica-English Edition* **89,** 242-250.

Guo, Y., Huang, C. C., Pang, J., Zha, X., Zhou, Y., Wang, L., Zhang, Y., and Hu, G. (2015). Investigating extreme flood response to Holocene palaeoclimate in the Chinese monsoonal zone: A palaeoflood case study from the Hanjiang River. *Geomorphology* **238,** 187-197.

Guralnik, B., Ankjærgaard, C., Jain, M., Murray, A. S., Müller, A., Wälle, M., Lowick, S. E., Preusser, F., Rhodes, E. J., Wu, T. S., Mathew, G., and Herman, F. (2015). OSL-thermochronometry using bedrock quartz: A note of caution. *Quaternary Geochronology* **25,** 37-48.

Gutiérrez, F., Morgan, M. L., Matthews, V., Gutiérrez, M., and Jiménez-Moreno, G. (2015). Relict slope rings and talus flatirons in the Colorado Piedmont: Origin, chronology and paleoenvironmental implications. *Geomorphology* **231,** 146-161.

Hickin, A. S., Lian, O. B., Levson, V. M., and Cui, Y. (2015). Pattern and chronology of glacial Lake Peace shorelines and implications for isostacy and ice-sheet configuration in northeastern British Columbia, Canada. *Boreas* **44,** 288-304.

Hoffmann, G., Grützner, C., Reicherter, K., and Preusser, F. (2015). Geo-archaeological evidence for a Holocene extreme flooding event within the Arabian Sea (Ras al Hadd, Oman). *Quaternary Science Reviews* **113,** 123-133.

Hornblow, S., Quigley, M., Nicol, A., Van Dissen, R., and Wang, N. (2014). Paleoseismology of the 2010 Mw 7.1 Darfield (Canterbury) earthquake source, Greendale Fault, New Zealand. *Tectonophysics* **637,** 178-190.

Horne, D., Lees, B., Cupper, M., and Fitzsimmons, K. (2015). The development of the Princess Charlotte Bay chenier plain: New results and insights. *Marine Geology* **364,** 12-20.

Hoyos, N., Monsalve, O., Berger, G. W., Antinao, J. L., Giraldo, H., Silva, C., Ojeda, G., Bayona, G., Escobar, J., and Montes, C. (2015). A climatic trigger for catastrophic Pleistocene–Holocene debris flows in the Eastern Andean Cordillera of Colombia. *Journal of Quaternary Science* **30,** 258-270.

Hu, X.-F., Du, Y., Liu, X.-J., Zhang, G.-L., Jiang, Y., and Xue, Y. (2015). Polypedogenic case of loess overlying red clay as a response to the Last Glacial–Interglacial cycle in mid-subtropical Southeast China. *Aeolian Research* **16,** 125-142.

Huang, X., Du, Y., He, Z., Ma, B., and Xie, F. (2015). Late Pleistocene–Holocene paleoseismology of the Batang fault (central Tibet plateau, China). *Geomorphology* **239,** 127-141.

Huang, X., Du, Y., He, Z., Ma, B., and Xie, F. (2015). Late Quaternary slip rate of the Batang Fault and its strain partitioning role in Yushu area, central Tibet. *Tectonophysics* **653,** 52-67.

Ibarra, Y., Corsetti, F. A., Feakins, S. J., Rhodes, E. J., and Kirby, M. E. (2015). Fluvial tufa evidence of Late Pleistocene wet intervals from Santa Barbara, California, U.S.A. *Palaeogeography, Palaeoclimatology, Palaeoecology* **422,** 36-45.

Iovita, R., Doboş, A., Fitzsimmons, K. E., Probst, M., Hambach, U., Robu, M., Vlaicu, M., and Petculescu, A. (2014). Geoarchaeological prospection in the loess steppe: Preliminary results from the Lower Danube Survey for Paleolithic Sites (LoDanS). *Quaternary International* **351,** 98-114.

Jacobs, Z., Li, B., Jankowski, N., and Soressi, M. (2015). Testing of a single grain OSL chronology across the Middle to Upper Palaeolithic transition at Les Cottés (France). *Journal of Archaeological Science* **54,** 110-122.

Jankowski, N. R., Jacobs, Z., and Goldberg, P. (2015). Optical dating and soil micromorphology at MacCauley's Beach, New South Wales, Australia. *Earth Surface Processes and Landforms* **40,** 229-242.

Janz, L., Feathers, J. K., and Burr, G. S. (2015). Dating surface assemblages using pottery and eggshell: assessing radiocarbon and luminescence techniques in Northeast Asia. *Journal of Archaeological Science* **57,** 119-129.

Jara-Muñoz, J., Melnick, D., Brill, D., and Strecker, M. R. (2015). Segmentation of the 2010 Maule Chile earthquake rupture from a joint analysis of uplifted marine terraces and seismic-cycle deformation patterns. *Quaternary Science Reviews* **113,** 171-192.

Jia, L., Zhang, X., He, Z., He, X., Wu, F., Zhou, Y., Fu, L., and Zhao, J. (2015). Late Quaternary climatic and tectonic mechanisms driving river terrace development in an area of mountain uplift: A case study in the Langshan area, Inner Mongolia, northern China. *Geomorphology* **234,** 109-121.

Joordens, J. C. A., d/'Errico, F., Wesselingh, F. P., Munro, S., de Vos, J., Wallinga, J., Ankjaergaard, C., Reimann, T., Wijbrans, J. R., Kuiper, K. F., Mucher, H. J., Coqueugniot, H., Prie, V., Joosten, I., van Os, B., Schulp, A. S., Panuel, M., van der Haas, V., Lustenhouwer, W., Reijmer, J. J. G., and Roebroeks, W. (2014). Homo erectus at Trinil on Java used shells for tool production and engraving. *Nature* **518,** 228–231.

Kadlec, J., Kocurek, G., Mohrig, D., Shinde, D. P., Murari, M. K., Varma, V., Stehlík, F., Beneš, V., and Singhvi, A. K. (2015). Response of fluvial, aeolian, and lacustrine systems to late Pleistocene to Holocene climate change, Lower Moravian Basin, Czech Republic. *Geomorphology* **232,** 193-208.

Kalińska-Nartiša, E., Nartišs, M., Thiel, C., Buylaert, J. P., and Murray, A. S. (2015). Late-glacial to Holocene aeolian deposition in northeastern Europe – The timing of sedimentation at the Iisaku site (NE Estonia). *Quaternary International* **357,** 70-81.

Kazakis, N. A., Kitis, G., and Tsirliganis, N. C. (2015). A cleaning method to minimize contaminant luminescence signal of empty sample carriers using off-the-shelf chemical agents. *Applied Radiation and Isotopes* **95,** 226-232.

Kels, H., Protze, J., Sitlivy, V., Hilgers, A., Zander, A., Anghelinu, M., Bertrams, M., and Lehmkuhl, F. (2014). Genesis of loess-like sediments and soils at the foothills of the Banat Mountains, Romania – Examples from the Paleolithic sites Românești and Coşava. *Quaternary International* **351,** 213-230.

Kijek, N., Chruścińska, A., and Przegiętka, K. R. (2014). The dependence of quartz OSL on stimulation energy. *Radiation Measurements* **71,** 108-112.

Kinoshita, A., Skinner, A. R., Guidon, N., Ignacio, E., Felice, G. D., Buco, C. d. A., Tatumi, S., Yee, M., Figueiredo, A. M. G., and Baffa, O. (2014). Dating human occupation at Toca do Serrote das Moendas, São Raimundo Nonato, Piauí-Brasil by electron spin resonance and optically stimulated luminescence. *Journal of Human Evolution* **77,** 187-195.

Klasen, N., Fischer, P., Lehmkuhl, F., and Hilgers, A. (2015). Luminescence dating of loess deposits from the Remagen-Schwalbenberg site, Western Germany. *Geochronometria* **42,** 67-77.

Komatsu, T., and Tsukamoto, S. (2015). Late Glacial lake-level changes in the Lake Karakul basin (a closed glacierized-basin), eastern Pamirs, Tajikistan. *Quaternary Research* **83,** 137-149.

Koul, D. K., and Patil, P. G. (2015). Influence of in Situ Temperature on the Sensitization of Quartz: A Simulation Study. *Geochronometria* **42,** 28-40.

Leighton, C. L., and Bailey, R. M. (2015). Investigating the potential of HCl-only treated samples using range-finder OSL dating. *Quaternary Geochronology* **25,** 1-9.

Li, B., Roberts, R. G., Jacobs, Z., and Li, S.-H. (2015). Potential of establishing a 'global standardised growth curve' (gSGC) for optical dating of quartz from sediments. *Quaternary Geochronology* **27,** 94-104.

Li, B., Roberts, R. G., Jacobs, Z., Li, S.-H., and Guo, Y.-J. (2015). Construction of a 'global standardised growth curve' (gSGC) for infrared stimulated luminescence dating of K-feldspar. *Quaternary Geochronology* **27,** 119-130.

Li, X., Huang, C. C., Pang, J., Zha, X., and Ma, Y. (2015). Sedimentary and hydrological studies of the Holocene palaeofloods in the Shanxi-Shaanxi Gorge of the middle Yellow River, China. *International Journal of Earth Sciences* **104,** 277-288.

Li, Y., Wang, N. a., and Zhang, C. (2014). An Abrupt Centennial-Scale Drought Event and Mid-Holocene Climate Change Patterns in Monsoon Marginal Zones of East Asia. *Plos One* **9**.

Lima, C. C. U., Bezerra, F. H. R., Nogueira, F. C. C., Maia, R. P., and Sousa, M. O. L. (2014). Quaternary fault control on the coastal sedimentation and morphology of the São Francisco coastal plain, Brazil. *Tectonophysics* **633,** 98-114.

Liritzis, I., and Vafiadou, A. (2015). Surface luminescence dating of some Egyptian monuments. *Journal of Cultural Heritage* **16,** 134-150.

Lisá, L., Hošek, J., Bajer, A., Matys Grygar, T., and Vandenberghe, D. (2014). Geoarchaeology of Upper Palaeolithic loess sites located within a transect through Moravian valleys, Czech Republic. *Quaternary International* **351,** 25-37.

Lister, A. M., and Grün, R. (2015). Mammoth and musk ox ESR-dated to the Early Midlandian at Aghnadarragh, County Antrim, Northern Ireland, and the age of the Fermanagh Stadial. *Geological Journal* **50,** 306-320.

Liu, B., Jin, H., Sun, Z., Miao, Y., Su, Z., and Zhang, C. (2014). Evidence of Holocene millennial-scale climatic change from Gonghe Basin peat deposit, northeastern Qinghai-Tibet Plateau. *Journal of Arid Environments* **106,** 1-10.

Liu, X.-J., Lai, Z., Madsen, D., and Zeng, F. (2015). Last deglacial and Holocene lake level variations of Qinghai Lake, north-eastern Qinghai–Tibetan Plateau. *Journal of Quaternary Science* **30,** 245-257.

Livingstone, S. J., Piotrowski, J. A., Bateman, M. D., Ely, J. C., and Clark, C. D. (2015). Discriminating between subglacial and proglacial lake sediments: an example from the Dänischer Wohld Peninsula, northern Germany. *Quaternary Science Reviews* **112,** 86-108.

Loibl, D., Hochreuther, P., Schulte, P., Hülle, D., Zhu, H., Bräuning, A., and Lehmkuhl, F. (2015). Toward a late Holocene glacial chronology for the eastern Nyainqêntanglha Range, southeastern Tibet. *Quaternary Science Reviews* **107,** 243-259.

Lomax, J., Fuchs, M., Preusser, F., and Fiebig, M. (2014). Luminescence based loess chronostratigraphy of the Upper Palaeolithic site Krems-Wachtberg, Austria. *Quaternary International* **351,** 88-97.

Long, H., Haberzettl, T., Tsukamoto, S., Shen, J., Kasper, T., Daut, G., Zhu, L., Mäusbacher, R., and Frechen, M. (2015). Luminescence dating of lacustrine sediments from Tangra Yumco (southern Tibetan Plateau) using post-IR IRSL signals from polymineral grains. *Boreas* **44,** 139-152.

Long, H., and Shen, J. (2015). Underestimated 14C-based chronology of late Pleistocene high lake-level events over the Tibetan Plateau and adjacent areas: Evidence from the Qaidam Basin and Tengger Desert. *Science China Earth Sciences* **58,** 183-194.

Lopes, R. P., Dillenburg, S. R., Schultz, C. L., Ferigolo, J., Ribeiro, A. M., Pereira, J. C., Holanda, E. C., Pitana, V. G., and Kerber, L. (2014). The sea-level highstand correlated to marine isotope stage (mis) 7 in the coastal plain of the state of Rio Grande do Sul, Brazil. *Anais da Academia Brasileira de Ciencias* **86,** 1573-1595.

Lopes, R. P., Kinoshita, A., Baffa, O., Figueiredo, A. M. G., Dillenburg, S. R., Schultz, C. L., and Pereira, J. C. (2014). ESR dating of Pleistocene mammals and marine shells from the coastal plain of Rio Grande do Sul state, southern Brazil. *Quaternary International* **352,** 124-134.

Luirei, K., Bhakuni, S. S., Suresh, N., Kothyari, G. C., and Pant, P. D. (2014). Tectonic geomorphology and morphometry of the frontal part of Kumaun Sub-Himalaya: Appraisal of tectonic activity. *Zeitschrift für Geomorphologie* **58,** 435-458.

Lunkka, J. P., Sarala, P., and Gibbard, P. L. (2015). The Rautuvaara section, western Finnish Lapland, revisited – new age constraints indicate a complex Scandinavian Ice Sheet history in northern Fennoscandia during the Weichselian Stage. *Boreas* **44,** 68-80.

Mahan, S. A., Gray, H. J., Pigati, J. S., Wilson, J., Lifton, N. A., Paces, J. B., and Blaauw, M. (2014). A geochronologic framework for the Ziegler Reservoir fossil site, Snowmass Village, Colorado. *Quaternary Research* **82,** 490-503.

May, S. M., Zander, A., Francois, J. P., Kelletat, D., Pötsch, S., Rixhon, G., and Brückner, H. (2015). Chronological and geoarchaeological investigations on an anthropogenic shell accumulation layer in the Longotoma dune field (Central Chile). *Quaternary International* **367,** 32-41.

Minckley, T. A., Haws, J. A., Benedetti, M. M., Brewer, S. C., and Forman, S. L. (2015). Last interglacial vegetation and climate history from the Portuguese coast. *Journal of Quaternary Science* **30,** 59-69.

Mischke, S., Madsen, D., Zhang, C., and Lai, Z. (2015). Reply to comment by Zhang (2014): The Shell Bar in the Qaidam Basin: fluvial or lake deposit, and OSL versus C-14 age data. *Journal of Paleolimnology* **53,** 335-344.

Moreiras, S. M., Hermanns, R. L., and Fauqué, L. (2015). Cosmogenic dating of rock avalanches constraining Quaternary stratigraphy and regional neotectonics in the Argentine Central Andes (32° S). *Quaternary Science Reviews* **112,** 45-58.

Munyikwa, K., Gilliland, K., Gibson, T., Mann, E., Rittenour, T. M., Grekul, C., and Blaikie-Birkigt, K. (2014). Late holocene temporal constraints for human occupation levels at the Bodo archaeological locality, East-central Alberta, Canada using radiocarbon and luminescence chronologies. *Plains Anthropologist* **59,** 109-143.

Murton, J. B., Bowen, D. Q., Candy, I., Catt, J. A., Currant, A., Evans, J. G., Frogley, M. R., Green, C. P., Keen, D. H., Kerney, M. P., Parish, D., Penkman, K., Schreve, D. C., Taylor, S., Toms, P. S., Worsley, P., and York, L. L. (2015). Middle and Late Pleistocene environmental history of the Marsworth area, south-central England. *Proceedings of the Geologists' Association* **126,** 18-49.

Nazari, H., Ritz, J. F., Walker, R. T., Salamati, R., Rizza, M., Patnaik, R., Hollingsworth, J., Alimohammadian, H., Jalali, A., Kaveh Firouz, A., and Shahidi, A. (2014). Palaeoseismic evidence for a medieval earthquake, and preliminary estimate of late Pleistocene slip-rate, on the Firouzkuh strike-slip fault in the Central Alborz region of Iran. *Journal of Asian Earth Sciences* **82,** 124-135.

Nelson, M. S., Gray, H. J., Johnson, J. A., Rittenour, T. M., Feathers, J. K., and Mahan, S. A. (2015). User Guide for Luminescence Sampling in Archaeological and Geological Contexts. *Advances in Archaeological Practice* **3,** 166-177.

Nimnate, P., Chutakositkanon, V., Choowong, M., Pailoplee, S., and Phantuwongraj, S. (2015). Evidence of Holocene sea level regression from Chumphon coast of the Gulf of Thailand. *ScienceAsia* **41,** 55-63.

Odriozola, C. P., Burbidge, C. I., Isabel Dias, M., and Hurtado, V. (2014). Dating of Las Mesas Copper Age walled enclosure (La Fuente, Spain). *Trabajos De Prehistoria* **71,** 343-352.

Oliver, T. S., Dougherty, A. J., Gliganic, L. A., and Woodroffe, C. D. (2015). Towards more robust chronologies of coastal progradation: Optically stimulated luminescence ages for the coastal plain at Moruya, south-eastern Australia. *The Holocene* **25,** 536-546.

Oniya, E. O., Polymeris, G. S., Jibiri, N. N., Tsirliganis, N. C., Babalola, I. A., and Kitis, G. (2015). Contributions of pre-exposure dose and thermal activation in pre-dose sensitizations of unfired and annealed quartz. *Radiation Physics and Chemistry* **110,** 105-113.

Ou, X., Lai, Z., Zhou, S., Chen, R., and Zeng, L. (2015). Optical dating of young glacial sediments from the source area of the Urumqi River in Tianshan Mountians, northwestern China. *Quaternary International* **358,** 12-20.

Pederson, J. L., Chapot, M. S., Simms, S. R., Sohbati, R., Rittenour, T. M., Murray, A. S., and Cox, G. (2014). Reply to Simon and Reed: Independent and converging results rule out historic disturbance and

confirm age constraints for Barrier Canyon rock art. *Proceedings of the National Academy of Sciences of the United States of America* **111,** E5604-E5604.

Pei, S., Niu, D., Guan, Y., Nian, X., Yi, M., Ma, N., Li, X., and Sahnouni, M. (2015). Middle Pleistocene hominin occupation in the Danjiangkou Reservoir Region, Central China: studies of formation processes and stone technology of Maling 2A site. *Journal of Archaeological Science* **53,** 391-407.

Phartiyal, B., Singh, R., and Kothyari, G. C. (2015). Late-Quaternary geomorphic scenario due to changing depositional regimes in the Tangtse Valley, Trans-Himalaya, NW India. *Palaeogeography, Palaeoclimatology, Palaeoecology* **422,** 11-24.

Pietsch, T. J., Brooks, A. P., Spencer, J., Olley, J. M., and Borombovits, D. (2015). Age, distribution, and significance within a sediment budget, of in-channel depositional surfaces in the Normanby River, Queensland, Australia. *Geomorphology* **239,** 17-40.

Plotzki, A., May, J. H., Preusser, F., Roesti, B., Denier, S., Lombardo, U., and Veit, H. (2015). Geomorphology and evolution of the late Pleistocene to Holocene fluvial system in the south-eastern Llanos de Moxos, Bolivian Amazon. *CATENA* **127,** 102-115.

Pluckhahn, T. J., Hodson, A. D., Rink, W. J., Thompson, V. D., Hendricks, R. R., Doran, G., Farr, G., Cherkinsky, A., and Norman, S. P. (2015). Radiocarbon and Luminescence Age Determinations on Mounds at Crystal River and Roberts Island, Florida, USA. *Geoarchaeology* **30,** 238-260.

Polymeris, G. S., Şahiner, E., Meriç, N., and Kitis, G. (2015). Experimental features of natural thermally assisted OSL (NTA-OSL) signal in various quartz samples; preliminary results. *Nuclear Instruments and Methods in Physics Research Section B: Beam Interactions with Materials and Atoms* **349,** 24-30.

Reimann, T., Notenboom, P. D., De Schipper, M. A., and Wallinga, J. (2015). Testing for sufficient signal resetting during sediment transport using a polymineral multiple-signal luminescence approach. *Quaternary Geochronology* **25,** 26-36.

Ribolini, A., Bini, M., Consoloni, I., Isola, I., Pappalardo, M., Zanchetta, G., Fucks, E., Panzeri, L., Martini, M., and Terrasi, F. (2014). Late-Pleistocene Wedge Structures Along the Patagonian Coast (Argentina): Chronological Constraints and Palaeo-Environmental Implications. *Geografiska Annaler Series a-Physical Geography* **96,** 161-176.

Rodrigues, L., Lombardo, U., Fehr, S., Preusser, F., and Veit, H. (2015). Pre-Columbian agriculture in the Bolivian Lowlands: Construction history and management of raised fields in Bermeo. *Catena* **132,** 126-138.

Roskosch, J., Winsemann, J., Polom, U., Brandes, C., Tsukamoto, S., Weitkamp, A., Bartholomäus, W. A., Henningsen, D., and Frechen, M. (2015). Luminescence dating of ice-marginal deposits in northern Germany: evidence for repeated glaciations during the Middle Pleistocene (MIS 12 to MIS 6). *Boreas* **44,** 103-126.

Sadek, A. M., Eissa, H. M., Basha, A. M., Carinou, E., Askounis, P., and Kitis, G. (2015). The deconvolution of thermoluminescence glow-curves using general expressions derived from the one trap-one recombination (OTOR) level model. *Applied Radiation and Isotopes* **95,** 214-221.

Santos, A. M. C., Mohammadi, M., and Afshar V, S. (2015). Energy dependency of a water-equivalent fibre-coupled beryllium oxide (BeO) dosimetry system. *Radiation Measurements* **73,** 1-6.

Scheffers, A. M., Engel, M., May, S. M., Scheffers, S. R., Joannes-Boyau, R., Haenssler, E., Kennedy, K., Kelletat, D., Brueckner, H., Voett, A., Schellmann, G., Schaebitz, F., Radtke, U., Sommer, B., Willershaeuser, T., and Felis, T. (2014). Potential and limits of combining studies of coarse- and fine-

grained sediments for the coastal event history of a Caribbean carbonate environment. *Sedimentary Coastal Zones from High to Low Latitudes: Similarities and Differences* **388,** 503-531.

Schmeisser McKean, R. L., Goble, R. J., Mason, J. B., Swinehart, J. B., and Loope, D. B. (2015). Temporal and spatial variability in dune reactivation across the Nebraska Sand Hills, USA. *The Holocene* **25,** 523-535.

Schmidt, C., Kreutzer, S., DeWitt, R., and Fuchs, M. (2015). Radiofluorescence of quartz: A review. *Quaternary Geochronology* **27,** 66-77.

Sighinolfi, G. P., Sibilia, E., Contini, G., and Martini, M. (2015). Thermoluminescence dating of the Kamil impact crater (Egypt). *Meteoritics & Planetary Science* **50,** 204-213.

Simon, N., and Reed, R. (2014). Incorrect representation of Barrier Canyon rock art site's history and other factors invalidate reported dates. *Proceedings of the National Academy of Sciences of the United States of America* **111,** E5602-E5603.

Singh, L. L., and Gartia, R. K. (2015). Derivation of a simplified OSL OTOR equation using Wright Omega function and its application. *Nuclear Instruments and Methods in Physics Research Section B: Beam Interactions with Materials and Atoms* **346,** 45-52.

Smith, R. W., Eakins, J. S., Hager, L. G., Rothkamm, K., and Tanner, R. J. (2015). Development of a retrospective/fortuitous accident dosimetry service based on OSL of mobile phones. *Radiation Protection Dosimetry* **164,** 89-92.

Sunta, C. (2015). "Unravelling thermoluminescence." Springer, New Delhi.

Tourloukis, V., Karkanas, P., and Wallinga, J. (2015). Revisiting Kokkinopilos: Middle Pleistocene radiometric dates for stratified archaeological remains in Greece. *Journal of Archaeological Science* **57,** 355-369.

Újvári, G., Molnár, M., Novothny, Á., Páll-Gergely, B., Kovács, J., and Várhegyi, A. (2014). AMS ^{14}C and OSL/IRSL dating of the Dunaszekcső loess sequence (Hungary): chronology for 20 to 150 ka and implications for establishing reliable age–depth models for the last 40 ka. *Quaternary Science Reviews* **106,** 140-154.

Urbanova, P., Hourcade, D., Ney, C., and Guibert, P. (2015). Sources of uncertainties in OSL dating of archaeological mortars: The case study of the Roman amphitheatre “Palais-Gallien” in Bordeaux. *Radiation Measurements* **72,** 100-110.

Vassallo, R., Mugnier, J. L., Vignon, V., Malik, M. A., Jayangondaperumal, R., Srivastava, P., Jouanne, F., and Carcaillet, J. (2015). Distribution of the Late-Quaternary deformation in Northwestern Himalaya. *Earth and Planetary Science Letters* **411,** 241-252.

Vaughn, K. J., Eerkens, J. W., Lipo, C., Sakai, S., and Schreiber, K. (2014). It's About Time? Testing the Dawson Ceramic Seriation Using Luminescence Dating, Southern Nasca Region, Peru. *Latin American Antiquity* **25,** 449-461.

Vokhmintsev, A. S., Minin, M. G., Henaish, A. M. A., and Weinstein, I. A. (2015). Spectrally resolved thermoluminescence measurements in fluorescence spectrometer. *Measurement* **66,** 90-94.

Wang, F., Sun, D., Chen, F., Bloemendal, J., Guo, F., Li, Z., Zhang, Y., Li, B., and Wang, X. (2015). Formation and evolution of the Badain Jaran Desert, North China, as revealed by a drill core from the desert centre and by geological survey. *Palaeogeography, Palaeoclimatology, Palaeoecology* **426,** 139-158.

Wang, X. L., Du, J. H., Adamiec, G., and Wintle, A. G. (2015). The origin of the medium OSL component in West Australian quartz. *Journal of Luminescence* **159,** 147-157.

Wang, Z., Zhao, H., Dong, G., Zhou, A., Liu, J., and Zhang, D. (2014). Reliability of radiocarbon dating on various fractions of loess-soil sequence for Dadiwan section in the western Chinese Loess Plateau. *Frontiers of Earth Science* **8,** 540-546.

Wilczyński, J., Wojtal, P., Łanczont, M., Mroczek, P., Sobieraj, D., and Fedorowicz, S. (2015). Loess, flints and bones: Multidisciplinary research at Jaksice II Gravettian site (southern Poland). *Quaternary International* **359–360,** 114-130.

Wróbel, D., Bilski, P., Marczewska, B., Mrozik, A., and Kłosowski, M. (2015). Characterization of the Risø TL/OSL DA-20 reader for application in TL dosimetry. *Radiation Measurements* **74,** 1-5.

Yang, X., Scuderi, L. A., Wang, X., Scuderi, L. J., Zhang, D., Li, H., Forman, S., Xu, Q., Wang, R., Huang, W., and Yang, S. (2015). Groundwater sapping as the cause of irreversible desertification of Hunshandake Sandy Lands, Inner Mongolia, northern China. *Proceedings of the National Academy of Sciences* **112,** 702-706.

Yu, L., Dong, Z., Lai, Z., Qian, G., and Pan, T. (2015). Origin and lateral migration of linear dunes in the Qaidam Basin of NW China revealed by dune sediments, internal structures, and optically stimulated luminescence ages, with implications for linear dunes on Titan: Comment and Discussion. *Geological Society of America Bulletin* **127,** 316-320.

Zhang, H. (2015). A comment on Lai et al. (2014) concerning the origin of the Shell Bar section from the Qaidam Basin, NE Tibetan Plateau: lake formation versus river channel deposit, and C-14 versus OSL dates. *Journal of Paleolimnology* **53,** 321-334.

Zhang, Y., Huang, C. C., Pang, J., Zha, X., Zhou, Y., and Wang, X. (2015). Holocene palaeoflood events recorded by slackwater deposits along the middle Beiluohe River valley, middle Yellow River basin, China. *Boreas* **44,** 127-138.

Zhang, Y., Huang, C. C., Pang, J., Zhou, Y., Shang, R., Zhou, Q., Guo, Y., Liu, T., and Hu, G. (2015). OSL dating of the massive landslide-damming event in the Jishixia Gorge, on the upper Yellow River, NE Tibetan Plateau. *The Holocene* **25,** 745-757.

Zhao, H., Sheng, Y., Zhang, J., Zhao, Y., and Li, G. (2015). Oasis evolution processes and mechanisms in the lower reaches of Heihe River, Inner Mongolia, China since 1 ka ago. *The Holocene* **25,** 445-453.

Zhao, J., Wang, J., Harbor, J. M., Liu, S., Yin, X., and Wu, Y. (2015). Quaternary glaciations and glacial landform evolution in the Tailan River valley, Tianshan Range, China. *Quaternary International* **358,** 2-11.

Zöller, L., Richter, D., Blanchard, H., Einwögerer, T., Händel, M., and Neugebauer-Maresch, C. (2014). Our oldest children: Age constraints for the Krems-Wachtberg site obtained from various thermoluminescence dating approaches. *Quaternary International* **351,** 83-87.

Papers from the 9th New World Luminescence Dating Workshop, published in Quaternary International 362

Brown, N. D., Rhodes, E. J., Antinao, J. L., and McDonald, E. V. (2015). Single-grain post-IR IRSL signals of K-feldspars from alluvial fan deposits in Baja California Sur, Mexico. *Quaternary International* **362,** 132-138.

Ellwein, A. L., Mahan, S. A., and McFadden, L. D. (2015). Impacts of climate change on the formation and stability of late Quaternary sand sheets and falling dunes, Black Mesa region, southern Colorado Plateau, USA. *Quaternary International* **362,** 87-107.

Fuchs, M. C., Kreutzer, S., Burow, C., Dietze, M., Fischer, M., Schmidt, C., and Fuchs, M. (2015). Data processing in luminescence dating analysis: An exemplary workflow using the R package 'Luminescence'. *Quaternary International* **362,** 8-13.

Gliganic, L. A., May, J. H., and Cohen, T. J. (2015). All mixed up: Using single-grain equivalent dose distributions to identify phases of pedogenic mixing on a dryland alluvial fan. *Quaternary International* **362,** 23-33.

Gray, H. J., and Mahan, S. A. (2015). Variables and potential models for the bleaching of luminescence signals in fluvial environments. *Quaternary International* **362,** 42-49.

Hanson, P. R., Mason, J. A., Jacobs, P. M., and Young, A. R. (2015). Evidence for bioturbation of luminescence signals in eolian sand on upland ridgetops, southeastern Minnesota, USA. *Quaternary International* **362,** 108-115.

Jain, M., Buylaert, J. P., Thomsen, K. J., and Murray, A. S. (2015). Further investigations on 'non-fading' in K-Feldspar. *Quaternary International* **362,** 3-7.

Lawson, M. J., Daniels, J. T. M., and Rhodes, E. J. (2015). Assessing Optically Stimulated Luminescence (OSL) signal contamination within small aliquots and single grain measurements utilizing the composition test. *Quaternary International* **362,** 34-41.

Mahan, S. A., Donlan, R. A., and Kardos, B. (2015). Luminescence dating of anthropogenic features of the San Luis Valley, Colorado: From stone huts to stone walls. *Quaternary International* **362,** 50-62.

Mahan, S. A., Nelson, M. S., Rittenour, T. M., Hanson, P., and Rhodes, E. (2015). The 9th New World Luminescence Dating Workshop: Aim of the community and scope of the conference proceedings. *Quaternary International* **362,** 1-2.

McGuire, C., and Rhodes, E. J. (2015). Determining fluvial sediment virtual velocity on the Mojave River using K-feldspar IRSL: Initial assessment. *Quaternary International* **362,** 124-131.

Rhodes, E. J. (2015). Dating sediments using potassium feldspar single-grain IRSL: Initial methodological considerations. *Quaternary International* **362,** 14-22.

Ribeiro, L. M. A. L., Sawakuchi, A. O., Wang, H., Sallun Filho, W., and Nogueira, L. (2015). OSL dating of Brazilian fluvial carbonates (tufas) using detrital quartz grains. *Quaternary International* **362,** 146-156.

Rich, J., Rittenour, T. M., Nelson, M. S., and Owen, J. (2015). OSL chronology of middle to late Holocene aeolian activity in the St. Anthony dune field, southeastern Idaho, USA. *Quaternary International* **362,** 77-86.

Rittenour, T. M., Coats, L. L., and Metcalfe, D. (2015). Investigation of late and post-Fremont alluvial stratigraphy of Range Creek, east-central Utah: Use of OSL when radiocarbon fails. *Quaternary International* **362,** 63-76.

Spencer, J. Q. G., Oviatt, C. G., Pathak, M., and Fan, Y. (2015). Testing and refining the timing of hydrologic evolution during the latest Pleistocene regressive phase of Lake Bonneville. *Quaternary International* **362,** 139-145.

Wyshnytzky, C. E., Rittenour, T. M., Nelson, M. S., and Thackray, G. (2015). Luminescence dating of late Pleistocene proximal glacial sediments in the Olympic Mountains, Washington. *Quaternary International* **362,** 116-123.

Conference Announcements: L.A.I.S.2015

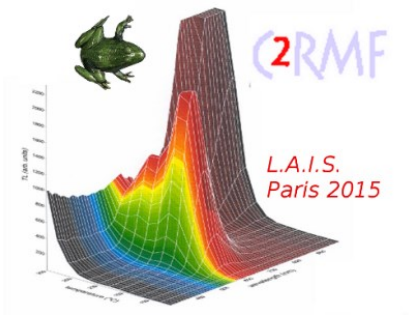

3rd Luminescence in Archaeology International Symposium

Palais du Louvre, Paris
2nd – 4th September, 2015

The 3rd Luminescence in Archaeology International Symposium (**L.A.I.S.2015**) will be held in Paris, France, from the 2nd to the 4th of September, 2015. It will be hosted by the Dating Group, Centre de Recherche et Restauration des Musées de France (C2RMF), Palais du Louvre, Paris (France).
L.A.I.S. 2015 continues the series of symposia initiated in Delphi 2009 and Lisbon 2012. It is an international initiative focusing on the use of luminescence for the dating and analysis of materials and questions of archaeological significance; in addition it supports archaeological and archaeometrical communities of the World to further develop and expose luminescence issues.

Scope
Theme 1 - Museum objects
Theme 2 - Ceramics, stone, glass and metals
Theme 3 - Reconstruction of environments in archaeological sites

Focus 1 - Dosimetry and Dating
Focus 2 - Spectroscopy and analysis of materials

Pre-meeting Workshop
A training course on the new **DosiVox** software, developed at the IRAMAT-CRP2A laboratory (Bordeaux, France), will be held on Tuesday, 1st September. It is open to a limited number of participants.
Please send expression of interest to: lais15@sciencesconf.org

Further information
Further information about the conference can be found trough the web site:

http://lais15.sciencesconf.org/

You can reach us by email at:

lais15@sciencesconf.org

The L.A.I.S.2015 organizers would be grateful if you would communicate this announcement to your colleagues and students studying luminescence phenomena in archaeological and cultural heritage materials, or applying luminescence data to archaeological and cultural heritage problems.

Antoine ZINK, Elisa PORTO
Centre de Recherche et de Restauration des musées de France

Conference Announcements: LumiDoz 9

9th International Conference on Luminescence and ESR Dosimetry (LumiDoz 9)

This year, Akdeniz University Nuclear Research and Application Center, will host the 9th International Conference on Luminescence and ESR Dosimetry (LumiDoz 9) on September 2 – 4, 2015.

INVITED SPEAKERS

Dr. Shin Toyoda
Dr. Virgilio Correcher
Dr. Peter Townsend

TOPICS

Luminescence Mechanisms:
-Thermoluminescence (TL)
-Optically Stimulated Luminescence (OSL)
-Radioluminescence (RL)
-Photoluminescence (PL)
-Other Luminescence Mechanisms

Luminescent Materials:
-Natural Materials
-Synthetic Materials
-Luminescence Properties
-Crystal Defects (Luminescence and ESR studies)
-Material Production and Applications

Applied Radiation Physics:
-Interaction of Radiation with Matter
-Radiation Safety and Protection
-Radiation Protection of Foods
-Radiation Sterilization
-Environmental Radioactivity

Dosimetry Methods:
-Luminescence dosimetry
-Personal dosimetry
-Medical dosimetry
-Retrospective dosimetry
-ESR dosimetry

Detection of Irradiated Foods:
-Thermoluminescence (TL)
-Electron Spin Resonance (ESR)
-Optically Stimulated Luminescence (OSL)

Archaeological and Geological Dating:
-Thermoluminescence Method (TL)
-Optically Stimulated Luminescence Method (OSL)
-Electron Spin Resonance Method (ESR)

Other related issues and technological applications can also be presented. Proceedings of both oral and poster presentations –those eligible for peer-reviewed publication- will be published in Journal of Nuclear Science (limited to one first-author paper per active participant).

More information can be found on the conference web page:
http://nukleer.akdeniz.edu.tr/lumidoz9

We look forward to welcoming you to Antalya,
Dr. İbrahim H. ALBAYRAK (on behalf of the local organising committee)

Conference Announcements: APLED 2015

The 4th Asia Pacific Conference on Luminescence and ESR dating including non-dating applications (APLED 2015) will be held in
Adelaide, Australia, from the **22nd - 26th November, 2015**.

APLED 2015 will be hosted by the Environmental Luminescence Group of the School of Physical Sciences, the Institute for Photonics and Advanced Sensing, and the Environment Institute, University of Adelaide, South Australia.

The conference seeks to bring together researchers to present new developments in Luminescence and ESR, with particular focus on techniques, applications and issues relevant to the Asia-Pacific region.

Conference scope: Luminescence dating has its roots in the middle of the 20th century, with the landmark paper by Farrington Daniels and colleagues (Science, 1953) being the first to expound the application of thermoluminescence as a dating technique for the geosciences and archaeology. The intervening years have seen the introduction of ESR and optical dating, and their rapid evolution and application to diverse fields in which ionising radiation effects provide either a "clock" or a characterisation tool. The conference invites contributions from this broad range of applications, including Quaternary geology, geomorphology and landscape evolution, palaeontology, palaeobotany, archaeology, soil science, palaeoclimatology, provenancing, mineral prospecting, tectonics, space science, dose-rate assessment, retrospective population dosimetry and radiological event studies, including relating to the aftermath of the 2011 Tohoku earthquake. Contributions are also invited on applications to new materials, current developments and methodological aspects of ESR, thermoluminescence and radioluminescence, and novel optical dating techniques such as TT-OSL and PIR-IRSL.

Further information on the conference, including details about abstract submission and registration, can be found on our web site at

http://www.adelaide.edu.au/apled2015/

We look forward to welcoming you to Adelaide,

Nigel Spooner and Lee Arnold (on behalf of the local organising committee)

Conference Announcements: SSD 18

We are pleased to announce the 18th International Conference on Solid State Dosimetry, SSD18, which will be held in Munich, Germany, 3 July - 8 July, 2016.

This series of conferences began in 1965 at Stanford, USA, and since then has expanded its initial scope from luminescence dosimetry to the current variety of solid state processes and methods available for radiation dosimetry.

In 2016, the main topics of the conference will be:

- Basic physical processes
- Material characteristics
- Monitoring and detection
- Clinical dosimetry
- Dating and Dose reconstruction
- Instrumentation/detectors

A School on Solid State Dosimetry will be offered 29 June - 2 July, 2016. The School is intended for scientist who are new in the field and for those who like to deepen their knowledge.

For more information on the conference, please visit the conference homepage

www.ssd18.org

We are looking forward to welcoming you to Munich, Germany!

Dr. Clemens Woda

Ancient TL

ISSN 0735-1348

Aims and Scope

Ancient TL is a journal devoted to Luminescence dating, Electron Spin Resonance (ESR) dating, and related techniques. It aims to publish papers dealing with experimental and theoretical results in this field, with a minimum of delay between submission and publication. Ancient TL also publishes a current bibliography, thesis abstracts, letters, and miscellaneous information, e.g., announcements for meetings.

Frequency

Two issues per annum in June and December

Submission of articles to Ancient TL

Ancient TL has a reviewing system in which direct dialogue is encouraged between reviewers and authors. For instructions to authors and information on how to submit to Ancient TL, please visit the website at:
http://www.ecu.edu/cs-cas/physics/ancient-timeline/ancient-tl1.cfm

Journal Enquiries

For enquiries please contact the editor:
Regina DeWitt, Department of Physics, East Carolina University, Howell Science Complex, 1000 E. 5th Street, Greenville, NC 27858, USA; Tel: +252-328-4980; Fax: +252-328-0753 (dewittr@ecu.edu)

Subscriptions to Ancient TL

Ancient TL Vol. 32 No.2 December 2014 was the last issue to be published in print. Past and current issues are available for download free of charge from the Ancient TL website:
http://www.ecu.edu/cs-cas/physics/ancient-timeline/ancient-tl5.cfm